Multiple Scattering Effects in the Lidar Pulse Stretching Problem

By
Steven D. Miller and Graeme L. Stephens

Department of Atmospheric Science
Colorado State University
Fort Collins, Colorado

Research supported by DOD Center for Geosciences-Phase II at CIRA/CSU grant #DAAH04-94-G-0420
and NASA research grant #NAG1-1702

Colorado State University

Department of Atmospheric Science

Paper No. 642

MULTIPLE SCATTERING EFFECTS IN THE LIDAR PULSE STRETCHING PROBLEM

Steven D. Miller and Graeme L. Stephens

Research supported by DOD Center for
Geosciences-Phase II at CIRA/CSU
Grant #DAAH04-94-G-0420 and NASA
Research Grant #NAG1-1702

ABSTRACT OF THESIS

MULTIPLE SCATTERING EFFECTS IN THE LIDAR PULSE STRETCHING PROBLEM

The implementation of operational active sensors on the space platform is no longer a question of "if", but of "when". The recently conducted Lidar in Space Technology Experiment (LITE) has generated a burgeoning interest in learning more about the possible operational role of the active sensor on this platform. This unique and unprecedented experiment represents the first attempt to employ a lidar (Light Detection and Ranging) instrument at orbit altitudes (256km AMSL). The detailed and and diverse data set obtained from the STS-64 mission contains a wealth of atmospheric profile information at a resolution unattainable from passive instruments on this platform. In addition to the expected returns from surface, cloud, atmospheric aerosol and density discontinuities, several occurrences of anomalously extended cloud bases indicated a possible problem in the ranging algorithm, which assumes that the lidar signal backscatters off targets exactly once before returning to the detector (as per the conventional radar ranging algorithm, a single scattering approximation).

This problem was associated with multiple scattering of the lidar beam, resulting in a fraction of the return signal traveling an added distance beyond single scatter path lengths and hence being ranged at distances corresponding to this extended travel distance. This phenomenon is very similar to the radar flare echo, which is often observed in returns behind cores of intense rainfall. It has also been addressed

in studies of ground-based lidar observations of clouds, including fog. If the additional distance surpassed a critical value defined by the satellite+cloud geometry, the mis-ranging effects resulted in signals occurring below the true cloud base (for the nadir-pointing instrument), and even instances of returns on the order of several kilometers below the surface of the Earth! Multiple scattering is a problem at orbit altitudes due to the finite divergence of the receiver telescope's field of view. At these altitudes, a 3.5 mrad detector field of view translates to a cloud-top footprint roughly 1km in diameter. Depending on the optical properties of the cloud, this means that radially-scattered light will have an increased probability of scattering back into the detector as the detector's view area increases. For ranges considered by most terrestrial lidar applications, this divergence is a negligible quantity, but cannot be neglected at orbit altitudes as spot sizes become significant with respect to the mean free photon path-length.

This study focused on examining the lidar pulse stretching problem in terms of the optical properties of idealized cloud structures, with the hope of determining ways of using these observed pulse extensions in the inverse problem–deducing relevant optical properties of the cloud media based on the pulse extension behaviors that they cause. By posing the LITE problem in a stochastic radiative transfer context (via Monte Carlo simulations), the multiple scattering behavior which manifests itself in ranging errors (addressed here largely in the context of below-cloud-base pulse extensions) was examined as a function of the driving optical properties of the medium. The pulse extensions were then modeled as a function of these cloud parameters in the interest of identifying possible utility of the pulse stretching data in backing out these quantities.

The results of this study indicate that certain properties of the cloud (in particular, cloud particle phase, nature of the scattering phase function, and the specular cloud extinction coefficient), are products which to first-order may be inferred from

observations of pulse stretching. Simultaneous solutions abound for a single measurement, the ill-posed problem may be constrained to a tractable one given an independent measurement of cloud optical depth. Furthermore, variable field-of-view instrumentation may aid in identifying orthogonal relationships between the retrieval parameters; enabling the construction of an unambiguous retrieval grid for simultaneous retrieval of both of these quantities.

Steven D. Miller
Atmospheric Science Department
Colorado State University
Fort Collins, Colorado 80523
Fall 1997

ACKNOWLEDGEMENTS

We wish to thank Drs. Tom Vonder Haar and Roger Hoffer for their insightful evaluation of this work. Timothy Schneider and Denis O'Brien were instrumental in the development, application, and understanding of the Monte Carlo tools used herein. We are indebted to secretaries (both past and present) Sue Lini, Heather Smith, and Angie Narum, who were assigned the unenviable task of keeping this ship afloat. Valuable discussions and support regarding Lidar (in general) and LITE (in particular) were provided by Dave Winker and Mark Vaughan of NASA Langley Research Center. This work was supported in part by the DOD Center for Geosciences - Phase II at CIRA/CSU under grant # DAAH04-94-G-0420 and NASA Research Grant # NAG1-1702.

Contents

List of Figures

List of Tables

Chapter 1

INTRODUCTION

> "I can see nothing," said I, handing it back to my friend.
> "On the contrary, Watson, you can see everything. You fail, however, to reason from what you see. You are too timid in drawing your inferences."
> -Sherlock Holmes, *The Adventure of the Blue Carbuncle*

In the near future, active sensors such as Lidar [1] and Radar [2] will join passive sensors on space platforms for use in the remote sensing of the Earth's atmosphere. The Tropical Rainfall Measuring Mission Satellite (to be launched November, 1997) will be the very first environmental satellite to feature a precipitation radar instrument for use in rainfall remote sensing from space (Simpson *et al*, 1988). Active sensors have shown merit in their ability to penetrate optically thick media and hence obtain a vertical profile otherwise unachievable via passive sensors alone. Such detailed information is by and large unretrievable using the passive sensor, which can only resolve those atmospheric features which may be extracted from a scene representing an integration over the entire atmospheric column (a weighty task).

---

[1] LIDAR: Light Detection And Ranging

[2] RADAR: Radio-wave Detection And Ranging

At the same time, this information is vital to developing an understanding the full radiative effects of complex layered cloud morphologies, as well as the development and verification of cloud parameterizations in atmospheric models.

1.1 Motivation

Unlike the passive sensor, an active sensor *interacts* with the environment it is measuring, thereby eliminating some of the unknowns associated with the passive sensor scene-deconvolution issues. Unfortunately, the interactions which occur between the active sensor's signal and the targets that it encounters remain nontrivial, and the problems associated with inferring atmospheric properties from these retrievals are simply shifted to a new paradigm with respect to the passive sensor problems. The important difference between the two is that we (the user) maintain control over what the active sensors probes–we are the instigator of the measurement. While the signal is still at the mercy of the scattering/absorbing medium that it encounters, the underlying premise that the medium will respond to this external stimuli according to predictable, physical protocols leads to the conclusion that some of these properties should be inferable from the signal returns; provided that we are keen enough to find the runs in Mother Nature's stockings of obscurity.

This, in and of itself, is not enough to demarcate the regimes of utility between active and passive instruments, as many clever techniques have been developed to glean information from the atmospheric profile (for example, through the use of spectral absorption characteristics and weighting response functions) using the passive sensor as a stand-alone instrument. The capacity in which active sensors truly expand the inherent limitations of passive remote sensing is in their ability to resolve atmospheric features at very high spatial resolution. Having detailed information about the internal structure of cloud media not only enhances the physical understanding of their construct, but also improves the estimation of how they will

interact with their environment, in terms of cloud radiative "forcing" properties. For example, lower level water clouds are thought to cool the atmosphere by reflecting incoming solar radiation as well as radiating their ambient (and relatively warm) temperature to space. Thin cirrus clouds, on the other hand, have been shown to posses "insulator" qualities – allowing for downward transmission of incoming solar energy while absorbing up-welling infrared (thermal emissions from the surface and atmosphere below the cloud) and re-emitting this energy to space at a cooler temperature. These heating and cooling effects are said to be "forced" by the presence and characteristics of the clouds, and have immediate impact on atmospheric circulations. The ability to accurately locate the altitude of cloud tops and bases, the planetary boundary layer, temperature inversions, aerosol distributions, and detect the presence of multiple cloud layers, are among the many attributes of the active instrument. These features are oftentimes simply too embedded within the melee of contributing atmospheric constituents for a passive sensor to identify them unambiguously.

As mentioned, these products are not without their own array of caveats which must be addressed in the context of the active sensor. Understanding the nature of these relationships speaks volumes to the physical composition of the medium. This is at the heart of the "inverse problem" in atmospheric remote sensing; deducing specific properties of the environment given measurements of their indirect effects, or "footprints" in nature. It is up to the researcher, now cast in the role of a sleuth, to piece together the puzzle these measurements comprise and thereby identify what information exists therein. Certainly it would be a naive conviction to hold that all avenues of atmospheric remote sensing have been explored to exhaustion, even within the constraints of existing technologies. Implementation of an active sensor instrument on the space platform is one example of how an existing technology may be used with minimal modification to provide an entirely new source of information. That these data might yield new insight on our planet's complex atmosphere,

based on the success we have already enjoyed with the passive instruments, should represent a source of optimism in the science community.

1.2 The Scope of the Problem

In preparation for the imminent inclusion of space-borne active environmental sensors on the environmental satellite armada, the Lidar in Space Technology Experiment (LITE) was conducted in the Fall of 1994. As its name implies, the experiment's immediate goals centered on developing several technology aspects of operating a lidar instrument in the challenging space environment. Aside from exploring the many hardware issues relevant to the mission, a science team dedicated to optimizing the research utility of the actual LITE data was assembled. The lidar instrument operated for 10 days of the STS-64 mission, collecting observations of cloud and aerosol over nearly 1.5 million kilometers of ground track. This unique data set reveals many fascinating atmospheric details and features undetectable to existent passive sensors. The first images produced from the LITE data showed immediately the potential windfall of having an active sensor in space; displaying an extremely detailed profile of cloud, aerosol, topography, and even planetary boundary layer signatures in the clear atmosphere returns.

In addition to all the wonderful features expected of the data, some additional, less intuitive, artifacts in a subset of the cloud returns were also immediately apparent. These features might be described as anomalous "extensions" or "stretching" of the cloud bases, particularly in the regions of optically thick cloud. The extensions appear as streaks of fading return intensity and variable magnitude. Their classification as anomalies is founded by the observation that some of the pulse stretching features were observed to reach several kilometers below the bases of neighboring (but less optically thick) cloud structures, with returns often reaching well below the surface of the Earth. Also notable was the juxtaposition of clouds exhibiting

marked stretching features in the same vertical profile as clouds showing little or no extension signatures.

Such anomalies were initially hypothesized by hardware engineers to be a possible "ringing" effect associated with the system electronics (detector response). Winker and Poole (1995) of NASA Langley Research Center later conjectured that multiple scattering effects were in fact accounting for the observed pulse stretching. At orbit altitudes of 250km, even a small detector field of view (FOV) of 3.5 mrad results in a cloud-top footprint of nearly 1km. This allows for multiply-scattered photons to have a greater possibility of scattering back to the detector and contributing to the return signal. This effectively decreases the extinction coefficient σ_{ext} by a factor η, $(0.0 < \eta < 1.0)$. The effects of multiple scattering on a single-scatter ranging algorithm (as is used for most lidar and radar operations), to be developed herein, also explains the observed pulse stretching in some optically thick clouds.

1.3 The Focus of this Study

This study addressed the question of whether or not this "problem" of pulse stretching, owing to multiple scattering of the lidar beam, could be harnessed to yield any useful information about the physical properties of the cloud medium. Understanding the relationships between theoretically modeled pulse stretching as a function of certain cloud optical properties (identified as significant parameters in the scattering behavior of the lidar photons) is an essential step in assessing the practicality of this notion. To this end, pulse stretching dependency on cloud optical depth and selected phase function parameterizations were investigated as a preliminary survey of the problem–the ultimate goal being to lay the groundwork for a new tool in the retrieval of cloud optical properties.

Some of the immediate applications of such a product include:

- Given (*a priori*) the correct cloud base altitude, and given the pulse extension observed, conduct a direct retrieval of the relevant cloud optical properties.

- Given the optical properties via synergy with independent measurements, filter the pulse extensions from the data to yield a more accurate cloud base altitude.

- Approximation to cloud particle phase and distributions based on the pulse-stretching-retrieved "bulk asymmetry parameter" for the cloud medium.

- Using pulse stretching as an independent validation of passive sensor retrievals.

Addressing the role of the active sensor in space is a relevant endeavor, because the advent of their operation on this platform is an inevitable and necessary step in the evolution of remote sensing techniques. Understanding the behaviors unique to this particular platform will aid in optimizing the utility of the instrument and help to define the scope of its application. As stated, the examination of the lidar "pulse stretching problem" falls under the greater category of active remote sensor algorithm development. This study is a worthwhile effort, as it predates the first implementation of the lidar instrument on the space platform in an operational mode. Results of these modeling efforts will hopefully be of some benefit to the science community as it proceeds to grapple with this new source of data and all the idiosyncrasies inherent to it. It is hoped that this research will stimulate the interest required to pursue and truly characterize the full scope of challenges to active instruments in the brave new world of space.

1.4 The Hypothesis

This work defined the lidar pulse extension problem as its principle focus, but it is important not to lose sight of the big picture. While the active sensor already has shown its potential on the space platform, there exist many poorly-understood

processes which must be considered when interpreting the data. The simple fundamentals of how the active sensor operates has made it dangerously convenient to interpret the information it provides much too literally. For many, if not most, common applications of the active sensor, higher-order effects are too subtle to leave their signatures in the returns. The policy of "what you see is what you get", however, becomes a far less valid premise for long-range platforms, when the rules of the sensing system are adversely recast. The consequence of overlooking the multiple scattering effects inherent to the lidar instrument leads not only to an immediate misunderstanding (and hence, misuse) of the information, but also an *under-use*, in that there may exist a means of gaining further insight to the characteristics of the scattering media from these multiple scattering artifacts. This study hones in on some of these possibilities; in particular, the retrieval of the bulk scattering phase function asymmetry parameter and the spectral cloud extinction in terms of the observed pulse extensions in a variety of scattering media.

The big picture, of course, remains one that is fundamental to the remote sensing community; the development of new retrieval methodologies and refinement of existing retrieval techniques. The development of active sensor technologies on the space platform is germane to both of these issues. Addressing the lidar pulse stretching phenomenon should not be interpreted as an argument against the push for active sensors in space, but as an inspiration to explore and further our understanding of these "non-ideal" responses in anticipation of the day when such datasets become commonplace. Gaining formal quantifications of the space-borne lidar pulse extensions (and assessing the feasibility of their use) should aid in decisions regarding the refinement of the instrument either to eliminate or enhance these features in future applications.

1.5 Research Objectives

Several objectives defined the breadth of this work. While ambitious in their own right, they by no means exhaust the possible insights inferable from the lidar pulse stretching problem.

- Pose the finite beam (lidar) problem in a "first order" representation from a Monte Carlo perspective. developed and refined from existing Monte Carlo code.

- Design experiments with this model to understand multiple scattering behavior in terms of idealized cloud optical parameters.

- Understand what kinds of information are contained within the multiple scattering, and how it may be used:

    1. Record photon path histories and used to determine mean photon path lengths, extended path distances with respect to single scatter events, and cases of cloud base extension due to significant multiple scattering.

    2. Employ Takano & Liou ray-tracing phase function for ice-crystals (described in detail herein), comparing pulse extension results to Deirmendjian C1 (water cloud) and empirical single/double Henyey-Greenstein scattering phase function parameterizations (often used in models as first order approximations to true scattering phase function behaviors).

    3. Explore the possibility of using the pulse stretching data to derive a parametric phase function that is representative of the retrieved asymmetry parameter.

    4. Example of a retrieval that uses this additional phase function information to improve the retrieval of cloud optical depth

5. Quantify how accurately we need to know the pulse extensions in order to make them useful for retrievals.

- Investigate pulse stretching relationships in three-dimensional, inhomogeneous cloud media.

- Formulate a hypothetical experiment that would test the results of this work.

1.6 Methodology

This thesis investigates multiple scattering behaviors and how they in turn lead to the observed pulse stretching features observed in space-borne lidar returns. The order of operations taken towards supporting or refuting the hypothesis and fulfilling the research objectives as stated was intended to adhere as faithfully as possible to the constructs of the "scientific method". The methodology described has both advantages and limitations which shall be addressed in context. The goal of this research was not to produce an operational-level retrieval algorithm based on the pulse stretching measurements, but instead to help lay the theoretical groundwork necessary to this end. The leap to application of these theoretical results requires a verification data set, including true cloud base altitudes and an independent evaluation of the cloud micro-physics and extinction properties (which are obtainable from standard FSSP and millimeter cloud radar instruments, respectively). The binding relationships which dictate the behavior of lidar pulse extensions are the subject of this work, and are readily characterized from a largely theoretical approach.

To examine pulse stretching, a suitable model-environment capable of representing the lidar problem was necessary. The Monte Carlo solution to the radiative transfer equation was chosen because it is readily transformed from the traditional solar problem into the lidar (finite source) case, and relevant features such as path length distributions and higher-order scatter contributions are immediate

by-products of the photon simulations. The forward versus backward Monte Carlo implementation for the lidar problem was investigated, in the interest of both computational efficiency and physical intuitiveness.

In order to examine multiple scattering behaviors as a function of cloud optical properties, several cases spanning a wide range of properties were run. The initial focus was to understand, in the most general sense, which scattering events were contributing, where in the medium they were occurring, and *when* (with respect to the lidar ranging technique). Also of relevance to this problem is the photon path length distribution which gives an idea of the geometric distances traveled as a function of scattering order and cloud optical properties, and a proxy to the expected degree of pulse stretching.

The results of the cases were then used to calculate the below-cloud-base (referred to herein as "pulse extension") returns from the lidar instrument at orbit altitudes. The degree of pulse extension for these case studies were used to understand exactly what was (and was not) retrievable from these signatures. Binning the contributions to the signal return as a function of scattering order, round-trip travel distance, and a variety of cloud variables, the physical behavior of pulse stretching may be captured and quantified. Based on the sensitivity of the modeled extensions to cloud optical properties, the requirements for lidar vertical resolution (in the interest of resolving the pulse extension features for use in inferring the cloud properties necessary to create them) were then established.

As an additional exercise, the ray-trace-generated scattering phase functions of Takano & Liou were incorporated into the Monte Carlo model to examine the multiple scattering behaviors of various idealized ice crystal geometries. While it is readily conceded that ice clouds do not consist entirely of a single ice crystal geometry, the study nevertheless provides a insightful comparison between ice and water clouds. Having modeled the pulse stretching effects in terms of the driving

cloud optical properties (the forward problem), the question of retrievability (the inverse problem) was discussed. Based on the specific needs established for such a retrieval, a hypothetical experiment designed to use the lidar pulse extensions in a validation study was outlined. A second LITE mission has been planned to fly in the late 1990's, providing an opportunity to comprehensively examine the pulse extension effects with additional independent information from other instruments in an Intensive Observation Period (IOP) scenario.

1.7 New Results

The new results of this research center around the quantification of the lidar pulse stretching phenomenon (at Space Shuttle orbit altitudes of 250km) in terms of the optical properties of the cloud media. The results indicate that quantifying the relationship between multiple scattering effects and optical properties particular to the scattering medium is a tractable problem. Scattering behavior in idealized cloud media, while not immediately translatable to the complexity of three-dimensional real world cloud structures, remains valid as an initial survey of how the characteristics of the cloud are contributing to the pulse stretching signals observed. Implementation of ice crystal phase functions produced by Takano & Liou have also been used in this study for pulse extension modeling; which to the author's knowledge is the first application of these ray-tracing data in this particular capacity. Perhaps most importantly, an outline of how pulse-stretching/cloud-parameter relationships may be exploited in retrievals is provided.

1.8 Chapter Outline

An introduction to the lidar instrument and its implementation on the space platform (LITE, September 1994) opens the paper in Chapter 2, followed by an investigation of the physics behind the lidar pulse stretching artifacts in Chapter 3. The

fundamental theory of the Monte Carlo approach to solving the radiative transfer problem is explained in Chapter 4, and its refinement to the "finite beam" of the lidar problem is detailed in Chapter 5 . Chapter 6 investigates some of the model sensitivities associated with various multiple scattering effects in terms of selected cloud optical properties. The actual pulse extension results are presented in Chapter 7. A discussion of the utility of these results (and the limitations of their applicability due to simplifying assumptions), along with an outline for a possible field experiment (centered on generating the multi-sensor data set necessary to effectively test cloud parameter retrievability) follows in Chapter 8. Chapter 9 concludes with a summary of the more salient aspects of the research and its findings and a few words towards the utility of active sensors on the space platform in future research.

Chapter 2

THE ACTIVE SENSOR

Active sensors are not a new tool in atmospheric remote sensing (the lidar itself has been used in this capacity for nearly three decades). While this technology has been developed and implemented with success on the operational level in terrestrial and airborne applications, it has yet to find its place in the space environment. This has been due largely to the increased demands of active sensors over passive sensors in terms of power, size, and maintenance requirements. Technological advances have poised the science community to seriously consider the merits of active sensors on the space platform. This was the motivation for the experiments described herein.

2.1 The Lidar Instrument

The active sensor modeled in this research is the Light Detection and Ranging (lidar) instrument. Similar to the conventional radar, the lidar uses electro-magnetic radiation (UV,visible or infrared) wavelengths instead of radio wavelengths as its transmission signal, and measures the returned power (after amplification) at some hardware-specified sampling interval time. The discretized sampling "range bins" are mappable to physical locations in space, and return power is thereby attributed to the backscattering targets accordingly. Because of its operating wavelengths and detector sensitivity, the lidar is capable is resolving atmospheric signatures down to the molecular (Rayleigh regime) level.

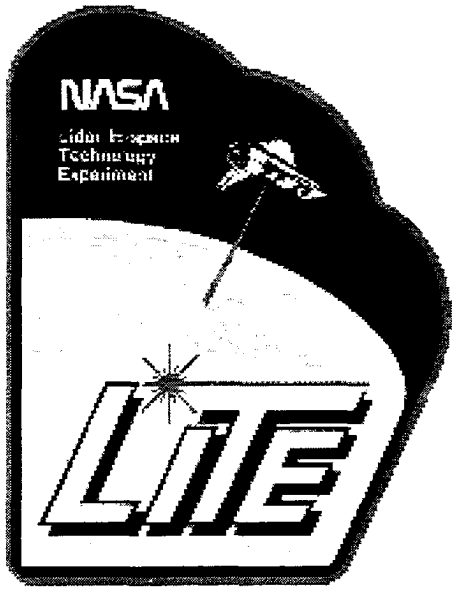

Figure 2.1: The LITE Mission was flown on the Space Shuttle Discovery during September, 1994

Table 2.1 summarizes the main hardware features of the lidar instrument flown for LITE. The instrument is comprised of a laser transmitter module (LTM), a coaxial receiving telescope (the detector) with a receiving optics/electronics assembly, and supporting electronic sub-assemblies. The laser transmitter is comprised of two redundant, flash-pumped and Q-switched Neodymium:yttrium-aluminum-garnet (ND:YAG) lasers, with doubling and tripling crystals employed to convert the fundamental operation transition wavelength of 1064 nanometers into second and third harmonics at 532 and 355 nanometers. The detector is a Cassegrain telescope with a 1 meter diameter primary mirror, which directs the return signal onto photo-multipliers (for second and third harmonics) or onto an avalanche photo-diode for the 1064 nm detector. The detector field of view (FOV) is selectable (1.1 mrad for daytime use or 3.5 mrad for nighttime use) via an aperture stop. The range resolution of the instrument is approximately 15 meters.

The advantages of lidar over currently implemented polar orbiting and geostationary radiometer instruments are numerous. In addition to the listing of attributes

Output Wavelength:	1064nm,532nm,355nm
Output Energy:	486mJ, 460mJ, 196mJ, respective to above
Laser Pulse Length:	27ns, 27ns, 31ns respective to above
Pulses-per-second (PRF):	10
Maximum Unambiguous Range:	14990km
Sampling Interval:	15m
Space Between Pulses:	0.740km
Laser Beam Divergence:	0.6mrad @ 532nm,355nm; 1.0mrad @ 1064nm
Laser Beam Footprint:	(range dependent)
Detector Field of View:	Selectable 1.1mrad, 3.5mrad (night). Opaque
Detector Footprint:	(range dependent)
Primary Mirror Diameter:	0.985m

Table 2.1: The LITE mission instrument specifications

above, the lidar has fewer temporal and spatial restrictions on its sensing capabilities as compared with passive instruments operating in at visible and near-infrared wavelengths (owing to dependencies on external illumination sources). However, the presence of these sources can have detrimental effects to the utility of the lidar instrument when it is attempting to detect its own signal amidst a sea of scattered solar energy also present over the detector bandwidth. A variable detector field of view narrowed from 3.5 mrad (nighttime operation) to 1.1 mrad for daytime operation served to minimize these effects during the LITE mission, but the cleanest and most useful lidar returns were obtained from nighttime orbit data.

2.2 The LITE Mission: An Overview

The Lidar in Space Technology Experiment (LITE) was flown on the Space Shuttle Discovery over the period of September 9-20, 1994. It was the first of several missions involving the lidar instrument, planned to fly on one to two-year intervals. The main payload of this mission was the lidar assembly as described above. The entire package was mounted on a rigid space-lab pallet. This unit was loaded inside Discovery's cargo bay and, during operation, the shuttle was oriented such that when

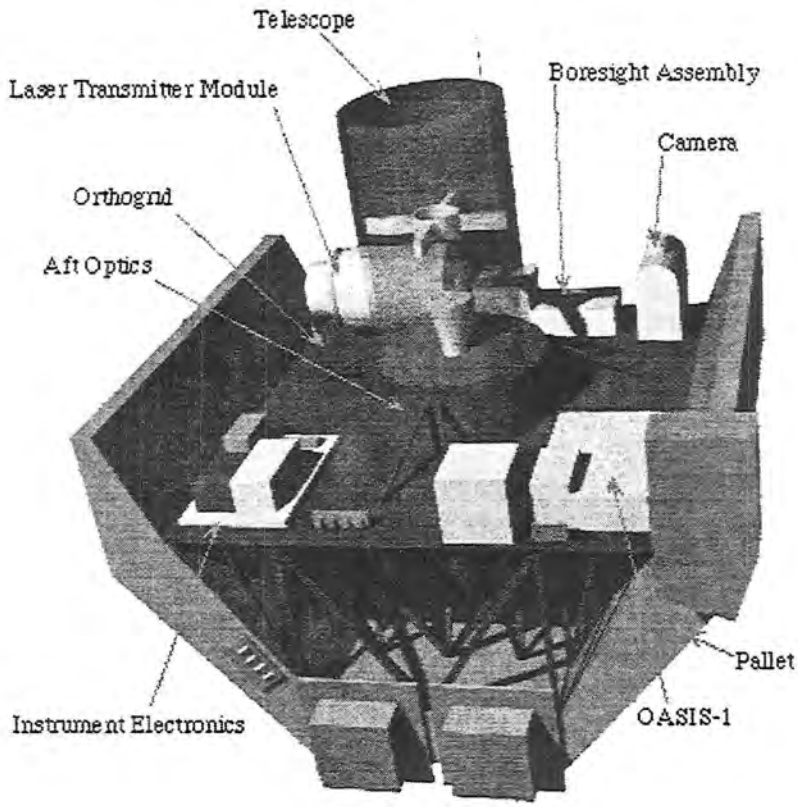

Figure 2.2: Components of the LITE assembly (Courtesy of NASA Langley Research Center)

the bay doors were opened the lidar viewed nadir to the Earth surface. The shuttle orbited the Earth at a 57-degree inclination angle, resulting in a highly precessive orbit–crossing the equator at a separation of 2500 km in successive orbits. The precession allowed for investigating the diurnal operation of the instrument. Table 2.2 describes the orbit properties of the STS-64 mission.

There are many remote sensing products which a lidar instrument may obtain on a global-scale and with relative ease if implemented on a space platform. Some are listed here:

1. Providing important information about cloud vertical structures, cloud distributions, backscatter/extinction properties, and developing a global cloud climatology.

Orbit Speed:	7.4km/s
Altitude:	256km
Period:	90min
Orbit Inclination:	57^{o}

Table 2.2: The LITE Mission Orbit Specifications

2. Probing below optically thinner cloud structures and between broken cloud fields.

3. Sub-visible cirrus (important for CRF) detection. Applications to contamination in surface imagery data (*eg* LANDSAT imagery– vegetation/soil classification studies).

4. A global aerosol (tropospheric and stratospheric) climatology.

5. Planetary Boundary Layer (PBL) and Tropopause detection, height and optical properties.

6. Ocean and stream probing, altimetry.

7. Atmospheric density/temperature studies, planetary and gravity wave detection.

8. Temperature and density profiles.

9. Energy transport, ozone transport, large scale circulation studies.

10. Altitude registration for other satellite-based instruments.

Because LITE was designed as a "technology experiment" (meaning that its main objective was to serve as a test-bed for the operational mechanics and instrumental design associated with developing space-based lidar instruments), the principle focus was on monitoring the system operations: thermal control, autonomous operation capability, general performance, noise studies with the laser transmitter

module (LTM) off, etcetera. Actual scientific applications were also considered and a science team was formed; headed by Drs. Tim Suttles (Chairman), Pat McCormick (Project Scientist), and Dave Winker (Deputy Project Scientist), in the interest of gaining as much scientific insight from the hardware-oriented technology experiment as possible.

The LITE 356nm and the 532nm channels were tuned specifically for detection of molecular-scale atmospheric targets. Consequently, backscatter imagery of the larger cloud particles for these channel returns were saturated (the lower-power returns are amplified to a level beyond the maximum unambiguous signal of the detector, making different levels of backscatter signal indiscernible) for a majority of the cloud returns. Only in the thinnest cloud cases encountered (mostly in regions of sub-visible cirrus clouds) did the signal yield a unsaturated return. Because the two high-gain channels (and 532nm channel in particular) were operated more extensively than the 1064nm channel, cloud backscatter properties and extinction profiles were often unretrievable. Only the most ostensible features of the cloud layers (such as base and top heights) were derivable. For the qualitative identification of pulse extensions, however, the high gain operation mode was not instrumental, as it served to accentuate the the weak-signal features of interest. Future-planned missions for the lidar on the space platform, building on the experience of LITE, will shift more emphasis to scientific objectives and more extensive investigation of the measurement capabilities of the instrument. Multiple scattering effects (which lead to the pulse stretching signals) will certainly be a focus of these future experiments.

2.3 Summary

A lidar was operated on the Space Shuttle Discovery in September 1994 for the Lidar In-space Technology Experiment. It represented the first civilian attempt at implementing of this instrument on the space platform. There are many atmospheric

features that are readily detectable by the lidar above and beyond what current sounder and occultation instruments are capable of measuring. While LITE's main focus was on hardware evaluation and instrument characteristics unique to active remote sensing in the space environment, the atmospheric backscatter data taken over the course of the mission showed a great deal of potential for the operational utility of the lidar in space. This was the first of several proposed follow-on missions planned to be conducted at 1 to 2 year intervals, with each subsequent mission building upon the knowledge gained from its predecessors and exploring further the remote sensing capabilities and limitations of lidar in space. The ultimate goal of this series of experiments is the eventual installation of an autonomous space-borne lidar system for environmental research purposes.

Chapter 3

LIDAR PULSE STRETCHING: A PHYSICAL BASIS

As previously stated, one of the goals of this research effort is to quantify the effects of multiple scattering on the correct ranging of cloud base altitudes as detected from a lidar on a space-platform. Because of the significant laser beam footprint at cloud top that results from a finite (non-zero) beam divergence at large distances (orbit altitudes on LITE meant ranges in excess of 250km) from the targets and the necessarily large field of view required for sufficient collection of backscattered photons, multiple scattering (MS) effects cannot be neglected. This is an unavoidable problem for any active sensor operating at most any orbit altitude. The problem is of lesser importance for non-satellite platforms because the beam divergence and detector field-of-view remain relatively columnar (negligible divergence) at shorter operating distances. In this chapter, the pulse-extension phenomenon is explained in terms of the multiple scattering effects.

3.1 The *Rub*: Multiple Scattering

Multiple scattering effects on lidar returns were first documented by Donchenko *et al* (1971) and Kaul and Samokhalov (1975). The effect that MS has on apparent cloud base extension is straightforward. Not unlike a conventional radar system, the ranging software package used to process lidar signal returns represents the columnar

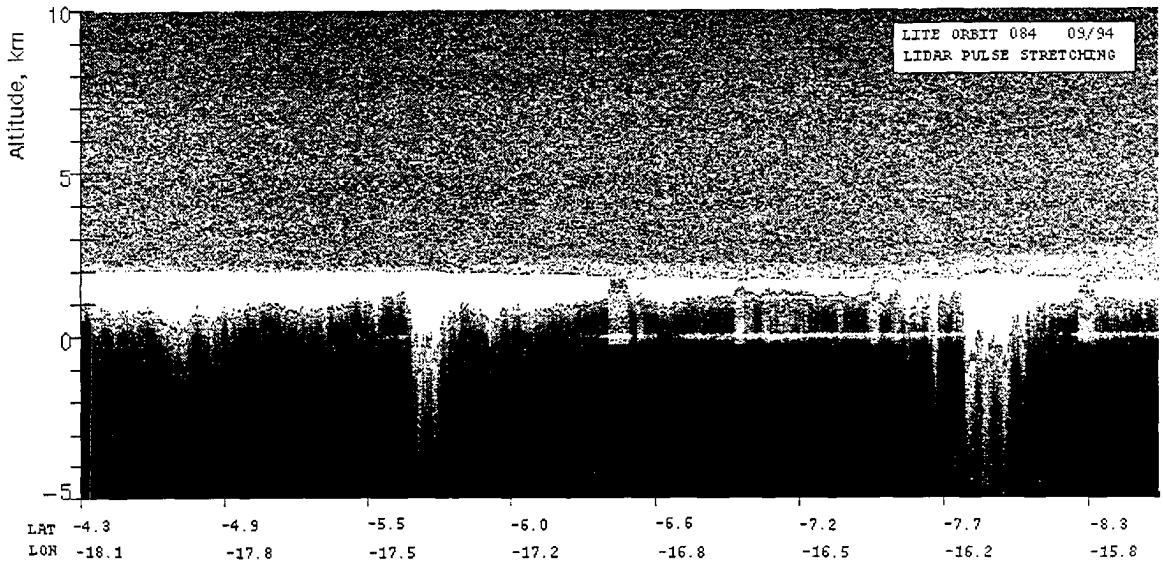

Figure 3.1: Raw count return from Orbit 084 (over the Equatorial Atlantic) showing marine stratus cloud base extensions (Courtesy of NASA Langley Research Center)

path of the laser beam trajectory as a discrete series of adjacent "range bins." The rate of travel for the photons is known (the speed of light, $c = 2.998 * 10^8$ m/s), so when a "salvo" (group) of photons is fired from the source, the time of return at the detector is directly mappable to the round-trip distance required for that signal to have traveled out to the the target, backscattered once, and returned back to the detector telescope. The listening time of the detector is much longer than the duration of a pulse, and the sampling rate of the detected signal determines the vertical resolution of the profile recovered. In the case of the lidar used in LITE, the 200 MHz bandwidth limits the range resolution of the instrument at approximately 15 meters.

In a idealized (to the lidar application) universe, single scattering events would reign; a photon would either bounce off of a particle once and return directly back to the detector without further scattering activity, or it would never return (single-scattered in some direction that does not trace back to the detector, or never scattered at all). In this unrealistic scenario (and neglecting the finite beam divergence),

a range-detection algorithm based on a two-way distance of travel (source to target and back to source) would precisely range the scattering event in physical space. It is also assumed that changes in the index of refraction of the atmosphere (which tends to "slow down" the speed of light in the lower layers of the atmosphere) is a negligible factor. For a standard atmosphere, the index of refraction at sea level is approximately $n = c/v = 1.0003$. or a difference of about 0.03 percent with respect to a vacuum environment. This roughly corresponds to a mis-ranging bias of 4.5cm in the range bins closest to the surface. Considering the range resolution of the lidar instrument and the rapid decay of higher indices of refraction with height AGL, the assumption of c = constant is probably a reasonable one to make here. For the nadir-pointing LITE instrument, the range as derived by the two-way travel time directly pinpoints the location of the scattering target with respect to the instrument. Together with surface returns, the altitude of the target is thereby immediately prescribed.

Unfortunately, the real world is far less accommodating than the idealized case offered by a single scattering universe. Depending on the optical properties of the medium and detector geometry of the instrument, photons may encounter a plethora of scattering targets before returning to the detector. With each additional scattering event beyond first-order (a single scatter event), additional distance to the photon's path length is accrued in excess of what its single scattering photon path distance would have been (with exception to scattering which results in no change in photon trajectory–a purely forward scatter). If these multiply-scattered photons do in fact return to the lidar detector they are, by definition, contaminated in the context of a single-scatter assumption. If the temporal delay is large enough (depending on the range resolution of the instrument), their energy will be attributed to a different range volume; further away from the bin in which they first scattered. This results in a mis-ranging of the vertical distribution of backscattering targets in

the medium. In the case where many photons undergo high orders of scatter and contribute significantly to the return signal, ambiguity in the assignment of a correct range becomes a problem. Once multiple scattering contributions to the lidar return signal become significant with respect to first order scatter returns, detailed vertical profiles of the medium are no longer obtainable (since MS is contaminating the entire profile of the medium).

3.1.1 The Consequences

It is readily apparent that as the multiple scattering phenomenon increases, the interpretation of ranging algorithm on the whereabouts of the scattering origins begins to suffer greatly. For a nadir-oriented lidar system, targets near the top of the medium are ranged correctly since low orders of backscatter will escape readily to less optically thick regions above the medium (thereby avoiding the accumulation of additional photon path distance). To understand the physical meaning of the "optical thickness" of a medium, one must consider the concept of extinction. Consider a collimated (non-diffuse, having a clearly defined direction) beam of light impinging upon a collection of scatterers (dust, water droplets, etc.) and a detector oriented such that it may view this beam from the opposite side of the medium. The extinction of this beam due to the presence of the optically attenuating media is a result of two factors: 1) scattering, and 2) absorption. The direction of photon travel with respect to the detector instrument is of primary importance, because extinction does not necessarily insinuate that the photon was absorbed by the particles. If a photon is scattered away from the viewing area of interest it will not be received by the detector and is therefore considered as extinct. Specular optical path is a measure of the medium's ensemble extinction properties along a geometric path (s', s'') through the medium, specified for a single wavelength. It is an integration of the specular volume extinction coefficient along this path, and expressed mathematically as:

$$\tau_\lambda(s', s'') = \int_{s'}^{s''} \sigma_{ext,\lambda}(s)\, ds \tag{3.1}$$

It is common practice to represent the integrated cloud extinction in terms of an optical *depth*, which is simply an equivalent optical path along the vertical (assuming a plane parallel, horizontally homogeneous atmosphere):

$$\tau_\lambda(z', z'') = \frac{\tau_\lambda(s', s'')}{cos\theta} \tag{3.2}$$

where θ is the zenith angle.

The scattering properties of particles are as diverse and complex as the media themselves, but do possess characteristics unique to their habits and geometries. The single-scatter phase function, $P(\theta)$, characterizes the angles of preferred scattering by a particle. Formally, it is a probability density function defined over the range of scattering zenith angles between 0 (complete forward scatter) and 180 (complete backscatter) degrees. While this assumption need not be true for a preferentially-oriented non-spherical particle distribution, the azimuthal-dependence on scattering is usually neglected.

Unless there is another scattering media above the cloud/aerosol layer in question, the incident (with respect to the lidar beam) boundary of the scattering layer is immune to additional energy from MS effects, since MS can only result in delayed returns (ranged deeper into the medium). However, the deeper a photon penetrates into an optically thick medium the less likely it is that it will experience a single-scattering path history. Rather, it is more likely to undergo several scattering events; each one redirecting its trajectory according to the scattering properties of the physical medium, until its ultimate fate is decided either by absorption, scattering away from any possible reunion with the detector, or successfully returning to the detector. While the first two possibilities dominate in probability (due to the tendency for strongly forward-peaked scattering by particles of interest, and the miniscule size of the solid angle of collection area itself) the shear number of photons fired in a lidar pulse maintains the possibility that photons will return to the detector even after running the gauntlet of multiple scattering.

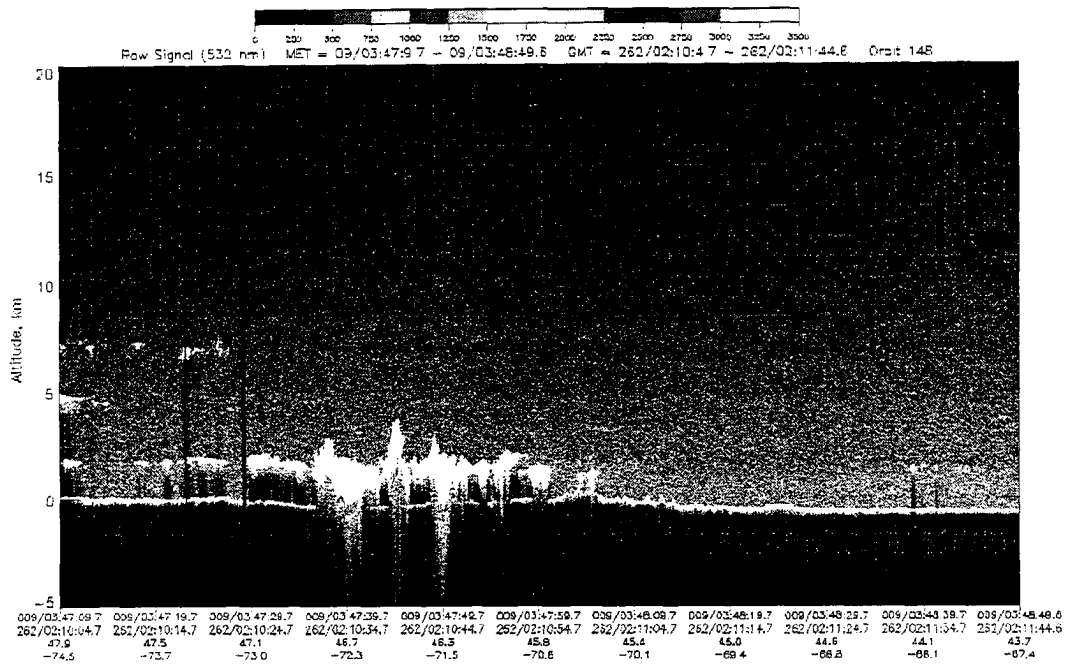

Figure 3.2: Raw signal return from LITE Orbit 148 (over Nova Scotia) showing cloud base extensions exceeding −4.0 km below the surface

Additionally, MS effects will increase the probability of photons returning to the detector by recapturing a subset of the stray photons. Instead of escaping the medium to the sides or below, a relatively higher number of photons will rattle around in a more localized area in the vicinity of the detector field of view–increasing the possibilities of just the right scattering event occurring which directs the photon back to the detector. When viewing the problem from a photon-by-photon standpoint, the task of successfully receiving a sufficient number of photons back to the detector to obtain a detectable signal appears to be one of insurmountable inefficiency. Considering again the vast number of photons fired in any single lidar pulse, however, these unlikely events add up quickly in a statistical sense. The modeling of this phenomenon on computer workstations, requires invoking strategies of variance reduction (discussed in Chapter 4) in order to achieve in a reasonable amount of time (tens of minutes to hours) what Mother Nature does instantly.

The manifestation of these multiply-scattered photon contributions to the space-borne lidar application is the observed "pulse stretching" observed in so much of the backscatter imagery. These extensions occur primarily in the optically thick regions of cloud media, as a significant number of photons travel extended distances within the detector field of view before returning to the instrument. Cloud base extensions on the order of several kilometers have been observed in much of the LITE imagery, often accompanied by such oddities as cloud base returns in excess of five kilometers *below* the Earth's crust! (See Figure 3.1) These are not fleeting artifacts, and have been observed to occur over both continental and maritime airmass, pre- and post-frontal cloud structures, and over a wide range of cloud type throughout the vertical. Because of LITE's global coverage, an extensive data base encompassing a wide variety of cloud scenarios exists. The examples included herein are but a snapshot of the multitude of pulse stretching cases observed in this single data set.

The enhancement of the multiple-scattered contributions to the signal will naturally increase with an increasing detector "collection area". Radially-scattered photons will quickly leave the field-of-view of a narrow-aperture detector, while having a greater chance of contributing for larger viewing detectors. Of course, these radially-scattered photons will also be characterized by longer photon path lengths, and hence will be ranged at further distances accordingly. By virtue of its enhanced ability to collect radially-scattered photons, it may be safely conjectured that larger FOV detectors should accentuate the lidar pulse extension phenomenon, while successively narrower FOV detectors will minimize this effect. Speaking to this issue, Platt and Winker (1996) present LITE imagery showing notable decreases in pulse extensions when switching from a 3.5 mrad to a 1.1 mrad receiver field aperture.

3.2 Summary

The lidar pulse extension phenomenon may be understood in the context of photon multiple-scattering occurring within the scattering media. The simple ranging

algorithm employed to locate targets in physical space is based on the assumption of two-way geometric travel distance (from the source, scattering off the target, and returning to the detector), and is insufficient for long-range operations. Due to hardware limitations, ground eye-safety, and signal to noise requirements, the necessary lidar beam/detector geometries lend themselves to significant multiple scattering effects when applied to orbit ranges. These effects manifest themselves in the observed pulse stretching phenomenon, which is an unknown function of both the optical properties of the scattering medium (*eg*, cloud extinction and scattering phase function properties) and the instrument optics. If it is possible to numerically identify fundamental pulse stretching behaviors in terms of these driving cloud parameters, their retrievals via inversion techniques may be possible.

Chapter 4

MONTE CARLO THEORY

Investigation of the problem at hand boils down to obtaining a detailed understanding of how photons travel within the scattering medium (having arbitrary optical properties). Knowledge of the integrated (over all scattering orders) signal, while helpful, is not sufficient in understanding the interactions that lead to pulse stretching in lidar returns. Developing an understanding of the multiple scattering behaviors within the cloud in a quantitative, discretized, and physical way necessitated the use of a computer model capable of keeping track of the photons histories on a scatter-by-scatter basis. A statistical archive of photon path histories (a photon path-length distribution) as a function of the optical properties of the cloud is required to characterize the pulse stretching phenomenon.

The problem is well-suited to the Monte Carlo solution to the radiative transfer equation, which uses a stochastic approach to model the signal contributions from all relevant orders of scattering. It is the ability to decompose and examine the individual contributions that makes Monte Carlo methods attractive, despite their computational inefficiency with respect to analytical techniques. First developed in the burgeoning atomic-era, the term "Monte Carlo" was coined in reference to the seemingly random behavior of photon trajectories observed during nuclear reaction processes–not unlike the randomness encountered in so many games of chance. Since Monte Carlo, France was a major hub of gambling activity at the time of

these experiments, the name found its niche in the annals of radiative transfer vernacular. The Monte Carlo technique has been used by many modelers of the lidar problem, including most recently an international panel of scientists participating in the MUSCLE [1] workshop group for the purpose of quantifying multiple scattering contributions to lidar returns (Bissonnette *et al* (1995)). This chapter covers the main points of the Monte Carlo algorithm in the context of radiative transfer theory: addressing its efficiency, its inherent strengths and shortcomings, and its utility in the context of the pulse stretching problem.

4.1 Statistical Radiative Transfer

The equation for transfer of electro-magnetic radiation at position $\vec{x}$ and traveling in direction $\vec{s}$ through a scattering, non-emitting medium may be expressed succinctly as

$$\vec{s} \cdot \nabla I(\vec{x}, \vec{s}) = -\sigma_{ext}(\vec{x}) I(\vec{x}, \vec{s}) + \sigma_{sca}(\vec{x}) \int_{\Omega} \mathcal{P}(\vec{x}, \vec{s}, \vec{s}') I(\vec{x}, \vec{s}') \, d\Omega(\vec{s}') \tag{4.1}$$

where σ_{ext} is the total extinction coefficient σ_{sca} is the scattering coefficient (both are assumed to be dependent upon the position in the medium), related with the absorption coefficient σ_{abs} as follows:

$$\sigma_{ext} = \sigma_{sca} + \sigma_{abs} \tag{4.2}$$

The first term on the right hand side of equation 4.1 represents the loss of radiation in direction $\vec{s}$ due to both absorption and scattering according to Lambert's law of extinction.

$$dI_{\lambda} = -\sigma_{ext,\lambda} I_{\lambda} d\vec{s} \tag{4.3}$$

Where the subscript λ indicates that these are wavelength-dependent quantities (this dependency is implicit throughout the following discussions, and the λ subscript in

---

[1] MUSCLE is an acronym for MUltiple SCattering Lidar Experiments

following equations shall be omitted for the sake of brevity). The second term on the right hand side of 4.1represents the scattering of radiation into the direction of $\vec{s}$. This is determined by the scattering phase function, $\mathcal{P}(\vec{x}, \vec{s}, \vec{s}')$, (allowed here to be a position-dependent quantity) which gives the cumulative probability "η" of radiation traveling in direction $\vec{s}'$ being scattered by a particle into a new direction $\vec{s}$.

The scattering phase function (for tradition and computational ease more than for physical soundness) is assumed to be azimuthally (ϕ) independent, and hence varies only as a function of the angle formed between the incident direction ($\vec{s}'$) and the new direction ($\vec{s}$). This angle is termed in the literature as the "scattering angle", Θ, and is represented mathematically as

$$cos(\Theta) = \vec{s} \cdot \vec{s}' \tag{4.4}$$

In the Monte Carlo algorithm, it is this scattering phase function which governs the nature of the "random walk" through the medium. Most cloud particle scattering phase functions exhibit a strong forward scattering peak, a weaker back-scattering lobe, a relatively weak normal-plane scattering regime, and an array of higher frequency features (*eg* halos and glories) characteristic of the particle phase (ice/water) and geometry. Several scattering phase functions were applied to the modeling of the lidar pulse extensions, ranging from isotropic (no preferential scattering direction) to highly anisotropic ice crystal (cirrus cloud) scattering phase functions which feature extremely sharp forward-scattering peaks.

Equation 4.1 is integrated over the full solid angle (4π steradians), with

$$d\Omega(\vec{s}') = sin(\theta')\, d\theta' d\phi' \tag{4.5}$$

to account for all possible incident radiation which may be scattered into the direction of our interest, $\vec{s}$. It should be noted that integration of the scattering phase

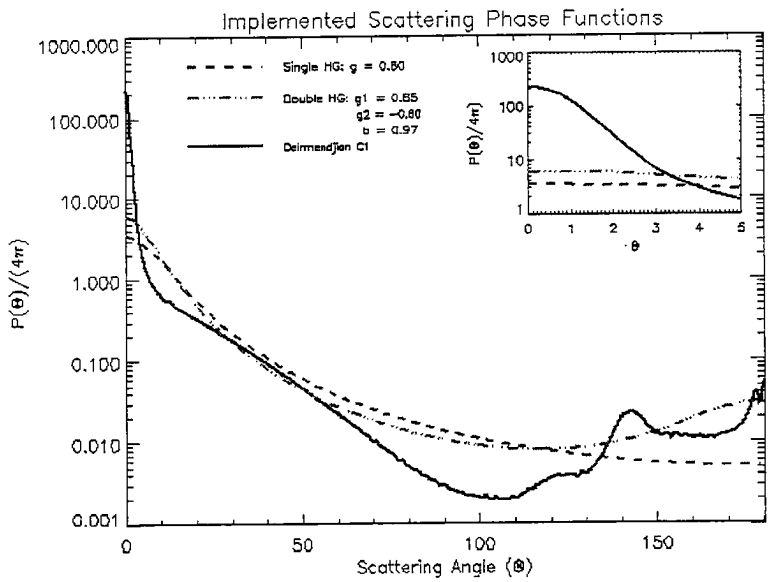

Figure 4.1: Comparison of analytical and Lorentz-Mie generated single-scattering phase functions

function over $d\Omega$ is equal to unity (as is required of any probability density function).

$$\frac{1}{4\pi}\int_{\Omega}\mathcal{P}(\vec{x},\vec{s},\vec{s}')\,d\Omega(\vec{s}') = 1.0 \tag{4.6}$$

Figure 4.1 shows single and double Henyey-Greenstein phase functions used in this study compared with the Deirmendjian C1 phase function. This plot reveals the dramatic differences in scattering properties from case to case. The forward scattering peak of the phase functions increases from single to double HG, with the DC1 exhibiting the strongest forward peak. While the analytic (HG) phase functions are well-suited to many radiative transfer codes, it is evident that they approach the "real" phase function structures only in the most general sense.

The integral form of the radiative transfer equation may be used to describe the radiance at any point, $\vec{x}_o$, and direction, $\vec{s}_o$ within the medium. Given a geometric

position $\vec{u}_\circ$ upon the boundary of the medium and integrating along the direction $\int$ to the interior point $\vec{x}_\circ$. the RTE may be written as:

$$I(\vec{x}_\circ, \vec{s}_\circ) = \mathcal{T}(\vec{x}_\circ, \vec{u}_\circ) I(\vec{u}_\circ, \vec{s}_\circ) + \int_{\vec{u}_\circ}^{\vec{x}_\circ} \mathcal{T}(\vec{x}_\circ, \vec{x}') \sigma_{sca}(\vec{x}') \times \int_\Omega I(\vec{x}', \vec{s}') \mathcal{P}(\vec{(x)}, \vec{s}_\circ, \vec{s}')\, d\Omega(\vec{s}') d\vec{x}' \tag{4.7}$$

where the beam transmittance between points $\vec{a}$ and $\vec{b}$ is given by

$$\mathcal{T}(\vec{b}, \vec{a}) = e^{-\tau(\vec{b}, \vec{a})} \tag{4.8}$$

where the optical path length between the two points is

$$\tau(\vec{b}, \vec{a}) = \int_{\vec{a}}^{\vec{b}} \sigma_{ext}(x)\, dx \tag{4.9}$$

The angular-dependent radiation (radiance) incident upon the detector (given by equation 4.7) represents the sum of contributions from all orders of scattering

$$\tilde{I}_K = \sum_{k=0}^{K} I_k \tag{4.10}$$

where $\tilde{I}_K$ represents the K^{th} partial sum of the multiple scattering series, and approaches the true radiance as $K \to \infty$. The residual (error) is simply the difference between the true radiance and the estimate, $\tilde{I}_K$. It is well known that random Monte Carlo estimation of integrals in the multiple scattering series has order $N^{-1/2}$, where N is the number of photon trajectories (quadrature points) simulated in the evaluation. Note that $I_{k=0}(\vec{x}_\circ, \vec{s}_\circ)$ describes any contribution to the observed intensity which did not interact with the medium during its commute to position $\vec{x}_\circ$ (it just transmitted directly to $\vec{x}_\circ$ from the boundary).

$$I_{k=0}(\vec{x}_\circ, \vec{s}_\circ) = \mathcal{T}(\vec{x}_\circ, \vec{u}_\circ) I(\vec{u}_\circ), \vec{s}_\circ) \tag{4.11}$$

The solution to the multiple scattering series is obtained by iterating 4.7 through K orders of scatter such that the K^{th} order contribution ($K \geq 1$) to the radiance

(the contribution which has been scattered K times) is given by

$$\begin{aligned} I_K(\vec{x}_\circ, \vec{s}_\circ) &= \int_{\vec{u}_\circ}^{\vec{x}_\circ} \mathcal{T}(\vec{x}_\circ, \vec{x}_1)\sigma_{sca}(\vec{x}_1)\, d\vec{x}_1 \\ &\quad \times \int_\Omega \mathcal{P}(\vec{x}_1, \vec{s}_\circ, \vec{s}_1) d\Omega(\vec{s}_1) \cdots \int_{\vec{u}_{K-1}}^{\vec{x}_{K-1}} \mathcal{T}(\vec{x}_{K-1}, \vec{x}_K)\sigma_{sca}(\vec{x}_k)\, d\vec{x}_k \\ &\quad \times \int_\Omega \mathcal{P}(\vec{x}_K, \vec{s}_{K-1}, \vec{s}_K)\mathcal{T}(\vec{x}_K, \vec{u}_K) I(\vec{u}_K, \vec{s}_K)\, d\Omega(\vec{s}_K) \end{aligned} \tag{4.12}$$

where we have started with an incident radiance at boundary point $\vec{u}_K$ heading in direction $\vec{s}_K$ and traveled through the medium over K orders of scatter to finally arrive at position $\vec{x}_\circ$ and in direction $\vec{s}_\circ$.

4.2 Simulating the Natural Transfer Process

In order to simulate the radiative transfer process, Monte Carlo simulations track individual photons as they scatter within the medium. By randomly sampling the three-dimensional space spanned by the medium and averaging the results, the Monte Carlo algorithm effectively solves the radiative transfer equation by means of stochastic integration. A simple outline of this process is given as follows:

1. Determine the piercing point of the incident photon packet (fired from the source) upon the surface of the cloud having a weight of unity.

2. Compute the free-path-length of the photon packet based on the cloud extinction characteristics.

3. Assess whether the next scattering point occurs within the medium (or simply transmitted out).

4. Calculate the coordinates of the scattering event (based on the current position, the trajectory of the photon packet, and the computed free-path-length).

5. Compute the scattering phase function value and transmission required for the photon to reach to the detector from this current position and at its current

trajectory; add this value to the signal and subtract it from the packet weight. (For the finite detector field of view case, only add this contribution if the scattering event is within the field of view).

6. Simulate the scattering event (pick a new zenith and azimuthal angle characterizing the new trajectory). Attenuate the packet weight by the single-scatter albedo (ω_o).

7. Recompute the trajectory of the photon based on the scattering angle results.

8. Repeat steps 2-6 until the photon has exited the medium, escaped the detector field of view, been completely extinguished by absorption, or has completed its maximum truncated scattering order imposed by the model.

9. Repeat steps 1-8 for as many photons as there are in a single salvo.

10. Repeat steps 1-9 for all the photon salvos of the run, generating a cumulative average of the results.

It should be noted that any real detector has a finite surface area over which photons may impinge to contribute to the detected signal. In addition, there exists a finite field of view associated with any detector. The solid angle associated with this field of view will subtend larger and larger areas as range from the detector increases. Real detectors, then, are sensors of spectral flux (units of $Wm^{-2}\mu m^{-1}$). Their signals may be converted to spectral intensity, or "radiance" (units of $Wm^{-2}\mu m^{-1}sr^{-1}$) by assuming that the intensity is uniform over the detector plate and normalizing the flux measurement by the detector's solid angle.

This problem is posed in a Cartesian coordinate system by which the position $\vec{x}_K$ and direction $\vec{s}_K$ of travel for the photon may be calculated at every point within the medium. Given a piercing point on the surface of the medium and a direction of travel, the Monte Carlo proceeds to follow the photon as it transmits/scatters

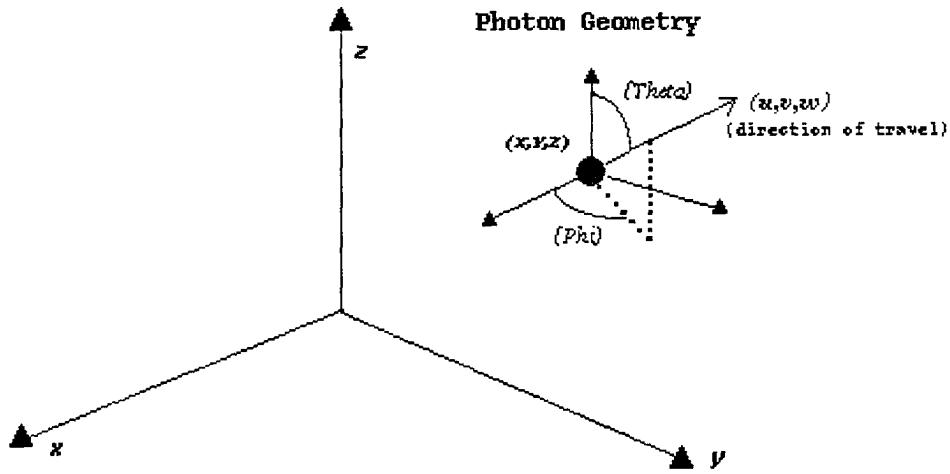

Figure 4.2: Cartesian-space geometry applicable to photon tracing within a scattering medium. Scattering geometry for the photon (ball) is expressed in terms of θ (*Theta*) and ϕ (*phi*) as shown.

through the medium. (See Figure 4.2). To do so, it first chooses an K^{th} order transmission "$\mathcal{T}_K$" (which translates to a geometric distance of travel between the current point and the next point of scatter) based on a uniformly-distributed random number drawn between 0 (no transmission) and 1 (complete transmission). To account for the dependence of this distance on the optical properties of the medium, this transmission is weighted by an exponential distribution according to Kunkel & Weinman (1976) and expressed here as:

$$\mathcal{T}_K = e^{-\int_0^{\mathcal{D}_K} \sigma_{ext}(s)ds} \tag{4.13}$$

where $\mathcal{D}_K$ is the geometric distance corresponding to a transmission $\mathcal{T}_K$ within the medium. Knowing the equation of the line defined by the photon's direction of travel, σ_{ext} may be integrated along this path to determine $\mathcal{D}_K$ numerically. Having determined $\mathcal{D}_K$ the location of the next scattering event in physical space is known, and two additional random numbers are drawn to determine the zenith (θ) and azimuth (ϕ) scattering angles corresponding to the next direction of travel.

While the azimuthal angle is chosen randomly between 0 and 2π (a consequence of the assumption of azimuthal symmetry in the behavior of the scattering particle). determination of the zenith angle is again weighted by a distribution representing the scattering phase function properties of the media. A uniformly-generated random number η is chosen and weighted by the scattering phase function to determine the appropriate scattering angle. The scattering phase function $\mathcal{P}$ is a probability density function for scattering. and is an intrinsic characteristic of any scattering medium. Solution of the corresponding scattering angle, Θ, may be obtained either analytically (providing that a solution exists) or by linear interpolation between tabulated values of η. While the former method is convenient for phase functions analytically representable, the majority of real-world scattering phase functions require the latter approach, and at high resolution in η.

It is usually more convenient in Monte Carlo applications to evaluate the line integral in equation 4.12 in terms of transmission. Because the transmission and extinction are related according to

$$\frac{d\mathcal{T}(\vec{x},\vec{x}')}{d\vec{x}'} = \sigma_{ext}(\vec{x}')\mathcal{T}(\vec{x},\vec{x}') \tag{4.14}$$

substitution into these line integrals results in the transformation from physical (geometric) space to transmission (optical) space

$$\int_{\vec{u}}^{\vec{x}} \mathcal{T}(\vec{x},\vec{x}')\sigma_{ext}(\vec{x}') \rightarrow \int_{\mathcal{T}(\vec{x},\vec{u})}^{x} \omega_{\circ}\, d\mathcal{T} \tag{4.15}$$

where $\omega_{\circ}$ is the "single-scatter albedo" which defines the fraction of the extinction due to scattering processes in the medium

$$\omega_{\circ} = \frac{\sigma_{sca}}{\sigma_{ext}} \tag{4.16}$$

Evaluation of the multidimensional integral in equation 4.12 may be readily transformed into integrals over the "unit hypercube" (one dimension in transmission

and the other two in scattering angle). As done in O'Brien (1992). the angular integrals

$$\mathcal{A} = \int_{\Omega} \mathcal{P}(\vec{x}, \vec{s}, \vec{s}')\, d\Omega(\vec{s}') \tag{4.17}$$

may be transformed using 4.5 and the variable substitutions

$$\zeta' = \frac{\phi'}{2\pi} \tag{4.18}$$

and

$$\eta' = \frac{1}{2} \int_0^{\Theta'} sin(\Theta) \mathcal{P}(\vec{x}, cos(\Theta))\, d\Theta \tag{4.19}$$

such that the resultant angular integrals take on the simplified form

$$\mathcal{A} = \int_0^1 d\zeta' \int_0^1 d\eta' \tag{4.20}$$

These transformations lend themselves directly to a discrete sampling of the hypercube space using uniformly-distributed random numbers drawn over the interval $[0, 1]$.

4.3 Forward Vs. Backward Monte Carlo

While the intuitive nature of Monte Carlo algorithm is appealing, the inefficiency associated with achieving appreciable returns remains a primary concern. While an actual source may instantaneously fire a great many photons, a computer model must keep track of a manageable number. When performing a measurement such as radiance (which requires that photons enter the detector at a specific direction of travel $\vec{s}$), the probability of any single photon both reaching the detector *and* doing so at the required direction is miniscule. Because Monte Carlo techniques rely on taking the average over a large sample space, the algorithm will fail for this kind of measurement if left to its own resources. We desire to pose the radiative transfer problem in both an intuitive and efficient context. Because of this constraint, various

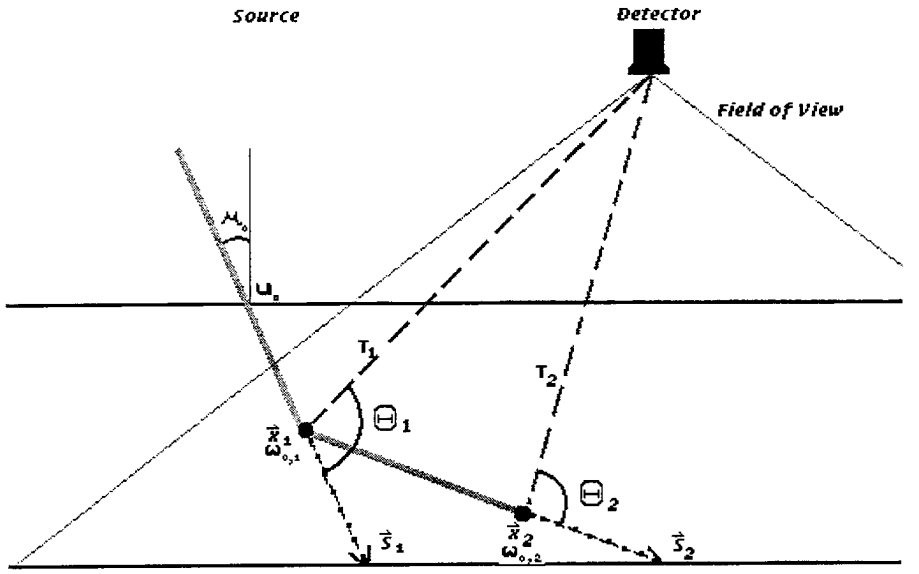

Figure 4.3: A cartoon depicting the first two scattering events as modeled in a Monte Carlo approach. See text for further detail in application.

amendments and techniques of "variance reduction" have evolved in an effort to render Monte Carlo runs more computationally efficient.

"Forward" Monte Carlo models, which trace the trajectory of a photon from the source to the detector, are generally used for calculation of hemispheric fluxes. Figure 4.3 illustrates how photons contribute to the measure intensity in a probabilistic weighting scheme (shown for the first two orders of scattering) using a technique which traces to the detector at each scattering event (Tsay *et al*, 1992). Referring to the figure, the first and second order contributions to the measured intensity for this case are given by

$$I_1 = \mathcal{T}(\vec{u}_o, \vec{x}_1)\frac{\mathcal{P}(\Theta_1)}{4\pi}F_{src}\omega_{o,1}\mathcal{T}(\vec{x}_1, Detector) \tag{4.21}$$

and

$$I_2 = \mathcal{T}(\vec{u}_o, \vec{x}_1)\omega_{o,1}\mathcal{T}(\vec{x}_1, \vec{x}_2)\omega_{o,2}\frac{\mathcal{P}(\Theta_2)}{4\pi}F_{src}\mathcal{T}(\vec{x}_2, Detector) \tag{4.22}$$

While computation of radiance using a forward Monte Carlo is highly inefficient, the adjoint problem is well posed. That is, observing that if a photon were to depart the *detector* at precisely the same angle at which it entered, then it would exactly retrace its path back to the source (Ambirajan and Look, 1996). Termed "backward" Monte Carlo, this method works well for computing radiance, since the model has complete control over the incident direction of detected photons and is not at the mercy of chance events. In an real experiment, a detector of solar radiance would receive countless photons from a source which, for all practical purposes, emits an infinite number of photons. Therefore there is no fundamental violation in backward Monte Carlo's premise of firing as many photons as is computationally efficient in a single direction of interest in order to achieve a stable radiance solution. As in the forward algorithm, the contributions for each order of scatter are decomposed, averaged and combined to yield the intensity in $(Wm^{-2}str^{-1}\mu m^{-1})$.

4.4 The Utility of Monte Carlo Products to This Study

The Monte Carlo solution to the radiative transfer equation not only provides accurate radiance and flux results, but also gives information about photon path distributions. A photon path distribution offers a statistical view of the geometric travel-distance of a "typical" K^{th}-order scattered photon. Such distributions are useful for making inferences about the optical properties of the cloud because they are a direct function of it. Book-keeping of scattering event occurrences as a function of cloud penetration depth are useful for gauging the effects of multiple scattering, and inferring properties of the cloud's scattering phase function. Of course, these are quantities which are specified *a priori* in the Monte Carlo cloud input parameters, and are unknown quantities in real-world observations. However, if the observations can provide information about the nature of the scattering (the development

of a forward model), inversion theory immediately suggests a means of backing out the "input parameters" necessary to create these observed effects. Given an adequate representation of the physical process, the problem of cloud property retrieval from observations of active sensor pulse stretching behaviors is exactly analogous to space-borne passive instrument retrievals currently in operation.

The by-products spawned by the tedious nature of the Monte Carlo method were exploited in this research for the purpose of understanding pulse extension artifacts in the space-borne lidar problem. These data include:

- Contribution to signal as a function of
  - Scattering order.
  - Geometric depth within medium.
  - Radial distance from beam center.
- Photon path length distributions.
- Pulse extension distributions

4.5 The Code Used Herein

For this project, a backward Monte Carlo code originally written by Denis O'Brien was obtained and modified to accommodate the lidar geometry. This code was originally applicable to the classic solar problem using an accelerated "quasi" Monte Carlo integration of the radiative transfer equation. The use of the Halton sequence instead of purely random quadrature nodes samples the integration space more uniformly and accelerates convergence. Specifically, the error estimation is reduced from $N^{-\frac{1}{2}}$ to $N^{-1}(log\ N)^d$, where N is the number of photons fired and d is the dimension of the integration. Chapter 5 describes the modifications and assumptions made to apply the code to the problem at hand.

As a verification its correct performance in the solar application, the original O'Brien code was compared to test cases run with a doubling and adding radiative transfer model. The comparisons for three conservative scattering ($\omega_o = 1.0$) cases for isotropic, single and double Henyey-Greenstein phase functions are shown in Figure 4.4 to be in good agreement, as expected. The deviation at high observation angles is a problem associated with the Legendre expansion of the scattering phase function necessary to doubling and adding representation (due to a relative dearth of quadrature points in this angular regime); an issue that is not applicable to Monte Carlo. The ability to incorporate scattering phase functions possessing high degrees of anisotropy at relatively low computational cost is another advantage of Monte Carlo over analytic methods which must explicitly represent the radiance field in an expanded form.

4.6 Summary

Monte Carlo is a viable method for obtaining a multiple scattering solution to the radiative transfer equation by means of a stochastic process. It is reputed as an accurate (albeit computationally expensive) means of computing radiative transfer products such as radiance fields and transmitted/reflected fluxes. Because it operates in a three dimensional paradigm, it immediately lends itself to applications in 3D cloud effects, and is generally more efficient than explicit models when few parameters are required. We can take advantage of its "brute-force" simulation of photon transfer by keeping track of contributions of the signal as a function of scattering order and depth within the medium. The ability to record contributions to the signal as a function of geometric path traveled makes Monte Carlo the algorithm of choice for direct modeling of the lidar pulse stretching effects.

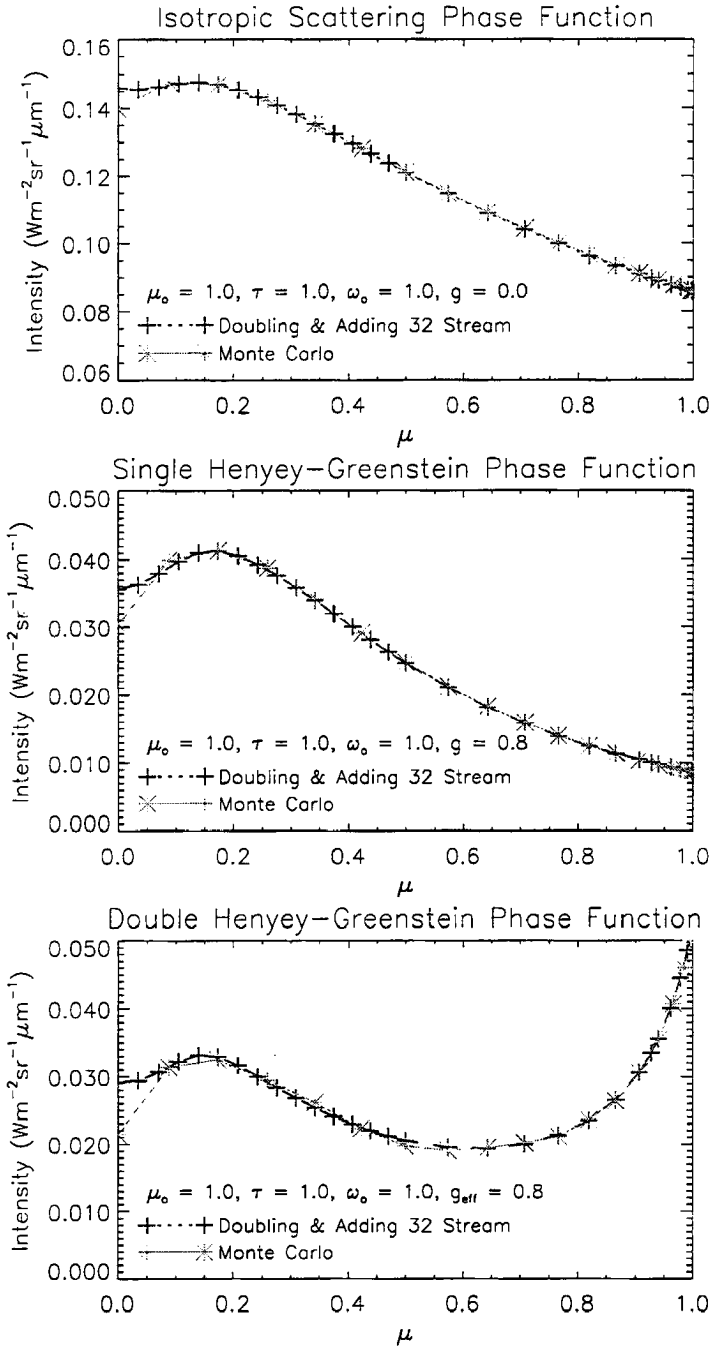

Figure 4.4: Comparison of Backward Monte Carlo to Doubling & Adding radiative transfer model results for three different scattering phase functions and Plane Parallel cloud

Chapter 5

LIDAR IN A MONTE CARLO CONTEXT

The goal of this Chapter was to outline and justify the modifications necessary in order to recast the "traditional" (infinite source) Monte Carlo problem described in Chapter 4 into a a model suitable to representing the physical problem of a lidar instrument on a Space Shuttle operational platform. While the fundamental operation of Monte Carlo remains the same (as for the procedure for tracing photons through the medium), the geometry of the problem changes with the specification of a finite source (the laser beam) as opposed to an infinite source (the sun). The implications of a finite source confuses the the traditional correlations between "forward" and "backward" Monte Carlo approaches, and the appropriate implementation for this problem is discussed in this context.

5.1 Backward/Forward Monte Carlo Realizations

The computational efficiency of applying a backward Monte Carlo approach to the lidar (finite beam) problem came into question early on. The fundamental difference between the solar and lidar problem resides in the fact that a laser beam is, by definition, a finite source. Figure 5.1 illustrates the geometric differences between the finite and infinite source cases. Considering the solar case for a plane parallel media, the incident beam direction is taken to be the same at all points upon the

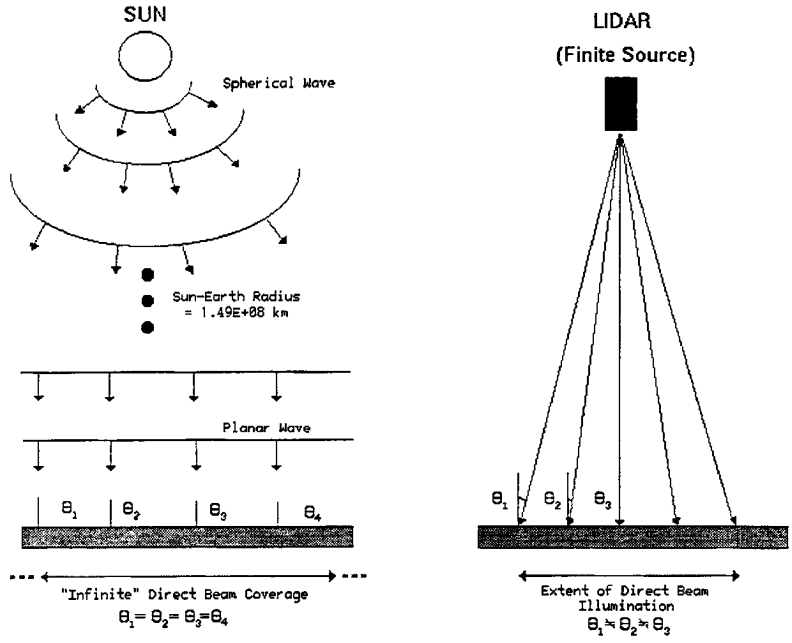

Figure 5.1: The differences between the infinite (solar) and finite (lidar) source problems.

surface of the scattering medium, whereas a lidar beam is limited in coverage to a localized, elliptical cross-sectional area of illumination. While the laser beam is highly collimated, it still has a non-zero beam divergence (somewhat larger in design for the space-based lidar for ground eye-safety concerns), meaning that even in this localized area of illumination the incident beam angle θ_{src} is variant. Furthermore, the distribution of photons in a lidar beam follows a Gaussian probability density function; with a higher photon flux at the center of the beam and decreasing radially. This is unlike solar insolation which is approximated to very high order as a constant value over the entire incident surface of the medium.

5.1.1 Geometry of the "Finite Source" Problem

The physical differences that exist between the finite and infinite source problems affect the modeling of photon contributions in Monte Carlo codes in the following way. In backward Monte Carlo applications, the photons (or "packets of photons")

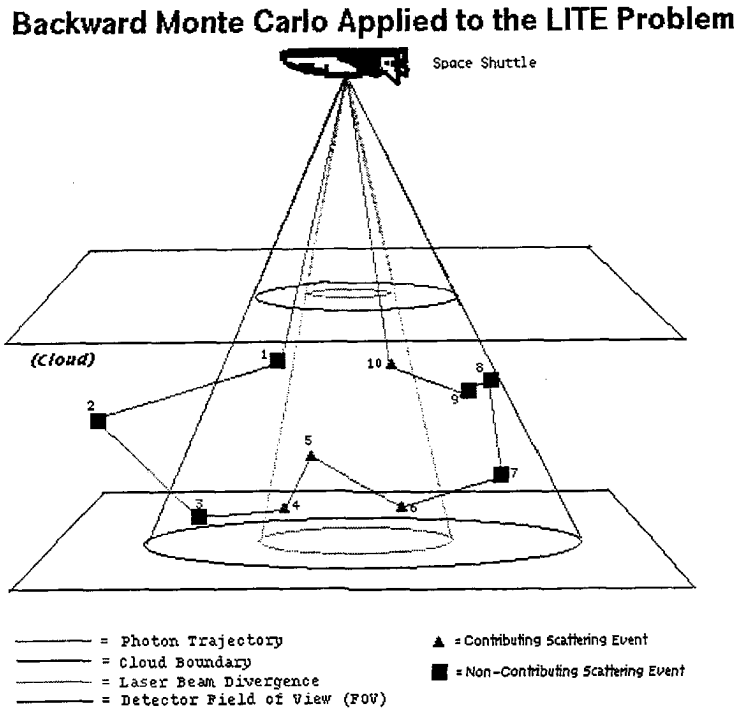

Figure 5.2: Tracing the photon path through a cloud medium for several orders of scatter. Note that for the backward Monte Carlo problem only scattering orders 4,5,6, and 10 may contribute to the intensity. (See text for discussion)

are traced back to the source at each scattering event along their trajectory within the medium in order to obtain an estimate of the contribution to the intensity at that scattering order. For the solar (infinite source) problem, photons are traceable back to their source (the sun) at *all* points within the scattering medium. For a finite beam of the lidar, only photons within the laser beam divergence may be physically traceable straight back to the source. This imposes a rather stringent constraint on the backward Monte Carlo problem as traditionally posed, since photon scattering events may only be counted as a K^{th}-order realization if they occurred within the geometric sub-cone defined by the laser beam divergence.

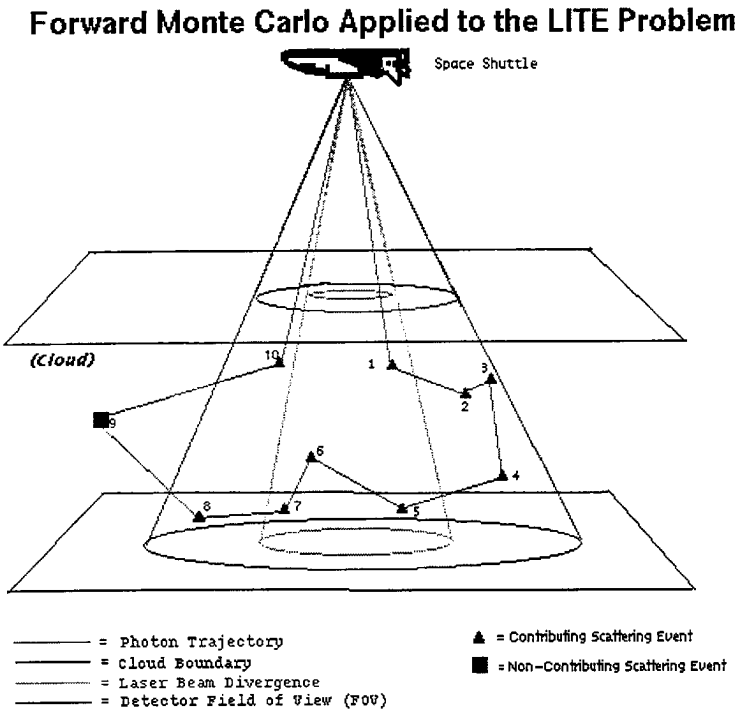

Figure 5.3: Tracing the photon path through a cloud medium for several orders of scatter. Note that for the forward Monte Carlo problem all scattering orders except 9 contribute to the intensity. (See text for discussion)

5.1.2 Detector Field of View Considerations

Further complications arise when considering the possible variation of the detector field in the backward Monte Carlo approach. As was mentioned in Chapter 2 and illustrated in Figures 4.3 , 5.2, and 5.3, the detector assembly on the lidar has a characteristic field-of-view whose spot size diverges with radial distance from the instrument. According to the geometry of the problem shown in (Figure 5.2), a photon fired into the medium may contribute at *some* scattering orders (those which occur within the beam divergence) but not at others. In the figure, contributing scattering events are denoted by triangular nodes and non-contributing events are given by square nodes. It is immediately apparent that, for any given photon realization, not all scattering events will be able to contribute physically to the modelled signal

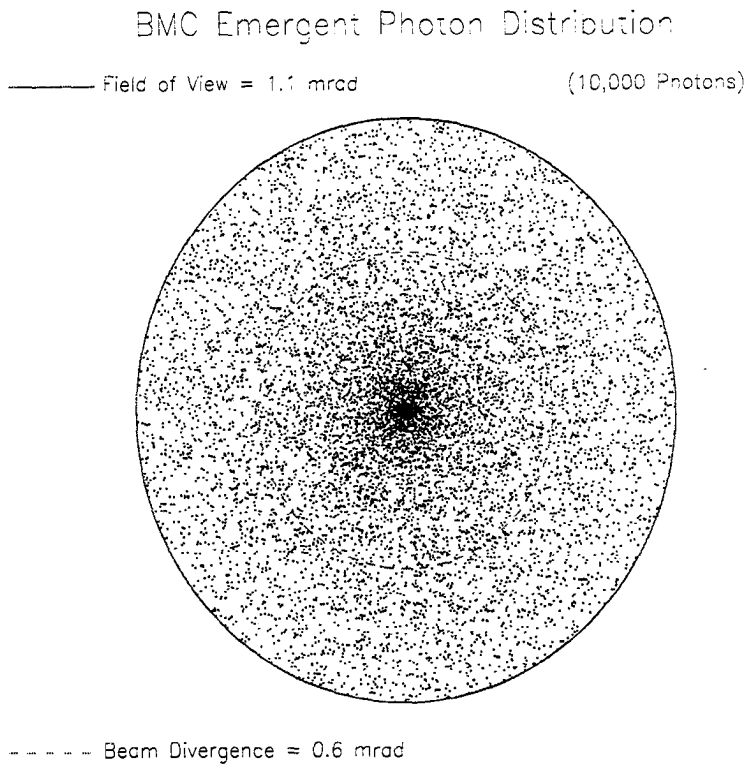

Figure 5.4: Photon "piercing points" in the backward Monte Carlo fired uniformly over $cos(FOV_{det}/2)$.

return. For this reason, the contributions associated with the scattering events must be recorded for all scattering orders regardless of contribution , and a delta function is implemented to police the actual contributions accordingly (allowing only scattering events within the beam divergence to contribute their contributions to the stochastic solution).

For the nadir-viewing lidar instrument in the physical problem, it is reasonable to expect a greater harvest of detectable photons in the medium when the detector field of view is increased. This is illustrated in Figure 5.5, which isolates the contributions to the total signal as a function of scattering order, penetration depth in the cloud, and detector FOV. Comparing the 3.5mrad and 28.0mrad detector FOV

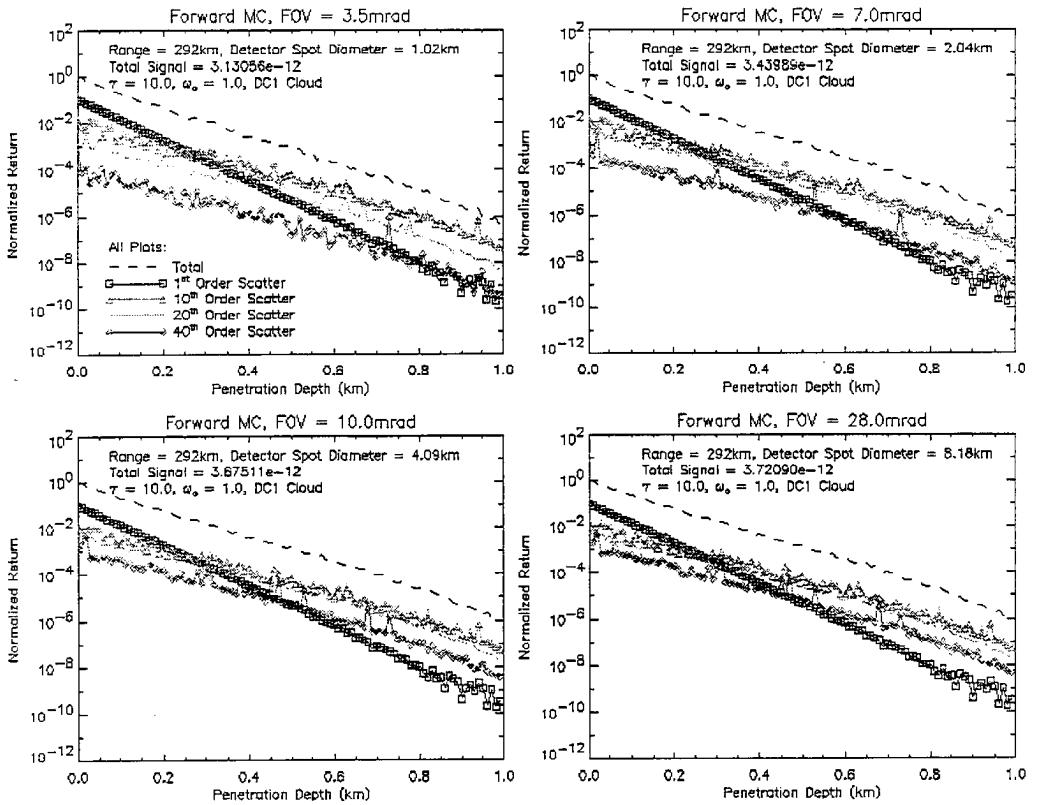

Figure 5.5: Contributions to return as a function of photon scattering order and detector field of view (FOV)

cases, the relative increase in the signal due to contributions from higher order scattering events is evident. These higher order scattering contributions are expected to yield higher amplitudes of lidar pulse stretching, as they represent photon geometric path lengths far in excess of single scattering distances.

In a backward Monte Carlo, photons are traced "backwards" from the detector, into the medium, and finally to the source. (See Figure 5.2) Because returning photons at the detector must have physically emerged from the medium somewhere within the detector's field of view (with appropriate direction), it is requisite of the backward problem to fire photons somewhere within this field of view. Without *a priori* constraints imposed on the scattering behavior of the medium, photons must be fired from the detector into the detector field of view in a random uniform

distribution. When the detector field of view is increased, however, the pitfall to this implementation becomes immediately apparent.

Obviously, there is no "homing mechanism" in a photon to guide it back towards the beam divergence (which determines whether or not it will be counted towards the signal). For the traditional backward Monte Carlo procedure this is not a problem, as the photon are traceable to the source at all locations within the scattering medium (the solar zenith angle is assumed constant owing to the vanishingly small $d\mu_0$ associated with the distant solar source). In the case of a finite source, problems are immediately encountered with photon sampling. For an incremental increase of the detector field of view (and holding the laser beam divergence fixed), the probability of photons reaching the relatively narrow beam divergence cone will decrease, since more and more photons are beginning their random trajectories further and further away from the central beam. Furthermore, specification of a distribution of piercing points (where the photon being fired from the detector first "pierces" the medium) can not be made without forcing *a priori* constraints on the physical nature of the scattering process. Lastly, and perhaps most importantly from the geometric considerations of lidar pulse stretching, the distribution of scattering order events in the physical problem are highly constrained; all first order events by definition must occur within the cone formed by the laser beam divergence. Combining this with the case where the detector field-of-view exceeds that of the laser beam divergence, the problem becomes substantially ill-conditioned to the backward Monte Carlo approach.

In contrast, Figure 5.3 depicts the problem in the forward Monte Carlo context. In this case, photons are fired from the laser beam source and traced back to the detector, as in the physical problem. By starting with all the photons within the beam divergence, the problem is well-posed from the standpoint of sampling–allowing for the increase of signal return with increasing field of view as is expected

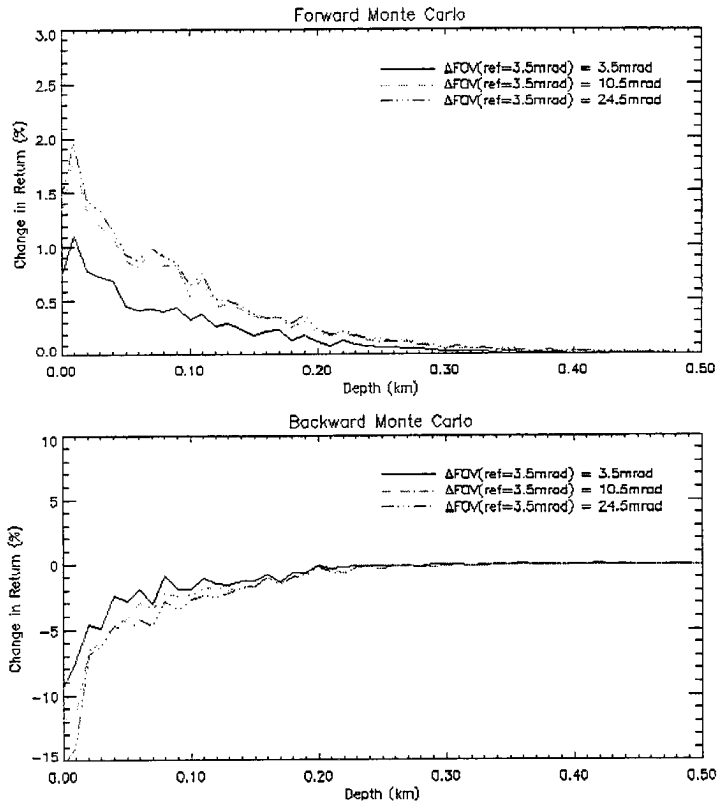

Figure 5.6: Illustration of the under-sampling issue encountered when applying backward Monte Carlo to the finite-beam problem.

in real applications. Figure 5.6 shows the change in return as a function of detector field of view and depth in the medium. The medium was conservatively scattering, having optical depth of $\tau = 10$, and a nadir-viewing lidar at an altitude of 292 kilometers above cloud-top. In the forward modeling of photons, the signal return increases with increasing detector field of view. These changes are most significant at low FOV, and level off for larger FOV as fewer radially-scattered photons contribute (a function of the scattering properties of the medium and the optical depth). The necessary truncation of scattering order (computational limitations of the model) may also be contributing to the leveling-off of signal return. Because real cloud scattering phase functions have the characteristic of strong forward scattering lobes, it is probably reasonable to assume that significant radial contributions will in fact decay as shown. The lower plot in Figure 5.6 indicates that signal return

actually decreases significantly with increasing detector field of view. This of course is counter-intuitive, and is a direct result of the ill-posed nature of the traditional backward Monte Carlo algorithm in the lidar problem.

5.2 The Lidar Revisions

Detection of photons impinging upon a surface of finite area and a non-singular direction casts the problem at hand into one not of radiance, but of flux. A number of modifications were made to the standard Monte Carlo model to address the questions posed in this research in regards to the effects of cloud optical properties on observed pulse extensions. The following section is a brief synopsis of the changes and/or adjustments made for this purpose.

5.2.1 Recasting the Problem

Forward Monte Carlo algorithms are generally used to compute accurate level-fluxes, while backward Monte Carlo tackle the problem of radiance. As shown above, the traditional backward Monte Carlo approach would not suffice for modeling lidar pulse extensions due to physical sampling issues. Furthermore, a radiance result does not account for the detector field-of-view dependency (radiance are calculated for a fixed viewing direction, whereas a field-of-view encompasses an infinite number of viewing directions). On the other hand, the finite surface area of the detector (located at satellite orbit ranges) meant that a level-flux calculation (the product of most forward Monte Carlo algorithms) was also computationally inefficient.

What was needed was a marriage of the two techniques: the computational efficiency of the backward Monte Carlo and the physical intuitiveness of the forward application. To this end, the forward algorithm was adopted with the amendment of a weighted forced-scatter to the detector at each scattering event within the medium (as is done in backward Monte Carlo to the source). Provided that this weighting

(by the scattering phase function) is done in an identical manner to that of the backward Monte Carlo implementation, there is no violation to the algorithm. It may be thought of in terms of a variance reduction technique, where each photon is now considered as a packet of many photons and the packet is assigned a weight of unity. At each scattering event a fraction of this packet is forced to scatter back to the detector with a probability defined by the scattering phase function.

5.2.2 The Modeling of Photon Random Walks

The "random walk" of a photon through the scattering medium is governed by the scattering phase function as described in Chapter 4. A medium having a strong forward and backward ($\Theta = 0$ and 180, respectively) scattering peaks will tend to either transmit photons directly through the medium or reflect them directly back, while inhibiting the propagation with a component normal to the beam source. In contrast, more isotropic scattering phase functions (with less preferential scattering direction tendencies) will more readily scatter photons into radial directions. The nature of these trajectories affects the total travel distance of photons returning to the detector, and ties directly into the problem of pulse extensions. For these reasons, it is imperative to model the physical photon trajectories within the medium as accurately as possible.

The quasi-random Hammersley-Halton sequence was therefore replaced by a truly random number generator. The Hammersley-Halton (HH) series improves the convergence of the Monte Carlo by more evenly sampling the space spanned by the 3-dimension "hypercube" (comprised of transmission and scattering direction), but the sequence itself should not be applied to the problem of photon path analysis because of the very "quasi-ness" of its random sequence. In some instances, a photon's physical trajectory using the HH sequence will shift systematically towards increasingly forward scattering angles with increasing scattering order, while in reality this

should not be the case (never in the ensemble sense does there exist memory associated with scattering processes). Likewise, adjacent transmission events exhibit a high correlation. When interpreting the scattering behavior of photons from a truly physical standpoint, such correlations could not be accepted.

In the current application, the photon paths traveled are considered as *real* itineraries in the medium. That is, they are modeled according to the actual chain of events taking place in the physical problem–photons are diverging from the beam center and propagating through the scattering medium according to the medium's inherent optical properties. The true-to-life propagation of these photons through this scattering regime is the cornerstone to the correct modeling of lidar pulse extension effects. Because the Halton sequence denies the photon of "certain inalienable rights" of scattering behavior, it cannot be used in this application, despite the fact that it does offer a superior sampling of the medium and thereby an accelerated convergence to the correct radiance results.

5.2.3 Incorporation of Anisotropic Scattering Phase Functions

In an effort to model more realistic cloud phase functions, the Monte Carlo code was modified to include the double Henyey-Greenstein (DHG) phase function (featuring a back-scatter peak), the Deirmendjian (1969) C1 phase (DC1) function (a more realistic cloud phase function computed from Lorentz-Mie theory), and idealized ice crystal phase functions from the ray-tracing work of Takano & Liou (1995) (described in more detail in Chapter 6). While the evaluation of scattering angles for the single HG phase function were computed analytically, the procedure to extend to double HG involved the solution of a fourth-order polynomial in $cos(\Theta)$ (where Θ = scattering angle) and was altogether unobtainable for the DC1 cloud phase function to within reasonable expansion order.

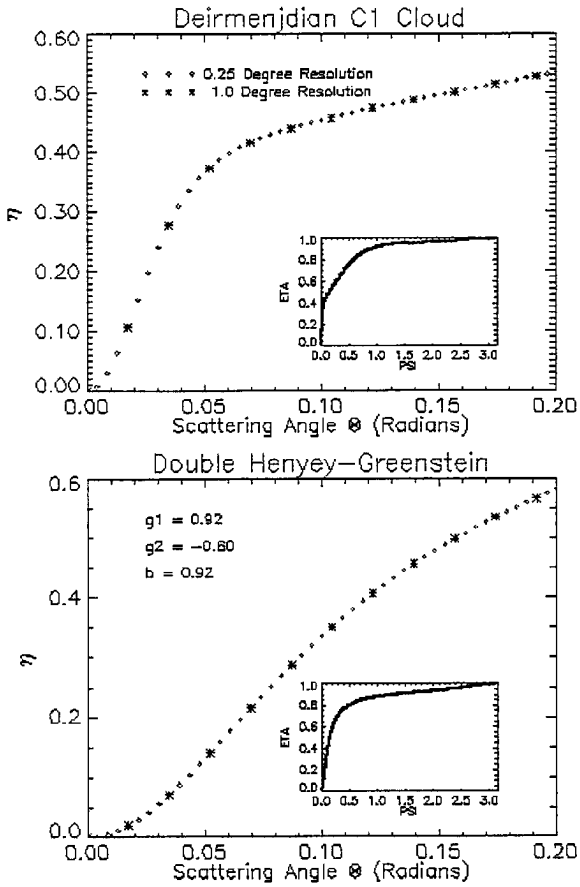

Figure 5.7: Basis for the (η, ψ) Scattering Phase Function Look-Up Tables

Initially, two approaches were taken to address the issue of dealing with complex scattering phase functions. In the first approach, a quasi-analytical solution was obtained by implementing a fit of the (η, ψ) relationship. The strong forward scattering peak in the phase functions of interest resulted in a highly sensitive relationship at small ψ and weak sensitivity at larger ψ. This necessitated a three-regime exponential fit to adequately characterize the response. Considering the effort required to generate essentially by-hand such a solution each time a new phase function was implemented, an alternative and more general method was desired.

To this end, a (η, ψ) lookup-table approach was implemented, with a simple linear interpolation implemented between points to obtain the appropriate scattering angle as a function of a passed cumulative probability value, η. To generate

the tabulated phase function for the DC1 phase function, the C1 modified gamma distribution

$$\begin{aligned} n(r) &= a\, r^{\alpha}\, exp(-b\, r^{\gamma}) \qquad (5.1) \\ 0 &\leq r < \infty \\ a &= 2.3730 \\ b &= 1.50 \\ \alpha &= 6.0 \\ \gamma &= 1.0 \end{aligned}$$

was applied to Lorentz-Mie scattering theory and output at 0.25 degree angular resolution. This resolution was necessary to ensure that the phase function integrated to unity with minimal discontinuity at $\Theta = \pi$. Computation of the scattering angle back to the source remained an analytical computation for the double Henyey-Greenstein phase functions, while the table-lookup method was used here for the non-analytical cases. As mentioned previously, the random number η passed to this routine represented the integration of the phase function. It is mathematically expressed as

$$\eta = \frac{1}{2}\int_0^{\Theta} \mathcal{P}(cos(\Theta'))sin(\Theta')d\Theta' \qquad (5.2)$$

where, for Double Henyey-Greenstein:

$$\begin{aligned} \mathcal{P}(x) &= bP(g_1, cos(x)) + (1-b)P(g_2, cos(x)) \\ (0 < & \quad b \quad < 1) \end{aligned} \qquad (5.3)$$

and

$$P(g_i) = \frac{1-g_i^2}{(1+g_i^2-2g_i cos(\Theta))^{3/2}} \quad (i = 1, 2) \qquad (5.4)$$

Note that double Henyey-Greenstein reduces to single Henyey-Greenstein by assigning the weight b to unity. Double Henyey-Greenstein parameters were calculated by

specifying an "effective" asymmetry parameter, g_{eff}, and computing the according to

$$\begin{aligned} g_1 &= g_{eff} + 0.05 \\ g_2 &= -0.60 \\ b &= \frac{g_{eff} - g_2}{g_1 - g2} \end{aligned} \tag{5.5}$$

This parameterization follows those of Duda (1994) and Stackhouse (1995), and was chosen because it gave a reasonable representation of Mie scattering phase functions, particularly in the backscattering angular region. No closed analytical form is available for most real-world phase functions, and the complicated behaviors of the Deirmendjian C1 and Takano & Liou (ray-tracing) phase functions are no exception. For such cases, a tabulated data set as described above was used with a trapezoidal integration rule to solve Equation 5.2. Using the tabulated approach, virtually any scattering phase function may be represented provided sufficient angular resolution to capture the details in the highly variable regimes.

5.3 Verification With Theory

An essential benchmark before applying the lidar-modified algorithm was to verify its performance with theory. Comparison of the single scattered lidar return with an analytic solution was chosen for this purpose for several reasons.

- The Monte Carlo code readily outputs 1^{st}-order scatter contributions to the return signal as part of its multiple scattering series results.
- For optically thin clouds, single scattering is the dominant contributor to the return.
- A concise analytic solution to single scattered reflected intensity exists in the literature (Liou, 1980)

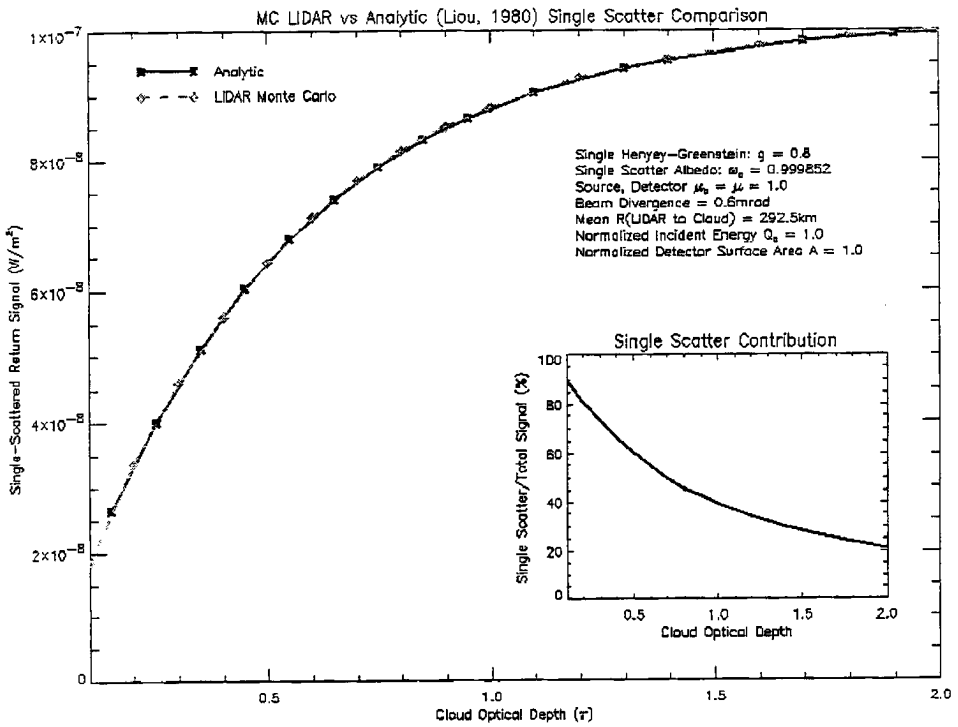

Figure 5.8: Comparison of the lidar-revised Monte Carlo algorithm to theory (Liou, 1980) for single scatter returns

The development of the analytic single scatter solution is trivial; following immediately from the azimuthally-independent radiative transfer equation without the multiple scattering term with a rescaling of the source term

$$\mu \frac{dI(\tau,\mu)}{d\tau} = I(\tau,\mu) - \frac{\omega_\circ}{4\pi} F'_\circ \mathcal{P}(\mu,\mu_\circ) e^{-\frac{\tau}{\mu_\circ}} \tag{5.6}$$

where

$$F'_\circ = \frac{F_\circ}{\Omega_{src}} \tag{5.7}$$

Invoking the (reasonable) boundary conditions that there exists no diffuse downward and upward radiation at the top and base, respectively, of the finite atmosphere

$$\begin{aligned} I(\tau = 0, -\mu) &= 0.0 \\ I(\tau = \tau^*, +\mu) &= 0.0 \end{aligned} \tag{5.8}$$

then 5.6 is solved immediately for the reflected intensity

$$I(\tau^*, \mu) = F'_\circ \frac{\mathcal{P}_{back}}{4\pi} \frac{\omega_\circ}{m\mu}(1.0 - e^{-m\tau^*}) \tag{5.9}$$

where $m = (\frac{1}{\mu} + \frac{1}{\mu_\circ})$ is the "air mass" factor and $\mathcal{P}_{back}$ is the scattering phase function evaluated at the backscattering peak, $cos(\Theta) = -1.0$.

Figure 5.8 shows the output of the lidar-modified Monte Carlo against the analytic single scattering results as a function of cloud optical depth. The fact that Monte Carlo outputs the intensity due to single scattering events as an independent quantity enables this direct comparison.

5.4 The Modeling of Pulse Extensions

In the context of Monte Carlo modeling, the procedure for determining of the actual pulse extensions amounted to a straightforward exercise in book-keeping. Several data fields encompassing relevant aspects of photon trajectory histories were recorded for a variety of cloud optical property scenarios. These included

- Round trip (source to detector) photon path distances as a function scattering order.
- In-cloud photon path length distributions as a function of scattering order.
- Relative contributions to return signal as a function of cloud penetration depth and scattering order.
- Contribution to return signal as a function of radial distance from laser beam center and scattering order.
- Varying detector field-of-view studies.

5.4.1 Round-Trip Travel Distances

Round-trip distances were binned for each contributing photon scattering order, along with their associated contribution to the signal, as follows:

$$D_{rt}(K) = D_{dp} + D_{ps}(K) + D_{ss}(K) \tag{5.10}$$

where:

D_{dp} = Distance from source to piercing point at top of medium.

D_{ps} = Distance from piercing point to scattering event "K" as traveled along the photon's random walk.

D_{ss} = Distance from scattering event "K" back to detector.

These results were used in the computed maximum below-cloud-base pulse extensions, and formed the primary data set for use in cloud optical property retrievals.

5.4.2 Photon Path Length Distributions

Photon path length distributions (PLD's) characterize the probability that a photon undergoing K scattering events will have traveled a distance λ within the scattering medium

$$< \lambda_K >= \sum_{i=1}^{K} \mathcal{D}_i \tag{5.11}$$

where $\mathcal{D}$ is the geometric distance traveled by the photon between scattering events $i-1$ and i (where scattering event "0" is the piercing point of the photon upon the medium boundary). Knowledge of the PLD gives an idea of which scattering orders are associated (in a statistical sense) with pulse extensions. Combining this information with the relative contribution to the signal from these scattering orders determines to what extent these features will actually be observed.

5.4.3 Cloud Penetration Depth Contributions

It is important to identify the threshold where first-order scattering events no longer dominate the return signal. The deeper a photon penetrates within an optically thick layer, the more likely it is to have undergone multiple scattering events. While it has been suggested that multiple scattering aids in an enhanced probing of the cloud medium, it must also be recognized that these effects muddy the waters of assigning accurate range to these signal returns. It is entirely possible that, for an optically thick cloud, the return signal originated from many orders of scatter which all occurred near the *surface* of the cloud. This in light of the fact that its contribution was ranged at a significant depth within the cloud (owing to the single-scattering ranging algorithm). Keeping track of from where in the cloud the returns are originating as a function of scattering order allows for a proper assessment of this problem.

5.4.4 Radial Contributions

Because pulse extensions are nothing more than a compilation of photons whose accumulated travel distances exceeded by varying degree the round-trip distance from source $\rightarrow$ cloud base $\rightarrow$ detector along the direct beam, it is useful to understand the radial (normal to the direct beam) distances of contributions for different cloud optical properties. Most real-world scattering phase functions are characterized by strong forward-scattering peaks and a small backscattering lobe. These phase functions have a strong dependency on the cloud particle size distribution, phase (ice/water) and habit. The increase of radial contributions to the return should correlate strongly with the increase of pulse extensions.

5.4.5 Detector Field of View

The information obtained from increasing the detector field of view is an operational way of observing the radial contributions to the return signal. During selected pe-

Chapter 6

MULTIPLE SCATTERING BEHAVIORS

Before engaging in any meaningful discussion of the lidar pulse stretching features in terms of the (non-trivial) physical scattering processes occurring within cloud media, it is first necessary to lay out rigorously the groundwork for the behavior of multiple-scattered photons and their implications to in-cloud travel times. It should be clear that even for the case of intense multiple scattering, all returns must still originate from somewhere within the scattering media. While it has been observed that multiple scattering results in "deeper returns", extreme caution must be exercised so as not to interpret these signals as necessarily originating from the depths that they advertise. This is a significant caveat introduced by multiple scattering and, as it lends itself so easily to misinterpretation, and is a point that shall be harped upon *ad nauseum*. This chapter explores the physical scattering processes as modeled with the lidar-adapted Monte Carlo algorithm described in Chapters 4 and 5.

6.1 Defining the Model Parameters

To isolate the pulse stretching sensitivities to cloud optical properties with minimal ambiguity, this research focused on a confining set of instrument parameters.

Wavelength	532nm
Beam Divergence	0.6mrad
Field of View	(Variable)
Instrument Altitude	293km (AGL)

Table 6.1: Monte Carlo Instrument Geometry Parameters

Inspired in large part by the LITE mission and its findings, the hardware specifications for the hypothetical instrument were naturally biased toward the values of the NASA-Langley instrument flown during STS-64. The instrument modeled for this work was a monochromatic, variable FOV lidar operating at a wavelength of 532nm (such that the ray-tracing phase functions of Takano & Liou would apply without modification). It should be noted that the cloud optical parameters investigated here are infact strong functions of wavelength. While this investigation of lidar pulse stretching was based on single-wavelength information, the extension of the study to an array of different operation wavelengths stands as an inviting direction for future modeling efforts.

6.1.1 Instrument Specifications

The Monte-Carlo lidar model simulated the nadir-viewing lidar instrument at Space Shuttle orbit ranges, with similar specifications to the instrument employed during LITE (See table 6.1). During the daytime orbits of the mission, the lidar operated with a detector FOV of 1.1mrad. This corresponded to a spot diameter of 177 meters and a field-of-view diameter of 324.5 meters for a cloud layer top at 1km. (See Figure 5.4). During night time operation, the detector FOV was expanded to 3.5mrad, producing a FOV diameter of nearly 1km. While, in the absence of solar noise, this served to strengthen the return signal, it also added more multiply-scattered contributions to the return signal. For simplicity, all simulations were run for nighttime cases, with no solar contamination (besides secondary lunar reflections) assumed.

riods of the LITE mission orbits, four apertures were interposed sequentially: a 3.5mrad open aperture, an annulus allowing only signal returns between the angles of 1.1 and 3.5mrad, a 1.1mrad aperture and a fully-occulting aperture (Platt and Winker, 1996). This allowed for some qualitative comparisons of returns from varying multiple scatter, but due to the two-second dwell time in each aperture setting and the rapid ground-speed of the orbiting shuttle ($\approx$ 7.4km/s), different portions of cloud were being sampled in each case. Because the degree of radial scattering is a function of both the scattering phase function and cloud optical depth, the observed variation in pulse extension magnitudes might serve as a means of backing out this optical property information. For a cloud of given optical depth, care must be taken in the Monte Carlo simulations to adequately account for higher-order scattering contributions as the detector field of view increases.

As the number of photon trajectories simulated approaches infinity , the relative contributions to the signal associated with increasing pulse extension are observed to drop off along with the frequency of occurrence. However, an artifact of the Monte Carlo sampling method occasionally appears in the returns whenever a photon's trajectory results in a *forward scatter* when tracing to back to the source. For strongly forward-peaked phase functions, the instantaneous value of the the phase function can be substantial, leading to a very large contribution associated with this event as described by Platt (1981). For a large number of photons, such "spikes" in the contributions dither to a smoother, decaying response with increasing distance along the pulse extension return. Further smoothing may be accomplished by launching several "salvos" comprised of many photon packets and then averaging the results.

5.5 Summary

The traditional Monte Carlo problem was recast to the special case of a finite-source geometry at orbit altitudes. The advantages and limitations of traditional backward

and forward applications of Monte Carlo were discussed in terms of the physical and computational requirements associated with modeling the pulse extension phenomenon. A compromise between the two procedures was reached which offered both physical clarity and computational efficiency. The modifications included. a forward estimate applied as a variance reduction technique. the exclusion of the Halton sequence in favor of a uniform random number generator for the selection of transmission and scattering angle terms in favor of a uniform random number generator. the inclusion of a phase-function integration package to construct the (η, φ) scattering phase function lookup tables, and the addition of an extensive array of book-keeping procedures dedicated to isolating photon path histories relevant to characterization of lidar pulse stretching. Measurements of the multiply-scattered contributions as a function of cloud penetration depth, radial distance from the direct beam, and increasing detector FOV were identified as proxies to the lidar pulse stretching effects. Examination of these measurements are the subject of Chapter 6.

Because this discussion included an attempt to relate cloud properties to physical pulse extension distances, it was important to understand exactly what the physical detector could and could not see. The returned signal is a function both of the instrument properties and the characteristics of the scattering medium, and is expressible in terms of the "lidar equation" (for single-scatter) as

$$P_{lid}(R) = \frac{C_{lid}}{R^2} \frac{\beta(R)}{4\pi} exp\left(-2\int_0^R \sigma_{ext}(R')\, dR'\right) \qquad (6.1)$$

This equation describes the returned power ($P_{lid}(R)$) originating from an illuminated pulse volume located at a range (R) from the instrument. The lidar system constant, (C_{lid}), contains instrument-dependent factors such as transmission power and telescope parameters, and $\beta(R)$ is the lidar backscatter cross section (a wavelength-dependent quantity representing the combined scattering cross-sectional areas for the scatterer species within the pulse volume). The exponential term describes the two-way (to and from the pulse volume) attenuation of the signal, with σ_{ext} being the volume extinction coefficient (another wavelength-dependent quantity) as described earlier.

Platt (1973) addressed the modification of 6.1 to account for the effects of multiple scattering. Introducing multiple scattering to the system effectively reduces the extinction coefficient (enhancing the number of returning photons which would otherwise have been lost). To account for this effect, a factor $\eta(R)$ was introduced by which the extinction coefficient must be multiplied. The value of $\eta(R)$ is always less than unity, with lower values corresponding to increasing multiple scattering effects. Adding this modification to 6.1 yields

$$P_{lid}(R) = \frac{C_{lid}}{R^2} \frac{\beta(R)}{4\pi} exp\left(-2\int_0^R \eta(R')\sigma_{ext}(R')\, dR'\right) \qquad (6.2)$$

It should be clear that η is a quantity unique to a scattering volume, and should therefore be allowed to vary as a function of range (R). A significant amount of research has focused on characterizing the η value, which is primarily a function

Quantum Efficiency	0.14
Cathode Radiant Sensitivity	5.99E-2 Amps/Watt
Anode Radiant Sensitivity	3.33E+3 Amps/Watt
Dark Count Rate	2.5E+3 Photo-Electrons/Sec
Noise Equivalent Power (@ 1Hz)	2.35E-16 Watts

Table 6.2: LITE detector characteristics (courtesy of NASA Langley Research Center)

of cloud optical depth, scattering phase function, cloud range, and detector FOV. It has been found from ground-based lidar simulations that η increases with cloud penetration distance and then levels off, with typical values of 0.90 to 0.80 for surface lidar (2.0mrad FOV) and 0.30 down to 0.10 for space-based lidar (293km range, 3.5mrad FOV) (Platt and Winker (1995)).

In terms of the lidar equation, the detectability of the lidar return signal is specified by the system constant, the optical properties of the pulse volume itself and medium along the path to it, and the target range (note that the signal is diluted according to $1/R^2$). Because this research was oriented around identifying relationships between pulse stretching and the cloud optical properties, an arbitrary minimum-detectable-signal (MDS) threshold might have been chosen. Values of actual pulse stretching distances will vary according to the hardware and user-defined thresholding as described below. For the sake of maintaining conformity to LITE, however, a threshold was chosen representative of the hardware capabilities of the instrument used in this experiment.

Definition of "minimum detectable signal" (MDS) for any lidar instrument is contingent upon background lighting conditions, the wavelength of operation, the detector gain setting, the attenuator settings, and the amount of averaging allowed. For the 532nm channel of the LITE instrument, the detector characteristics are given in Table 6.2. The MDS is generally defined in terms of the signal to noise ratio. Values were provided from hardware experts at NASA Langley for the LITE

532nm channel for a hypothetical signal-to-noise ratio of unity. For full moon (worst case for night time conditions, single shot (non-averaged) and unsmoothed data, this MDS value is approximately 8.93E-11 Watts. The value used for modeling of pulse stretching was chosen to be an order of magnitude larger than the SNR = 1 value to ensure that the signal would be above the noise.

Given output energy and laser pulse length (see Table 2.1), a normalization by the lidar output power was used to obtain a dimensionless quantity representative of the minimum detectable signal (a fraction of the normalized incident energy as modeled in the MC algorithm). The resulting threshold represented (in an approximate sense) the signal that the 532nm lidar detector would be able to detect in a single lidar shot. In practice, many shots are averaged together, and the *actual* minimum detectable signal is dependent on the system's residual noise among other error characteristics. By modeling for a less-than-ideal scenario, the results derived from the models may be argued to be well within the physical instrument's resolving capabilities. The hypothetical lidar modeled for this study was thus designed to represent an operational instrument, and as such, results were argued to be representative of what this instrument would be capable of resolving in practice

6.1.2 The Scattering Medium

For the initial modeling of pulse extension effects, a vertically homogeneous, plane parallel cloud was assumed. Cloud property inputs to the model are the geometric boundaries of the medium, the extinction coefficient σ_{ext}, the single-scatter albedo ω_o, and the single-scatter phase function $\mathcal{P}(cos(\Theta))$. The Rayleigh (molecular) scattering atmosphere, surface reflection, three dimensional effects, and variability in the atmospheric index of refraction were neglected for the time being, as they only add to the complexity of the first-order problem. These effects must be taken into account when applying the algorithm in an operational scenario, and may in fact provide additional resources to the inversion procedure (*eg*, Rayleigh scattering

and the index of refraction are functions of altitude, surface reflection may enhance multiply-scattering effects over marine stratus layers).

A variety of scattering phase functions were employed in this study in an attempt to determine the ability to retrieve scattering properties of clouds from the observed pulse stretching effects. In addition to the analytic Henyey-Greenstein and Deirmendjian C1 scattering phase functions described in Chapter 5, a unique data set of tabulated phase function values for idealized ice-crystal geometries was provided by Takano & Liou (1995). These phase functions were generated using a "hit and miss" Monte Carlo geometric ray-tracing method which took into account the detailed geometries of commonly found cloud ice crystals (hollow, solid, and capped columns, bullet rosettes, and dendrites). Readers interested in a more thorough description of the ray-tracing methodology are encouraged to seek out the referenced paper. It suffices to state here that the resultant scattering phase functions were highly variable with scattering angle; having strong forward/backward scattering lobes and halo effects which correlate with what is observed in nature. The phase functions were generated for $\lambda = 550nm$.

As with the Deirmendjian C1 cloud phase function, modeling of the Takano & Liou ice crystal ray-tracing data required their representation in an (η, ψ) lookup table. The strength of the forward peaks in these phase functions are immediately evident in Figure 6.1, as over fifty percent of the cumulative distribution occurs within the first degree of scattering angle (the forward scattering peak). These forward-scattering lobes are several orders of magnitude higher than those of the analytic (Henyey-Greenstein) approximations. The impact of this peak on the scattering of the lidar photons is a subject addressed in the following section.

6.2 Visualizing the Multiple Scattering Processes

When a photon interacts with a cloud particle, its energy is either absorbed by the particle or scattered into a new direction according to the composition, phase, and

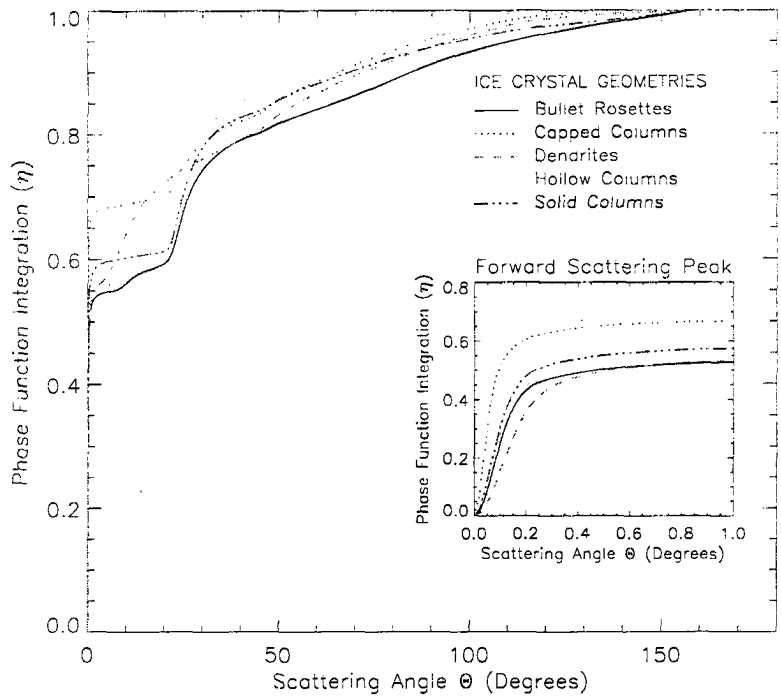

Figure 6.1: The (η, ψ) relationships for Takano & Liou ice crystal ray-tracing results

morphology of the scattering particle. Following a photon's path from its source (in this case, the lidar) into the cloud media, the succession of interactive scattering/absorption events determines its path history. More importantly, it determines whether the photon will ever have an opportunity to return to the detector and thereby contribute to the backscatter signal. Because the closest distance between two points is a straight line (representable here by the single-scattering trajectory), pulse extensions may be related directly to the frequency and amplitude of higher order scatter contributions. In order for these higher order scattering events to contribute to pulse extensions, they must have occurred within the detector field of and have accrued a significant geometric travel distance en-route. Additionally, high order photon scattering events which occur deep within an optically thick media are far less likely to transmit all the way back through the cloud and reach the detector–meaning that the physical depth at which these high order scattering

events contribute to pulse extensions should be preferentially biased towards the top of the cloud (for a nadir-viewing instrument). To characterize lidar pulse extensions in terms of the extinction processes of the cloud media, then, it was necessary to examine contributions to the return signal as a function both of scattering order and of cloud penetration depth.

6.2.1 Parameter-Dependent Qualitative Distributions

To gain a visual feel for the scattering behavior within clouds of varying optical depth (τ), physical positions of scattering events were recorded and plotted on a 3-dimensional grid, truncated at scattering order $N = 150$ (See Figures 6.2 - 6.9). The lidar was oriented nadir (looking straight down) at a range of 292km above a 1km thick homogeneous plane parallel cloud. The points in the figures represent the geometric locations of scattering events in the medium, and provide no information (outside of what is inferable from the bulk distributions) about scattering directions chosen by individual photon trajectories.

There exist three regimes of interest in these figures. The central column of each image is comprised of the scattering events which occurred within the laser beam divergence itself (predominantly direct-beam, first-order-scattering events). Within the secondary shell reside all photon scattering events which are visible to the lidar instrument (they are within the detector field of view). The outer points are events which occurred outside the detector field of view and may only contribute to the signal if they backscatter into the detector field of view–a highly unlikely event for most real scattering media which have relatively low backscattering lobes.

Two sets of scattering phase functions (isotropic and strongly forward-peaked) were plotted for the variety of optical depths shown in order to examine the extreme cases of scattering behavior in the idealized media. It is observed from the figures that at lower optical depths the strong forward peak ($g = 0.9$) of the Henyey-Greenstein phase function tends to distribute the scattering events more widely the

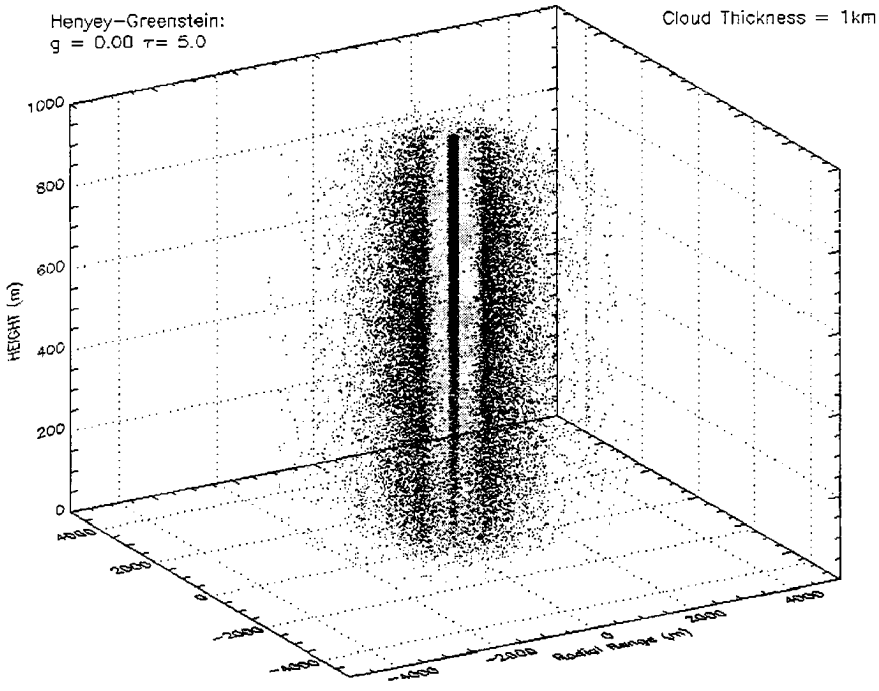

Figure 6.2: Scattering events for $\tau = 5.0$, Isotropic

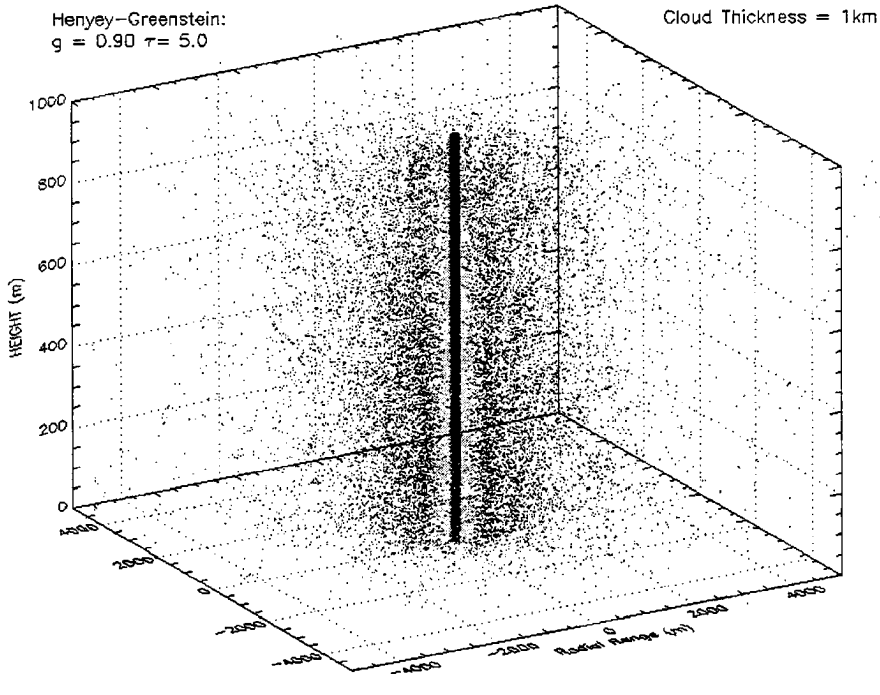

Figure 6.3: Henyey-Greenstein $\tau = 5.0, g = 0.90$

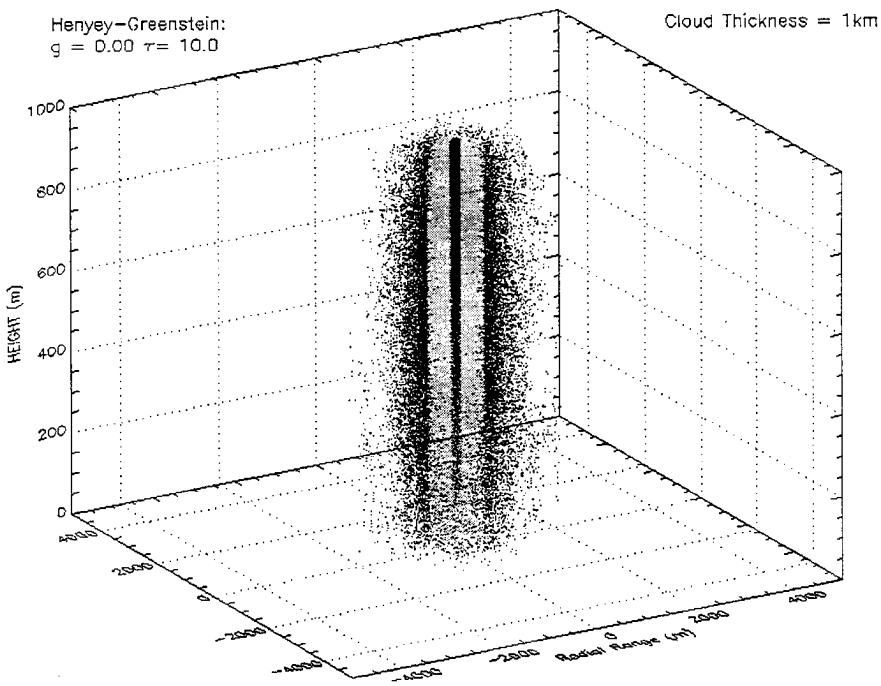

Figure 6.4: Scattering events for $\tau = 10.0$, Isotropic

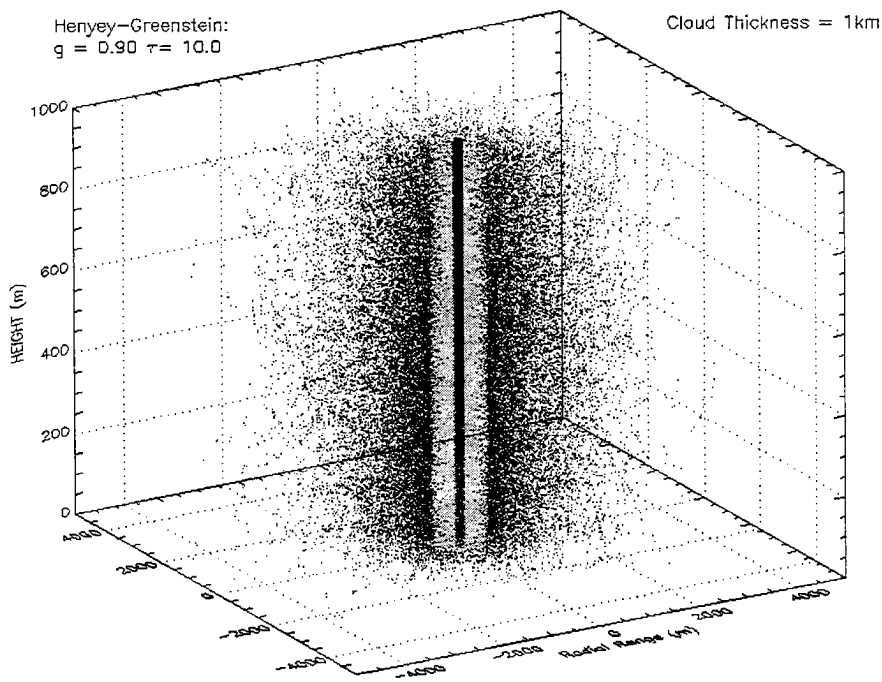

Figure 6.5: Henyey-Greenstein $\tau = 10.0, g = 0.90$

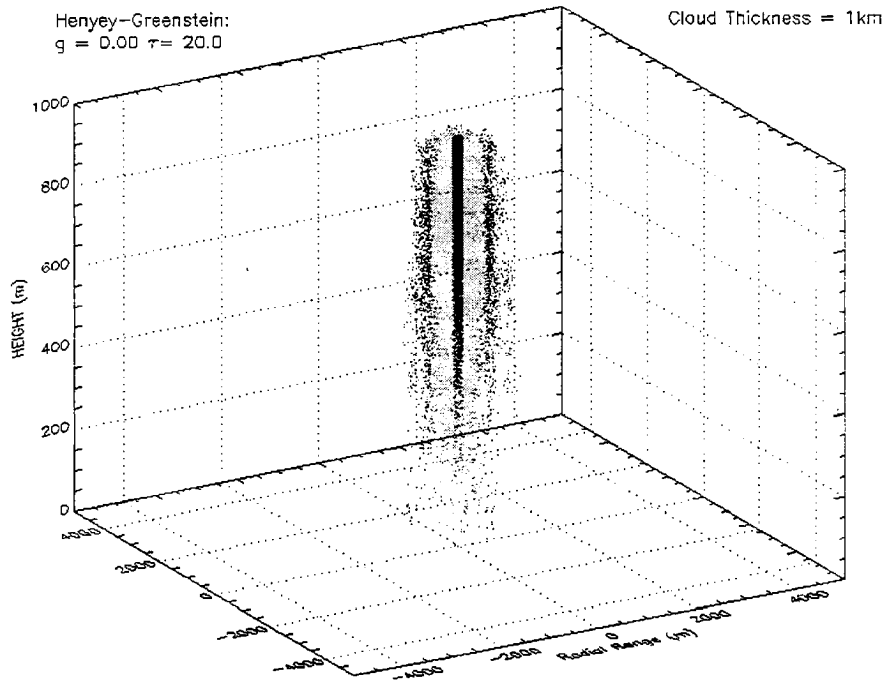

Figure 6.6: Scattering events for $\tau = 20.0$, Isotropic

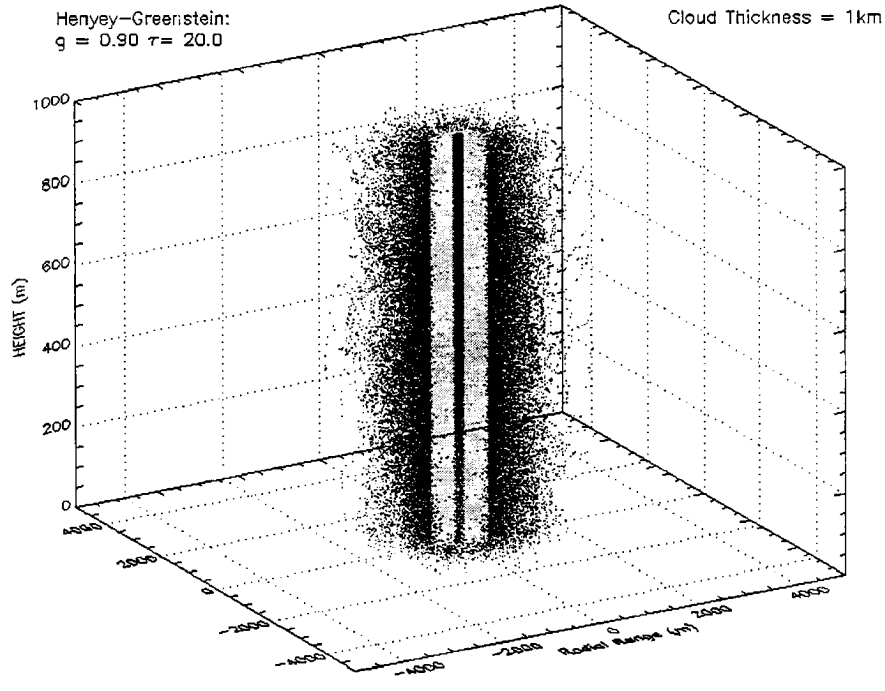

Figure 6.7: Henyey-Greenstein $\tau = 20.0, g = 0.90$

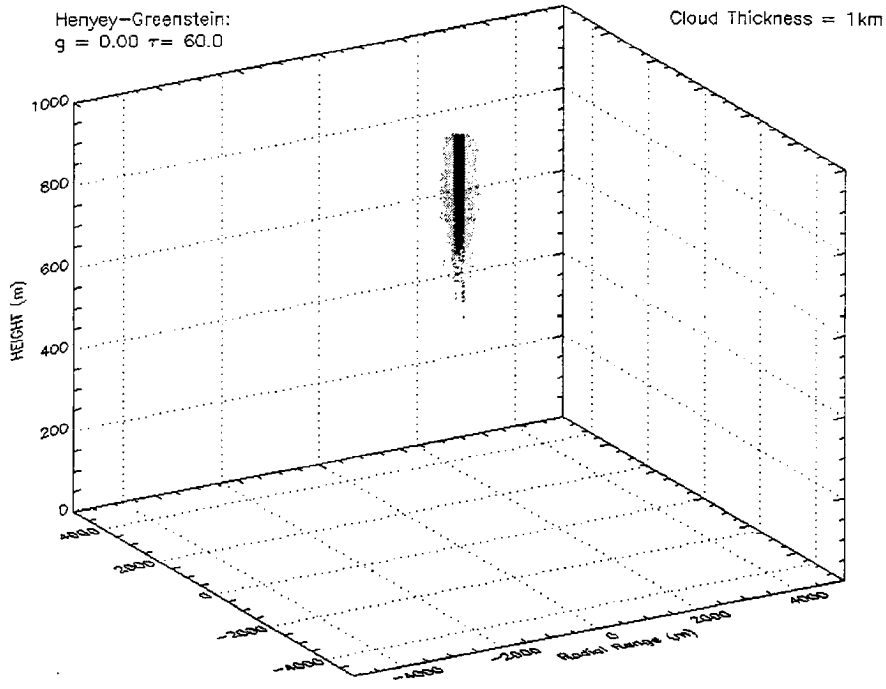

Figure 6.8: Scattering events for $\tau = 60.0$, Isotropic

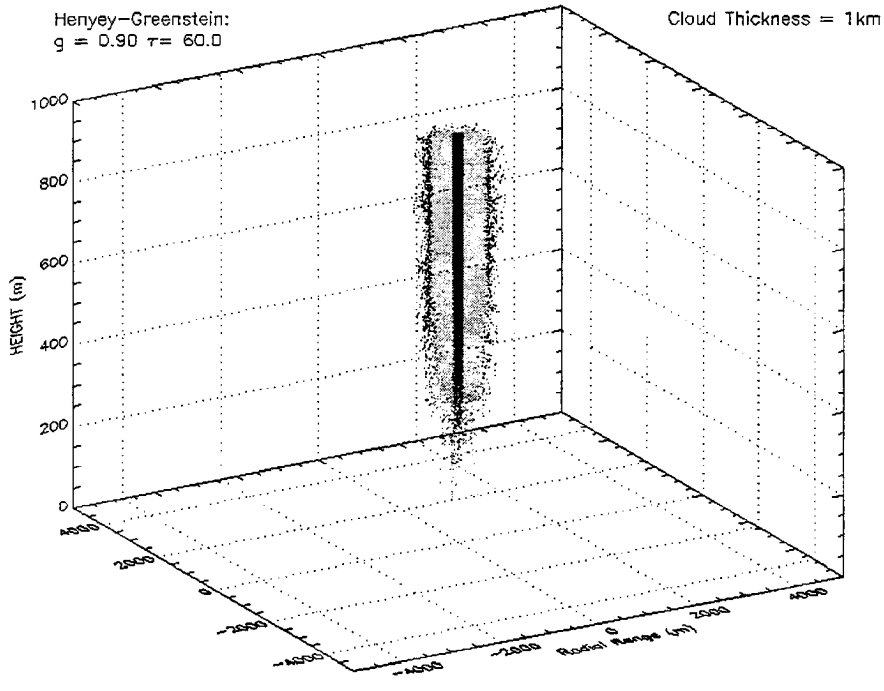

Figure 6.9: Henyey-Greenstein $\tau = 60.0, g = 0.90$

about the central beam, and bias the distribution towards the base of the cloud, whereas the isotropic case yields a more dense distribution closer to the beam. The forward peak lobe of the Henyey-Greenstein scattering phase function serves to preferentially maintain the original trajectories of direct-beam photons. When a photon does encounter a significant radial scattering event, ensuing events are biased towards maintaining this new trajectory (there is no "memory" in the system). This is observed in the strong radial dispersion of scattering events (which initially may seem counter-intuitive for a highly "forward-peaked" phase function). Conversely, an isotropic scattering medium does not allow for such trends to develop (no directional scattering bias) and a result photons tend to cluster more in the vicinity of the initial (first order) scattering events. These tendencies become more obvious for larger optical depths. As τ increases, the photon's free-path distance traveled between consecutive scattering events decreases, and events become increasingly confined to the vicinity of the direct beam (more rapidly converging for the isotropic case for the reasons mentioned above). Implicit to this effect is that more photon scattering events must be occurring within the detector field of view; at higher scattering order, but with relatively lower geometric photon path lengths (for a given scattering order) associated with them.

Increasing the optical depth to larger values, it becomes apparent that the direct beam no longer penetrates the full depth of the cloud. For the isotropic case, all events occurred within the detector FOV and within the top 300m of the cloud. The penetration of scattering events in the strong forward-peaked case is roughly double that of the isotropic medium, and the majority of events are also within the detector FOV. In the actual LITE imagery, such optically thick cloud media are observed to attenuate the beam completely, with a dark region devoid of reflectivity returns present below the level of total apparent attenuation. The general trend of all the figures is for the distribution of scattering events to cluster towards the

incident boundary with increasing optical depth. This makes sense from a physical perspective since optically thicker media inhibit deep penetration. At the largest optical depth shown ($\tau = 60.0$) it is apparent that a significantly higher order of scatter is required for photons to travel the same distance compared to a lower optical depth. While the clustering of events is such that the lower regions of the cloud are unsampled, it is important to note that pulse stretching effects are occurring *within* the cloud. That is, a return signal depth much greater than the actual minimum event depth may be apparent in the imagery. It has been hypothesized that multiple scattering effects allow for the enhanced penetration of of the cloud medium, and hence serve as an aid in the retrieval of cloud vertical structure. While this statement is substantiated by the imagery, the ambiguity introduced by the pulse stretching effects (when necessarily employing a single-scatter ranging algorithm) render this additional depth information meaningless. As is observed from the figures, the contributions responsible for these extended signals need not have originated from the depths at which they were ranged. They represent in-cloud pulse stretching, and these effects will intensify with increasing depth in the cloud.

It should also be kept in mind that the probability of the deepest events transmitting back up through an optically thick medium (to return to the detector) are miniscule; the contributions to the signal will come largely from events closer to the upper boundary in these cases. Hence, the isotropic phase function should exhibit a higher "per capita" contribution to the signal in the model than the highly forward-peaked phase function. The implications of these figures to the modeling of lidar pulse extensions is that, for a given cloud geometry and characteristic scattering phase function, there must exist a critical scattering order below which contributions to pulse extensions are under-sampled–resulting in a tailing off of modeled results. By choosing a sufficient scattering order of truncation (such that the return signal no longer changes with increasing order) and systematically increasing

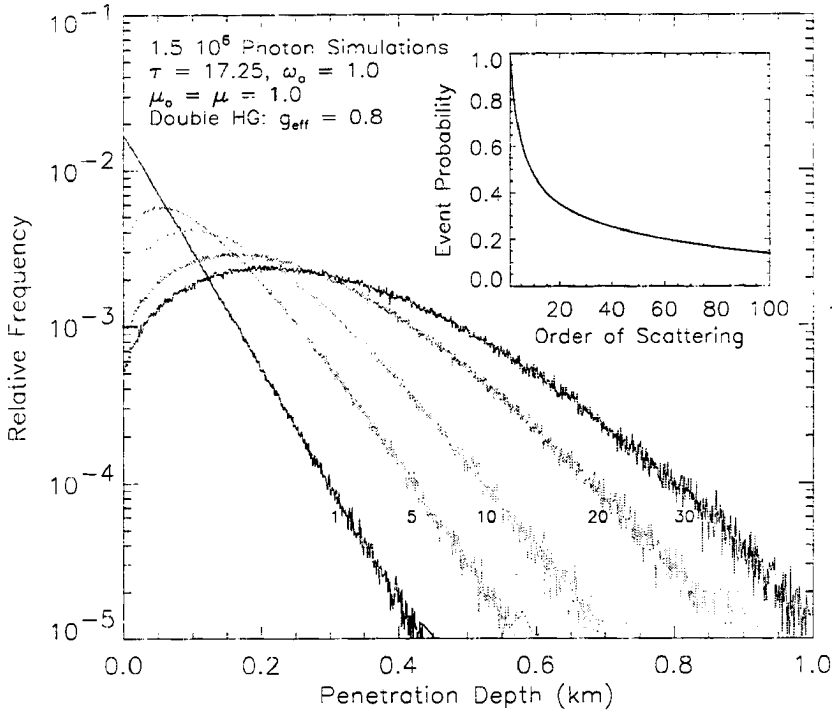

Figure 6.10: An example of modeled scattering order event frequency as a function of cloud penetration depth

the cloud optical depth, this value was chosen to minimize the effects of photon under-sampling.

6.2.2 Parameter-Dependent Quantitative Distributions

A supporting cast of figures were produced in an effort to quantify the distributions of scattering events within the medium. Figure 6.10 provides a two-dimensional view of where the majority of scattering-order events were occurring within the medium. First order scatter dominates at the incident boundary and decays exponentially with penetration depth according to Beer's law of extinction. The peaks in higher-order scattering events are a function of the scattering phase function of the medium. Because backscatter events do occur even in the strongest forward-peaked phase functions, contributions near the incident cloud boundary from high orders or scatter

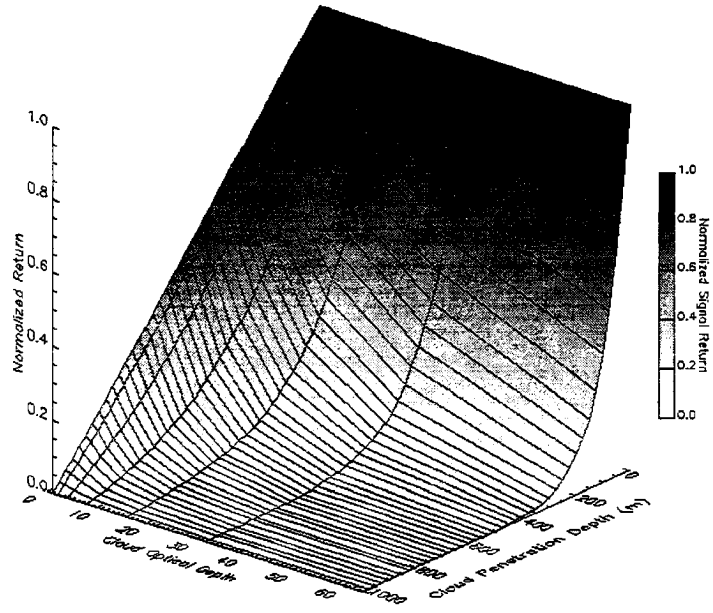

Figure 6.11: Showing the relative contributions to the total intensity as as function of depth within the cloud

are present. These are the photons postulated to comprise the bulk of the pulse extension signal observed in lidar imagery. The inset graph depicts the frequency of events as a function of scattering order, showing that for higher optical depths multiple scattering is far from insignificant. The signal return normalized with respect to the return from the top of the medium was computed as a function of cloud penetration depth in Figure 6.11. It is observed that as optical depth is increased the distribution of signal returns shift toward the incident boundary (corresponding to a cloud penetration depth of 0.0 in the figure). This both corroborates and quantifies the deductions made from Figures 6.2 - 6.9.

Contour plots were created to investigate the contribution to the intensity as a function of cloud penetration depth, optical depth, and scattering order. Figure 6.12 utilized a double Henyey-Greenstein phase function ($g1 = 0.85, g2 = -0.6, b = 0.97$) and shows contours of the signal normalized with respect to the total return as a

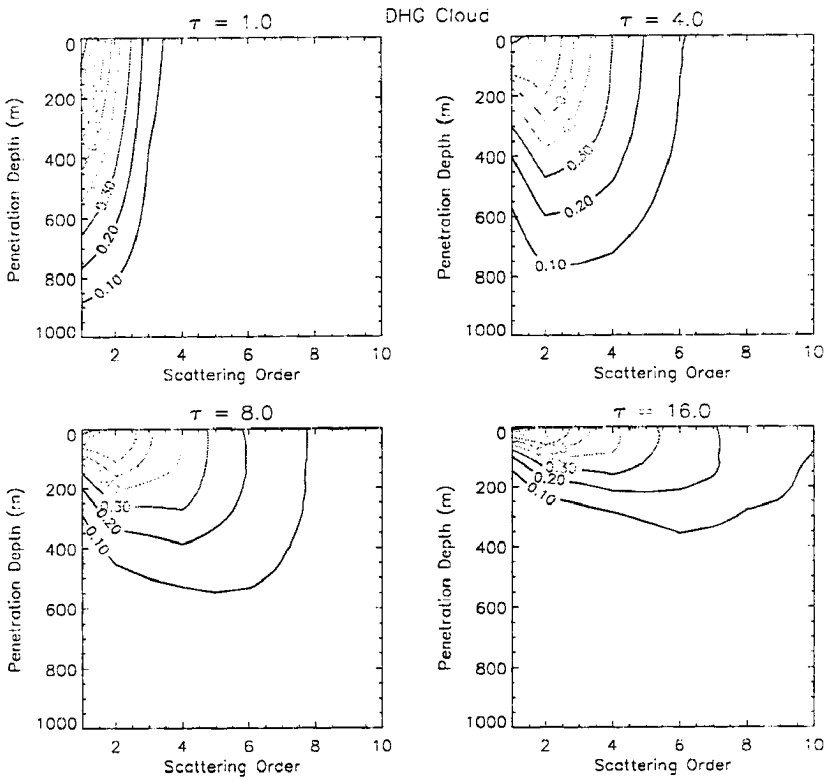

Figure 6.12: Double Henyey-Greenstein scattering order contributions as a function of cloud penetration depth

function of penetration depth within the cloud. As expected, intensity falls off with penetration depth. Contributions shift toward the incident cloud boundary for larger optical depths for all orders of scatter, and towards higher scattering order with penetration depth. To achieve appreciable pulse stretching, both high orders of scatter *and* significant photon path lengths are required. Another way of looking at the contributions as a function of scattering order, cloud optical depth, and cloud penetration depth is offered in Figures 6.13 - 6.14 The propagation of photons through the forward-scattering medium roughly follows the expected distribution of scattering events determined by the mean free path ($1/\sigma_{ext}$). As an example, for a 1km thick cloud with $\sigma_{ext} = 10.0$/km, the mean free path is 0.1 kilometers. Then, for a strongly forward-scattering medium the peak in 10^{th} order scatter should occur around 1.0km, as is observed in Figure 6.14. At lower optical depths fewer high-scattering-order photons remain in the medium, as is evident in the marked

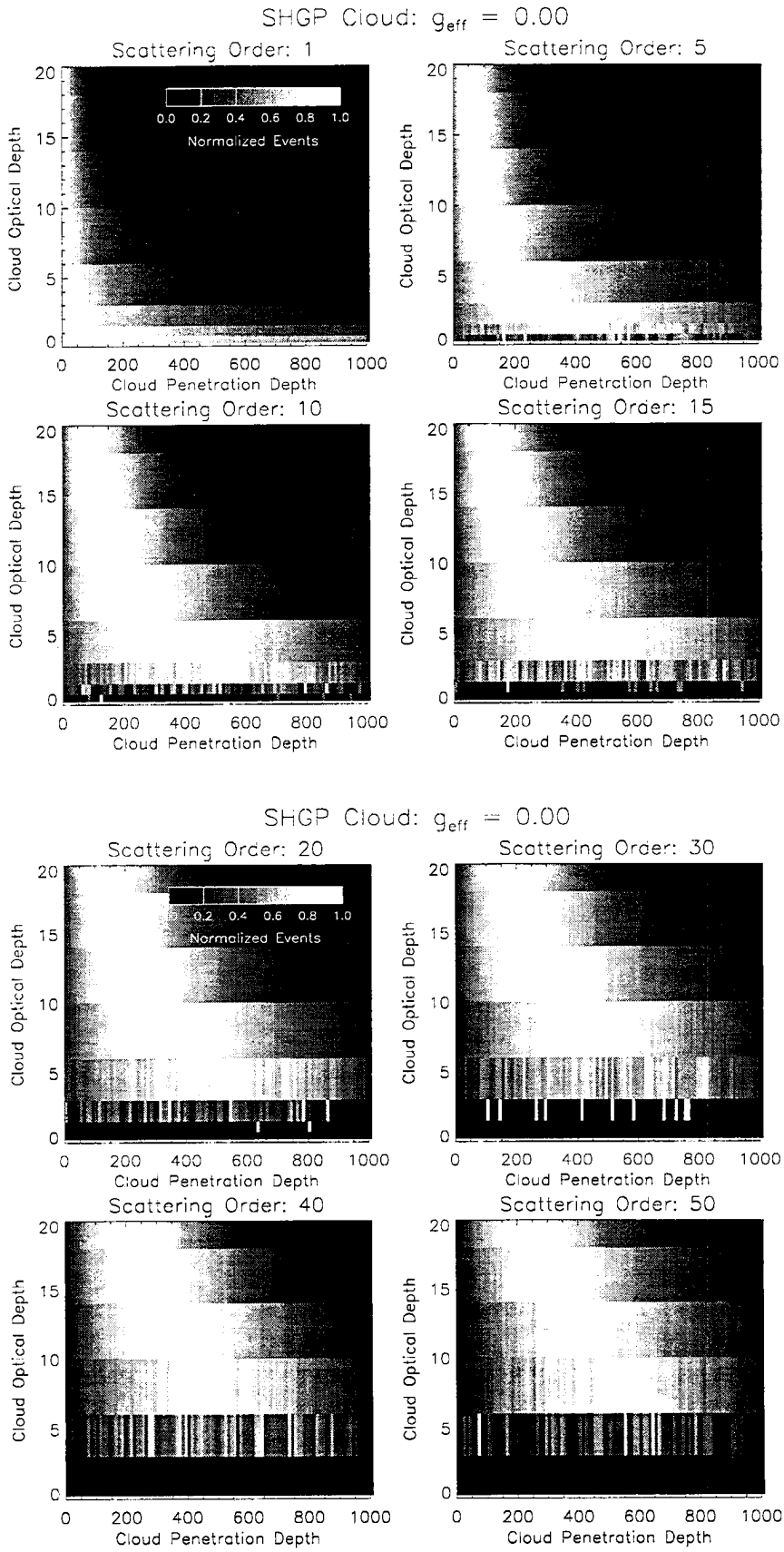

Figure 6.13: Distributions of scattering events for isotropic medium

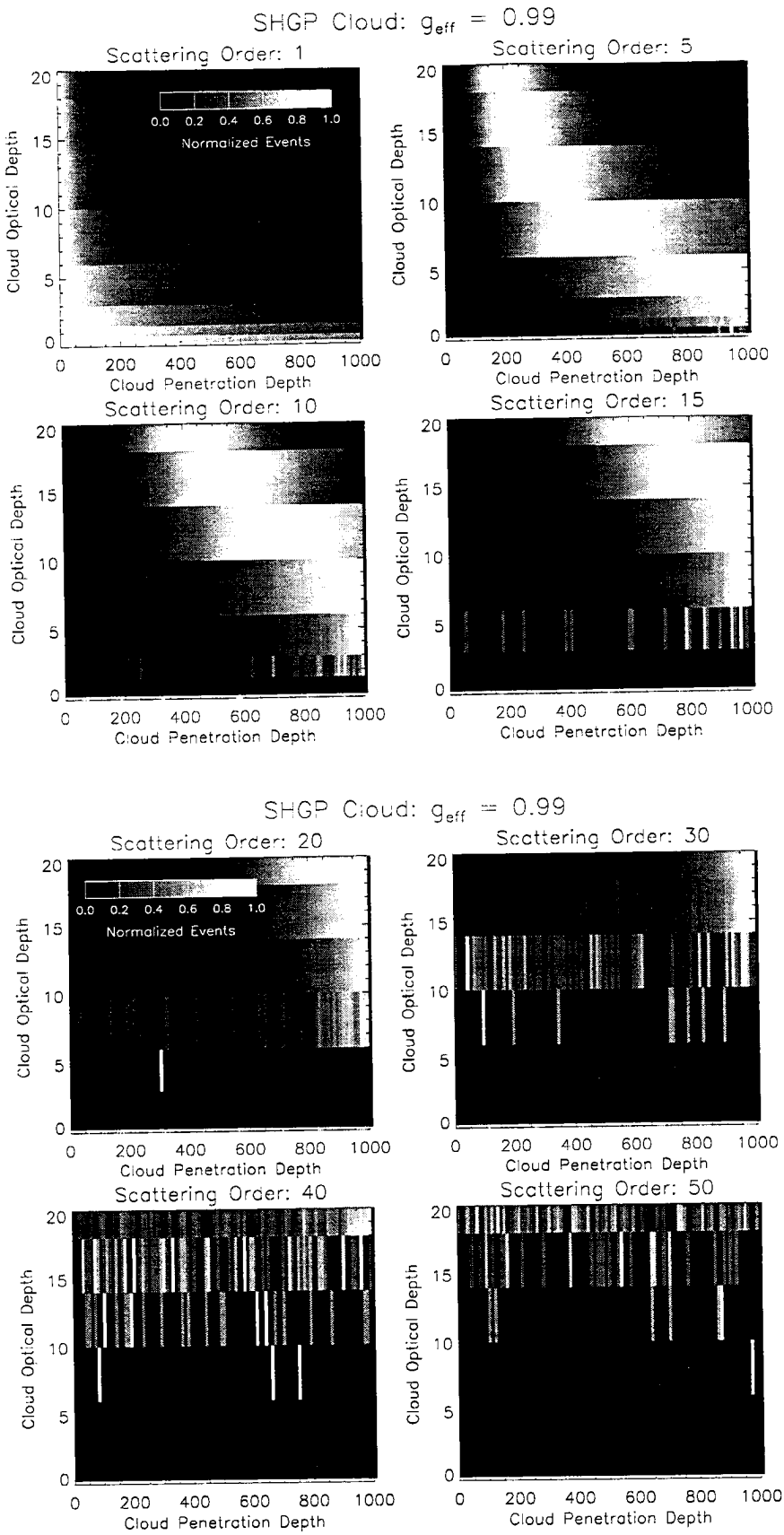

Figure 6.14: Distributions of scattering events for a highly forward-scattering medium

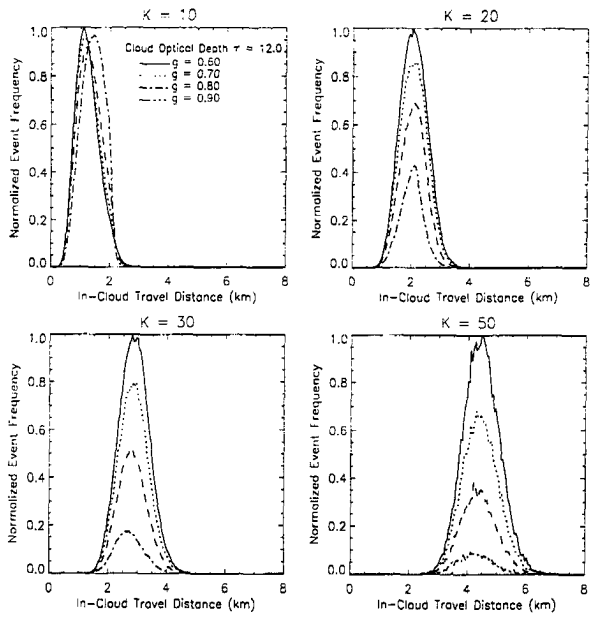

Figure 6.15: Photon path length distributions as a function of cloud optical depth and asymmetry parameter, shown for several scattering orders.

drop-off of scattering events in the lower regions of these plots. Keeping in mind that these events are weighted-down by the transmission required to retrace through the medium to the detector, higher-order scattering distributions which peak closer to the incident surface should contribute to the return signal more readily.

6.2.3 Photon Path Length Histories

Photon path length distributions, $P(\lambda)$, were also recorded as a means of examining the bulk geometric travel distances "brought to the table" from the higher-order scattering contributions. Figure 6.15 is an example of these distributions, plotted for a 1km thick cloud as a function of cloud optical depth for a variety of scattering orders, again for the Henyey-Greenstein scattering phase function. The lidar was again placed at 292km above the top of the cloud. Only photon path histories within the detector field of view were considered. For the cloud/lidar geometry used, an optical depth of $\tau = 12.0$ allowed for sufficient containment of photons such that

distributions of path lengths could be compared over the scattering asymmetry parameter range of $g = 0.60$ to $g = 0.90$. The distributions were normalized with respect to the $\tau = 12.0, g = 0.60$ maximum value for each scattering order shown. The normalization was done with respect to $g = 0.60$ as it represented the most isotropic of the cases examined and therefore produced the highest frequency of scattering events within the detector field of view. This exercise was done in order to examine the relative differences in the cloud asymmetry parameters as a function of increasing scattering order. At $K = 10^{th}$ order scatter, contributions are similar for all g. As K increases, the mean of the distributions shift to higher in-cloud distances of travel and relative contributions for higher forward-scattering peaked phase functions decrease. The distributions essentially reiterate the information provided above and substantiate the explanation of the peak in scattering event distributions for highly forward peaked scattering phase functions in terms of the mean photon path length, with relatively fewer photons remaining both in the cloud and within the detector field of view at higher scattering orders.

6.2.4 Radial Scattering Distributions

It has been postulated that in order to achieve *significant* accumulated photon path length distance (leading to strong pulse stretching effects) a photon must undergo scattering in directions normal to the direct beam while remaining within the detector field of view. The radial distribution of scattering events, then, may be considered as a proxy to the pulse stretching expected in any given media. Figure 6.16 is an example of scattering event frequency as a function of radial (orthogonal to the direct beam for all azimuthal angles) distance for a variety of cloud optical depths, asymmetry parameters, and fixed detector FOV of 3.5mrad. The data were examined for $K = 40^{th}$ scattering order and normalized with respect to the $g = 0.6$ maximum event value in order to compare the relative differences between other cloud asymmetry behaviors. Only photon scattering events which occurred within

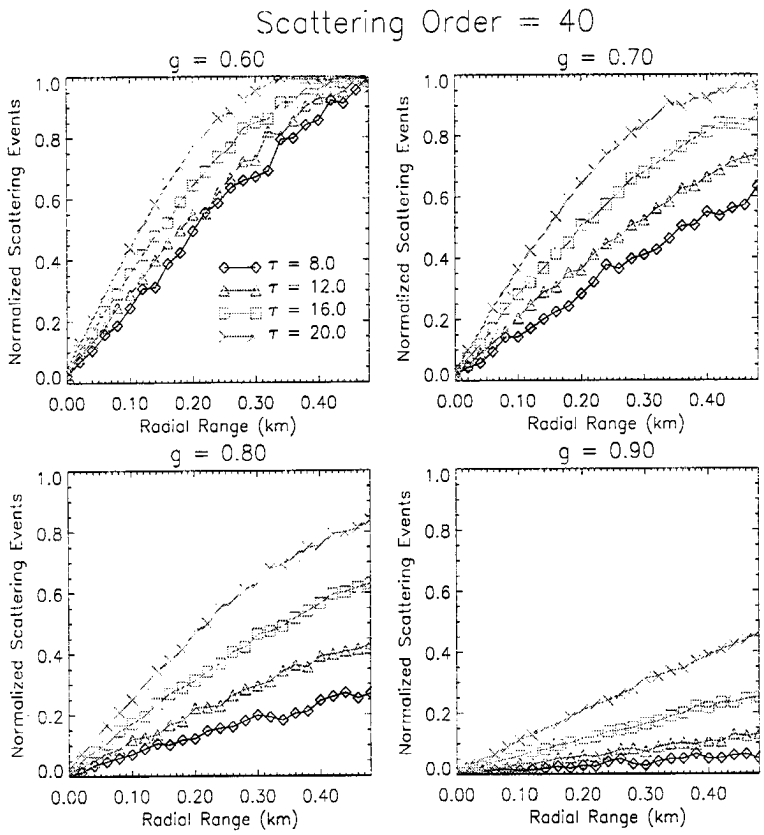

Figure 6.16: Radial scattering event distributions for several cloud asymmetry parameters at 40^{th}-order scatter.

the detector field of view were considered. Scattering event frequencies at 40^{th} order increase with radial range and increasing cloud optical depth. The former point is supported by the observation that photons tend to diffuse radially from the direct beam with increasing scattering order, and the latter point holds due to the decrease in mean photon path length (maintaining higher scattering orders within the cloud medium and detector field of view).

6.3 Field of View Analysis

As an additional examination of the relative contributions to the lidar signal from multiply-scattered photons, the detector solid angle (defining the instrument's field

of view) was allowed to vary. It was expected from a purely physical argument that expanding the detector the field of view would result in a greater number of received photons. Depending on the extinction coefficient (σ_{ext}) of the cloud, the radius of the area projected by the detector FOV (assuming a nadir-viewing instrument) may be significantly larger than the mean free path ($1/\sigma_{ext}$) of a photon. Considering radially-scattered photons (normal to the direct beam) this means that photons significant to pulse stretching will have a better opportunity to contribute to the return signal.

Because backscattering events are unlikely in most real scattering phase functions, once a radially traveling photon exits the FOV it is unlikely to ever return (this premise may be utilized in Monte Carlo lidar simulations as a means of accelerating convergence). For optically thick media it may also be expected that a point will be reached when increasing the detector FOV will no longer result in an appreciable change in the signal return (all scattering events within the medium being confined to a finite volume, with losses due only to photons escaping the upper or lower boundaries of the cloud or absorption by the medium). Because an increase in multiply-scattered photons results from the increase of detector FOV, an accompanying increase in lidar pulse stretching effects may also be inferred.

In an international workshop assembled to address the issues of lidar multiple scattering in cloud media, several models were used on a common problem and their results compared. The models ranged in approach and complexity from Monte Carlo (stochastic) models to radiative transfer (analytic) approaches. For the common problem, a 300m thick Deirmendjian C1 cloud was chosen, with the lidar instrument oriented nadir at a range of 1km. The detector field of view was switched between 1mrad and 10mrad, and the laser beam divergence was specified as 0.1mrad. Further description of the common problem may be found in Bissonette *et al* (1995). As with the Monte Carlo results used in this thesis, the signal returns were representable

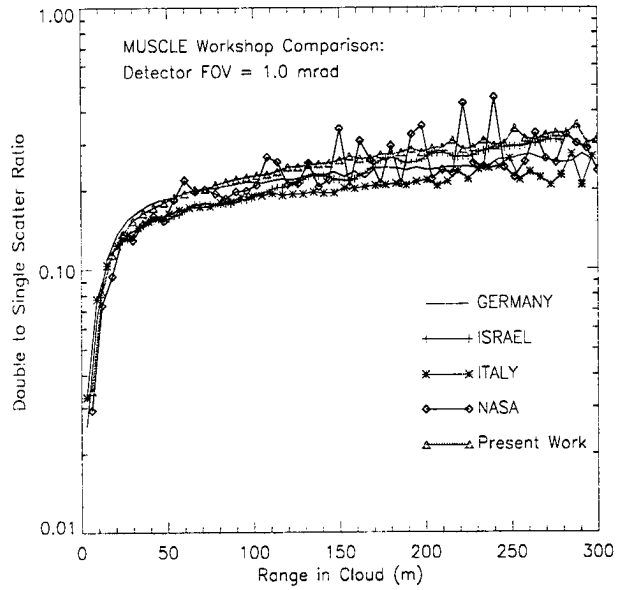

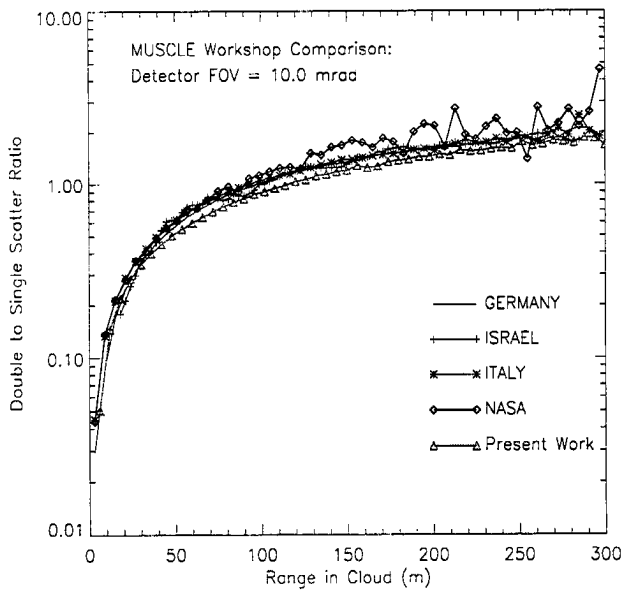

Figure 6.17: Double-to-Single scattering event ratios

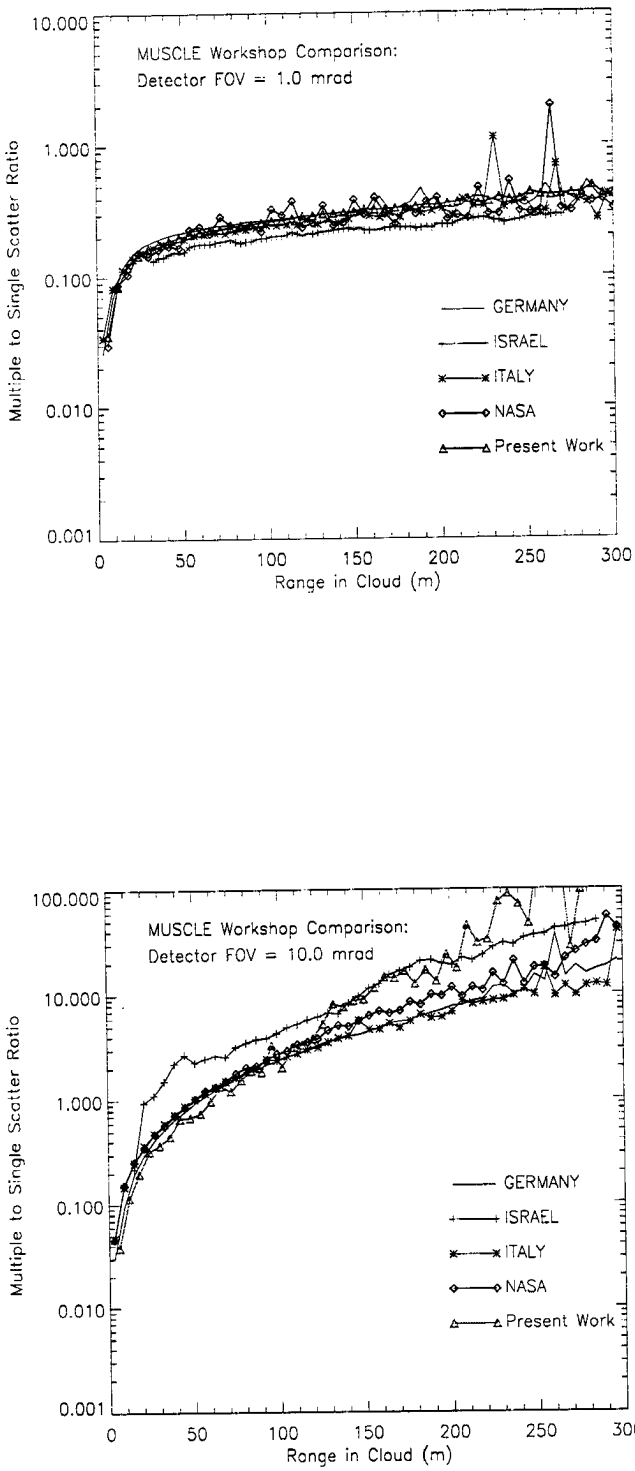

Figure 6.18: Multiple-to-Single scattering event ratios

as the sum of the multiple-scattering series. As such, relative contributions to the total signal as a function of scattering order were computable, and served as a useful diagnostic between the models. The collective results of the MUSCLE workshop for double-to-single and multiple (the total signal from scattering orders greater than 1)-to-single scattering signal return ratios as a function of geometric depth in the cloud medium are shown in Figures 6.17 - 6.18 along with the corresponding results from this present study. Two million photon trajectories were simulated for this comparison, and the scattering-order truncation was invoked at $K = 30$.

The curves show a generally good agreement between the MUSCLE results and the present study, which made use of a tabular C1 array taken directly from Kunkel and Weinman (1976) at a significantly coarser angular resolution compared to that used by the MUSCLE workshop participants. As multiple scattering becomes increasingly significant with cloud penetration depth, the discrepancies between the two scattering phase functions account for the divergence in results. Comparing the 1.0 mrad and 10.0 mrad sets of curves for the multiple scattering to first-order scattering ratios, it is evident that multiple scattering effects are not negligible, and are a strong function of the detector field of view. The 2:1 ratio curves show relatively little difference between the two FOV, as the 1.0 mrad FOV captures a majority of the second-order scattering events.

Extending this problem to the space platform, scattering-order ratios were again investigated as a means of observing the enhanced contributions to the signal from multiply-scattered photons. The lidar was placed 292km above a 1km-thick cloud and ratios of the frequency of double and total-multiple scattering events were computed with the single-scatter alone. These ratios were computed for a variety of cloud optical depths ranging from 1.0 to 20.0 and for a detector FOV of 3.5mrad. Figure 6.19 indicates a significant enhancement of multiple scattering events with increasing depth in the medium. The incompleteness of the curves at higher optical depth is due to the absence of single scattering events occurring at the deeper

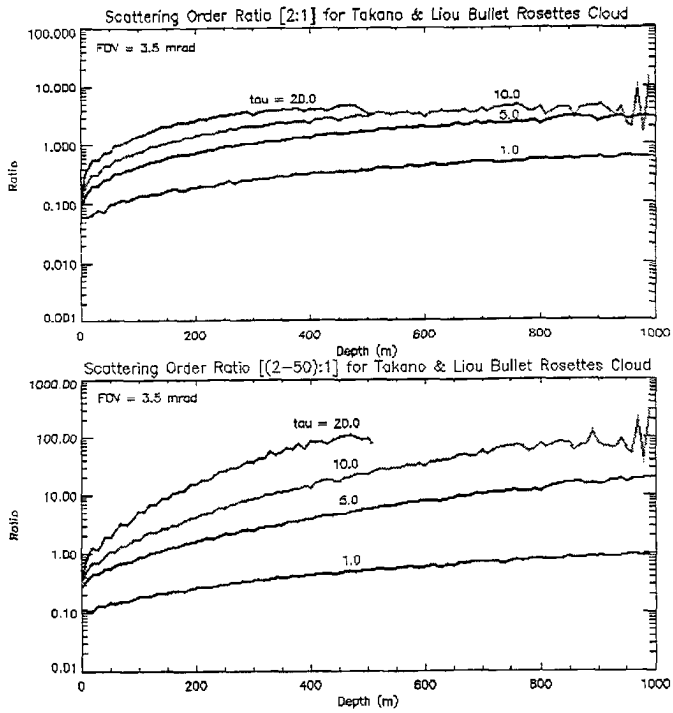

Figure 6.19: Scattering event ratios at orbit altitude of 292km for a detector FOV of 3.5mrad

regions of these optically thick media. All the curves reveal a rapid increase within the first 50 meters of cloud penetration with a decreasing positive slope through the extent of the cloud.

As mentioned earlier. in order to account for the increasing number of returning photons in the Monte Carlo model with increasing detector FOV it was necessary to monitor carefully the truncation of scattering order. This procedure was carried out for a variety of optical depths, asymmetry parameters, and detector FOV. Figure 6.20 is an example of this exercise, and shows the expected trends in required scattering orders as a function of optical depth and FOV. The instrument was placed 292km above a 1km thick cloud media. Convergence was defined as when the model converged to within 0.5 percent, and the thresholding used for truncation in the plot was specified at within 3 percent of this value. For larger fields of view and cloud optical depths it is evident that a high order of scattering events must be

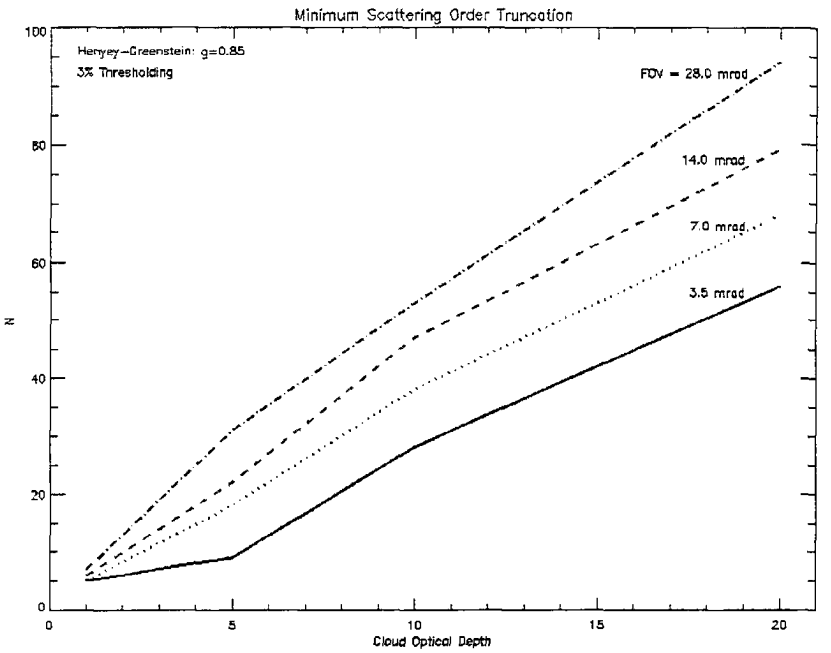

Figure 6.20: Scattering order thresholding values required to capture the total return signal to within 3%

considered. These results were used as benchmarks for specification of minimum scattering order truncation in the model simulations.

6.3.1 Varying FOV Radial Contributions

Radial contributions to the lidar signal were examined for a fixed detector FOV in Figure 6.16. Contributions to the return signal as a function of radial (with respect to the laser-axis) distance determines the the locus of detector FOV's which will exhibit appreciable variations in return power (and hence, contain additional pulse extension information). Figure 6.21 demonstrates the expected asymptotic nature of the return signal with increasing detector FOV. In this case, the lidar was 292km above the cloud top. The maximum FOV required to capture all the available signal varies both with the lidar-target geometry and the optical thickness of the cloud.

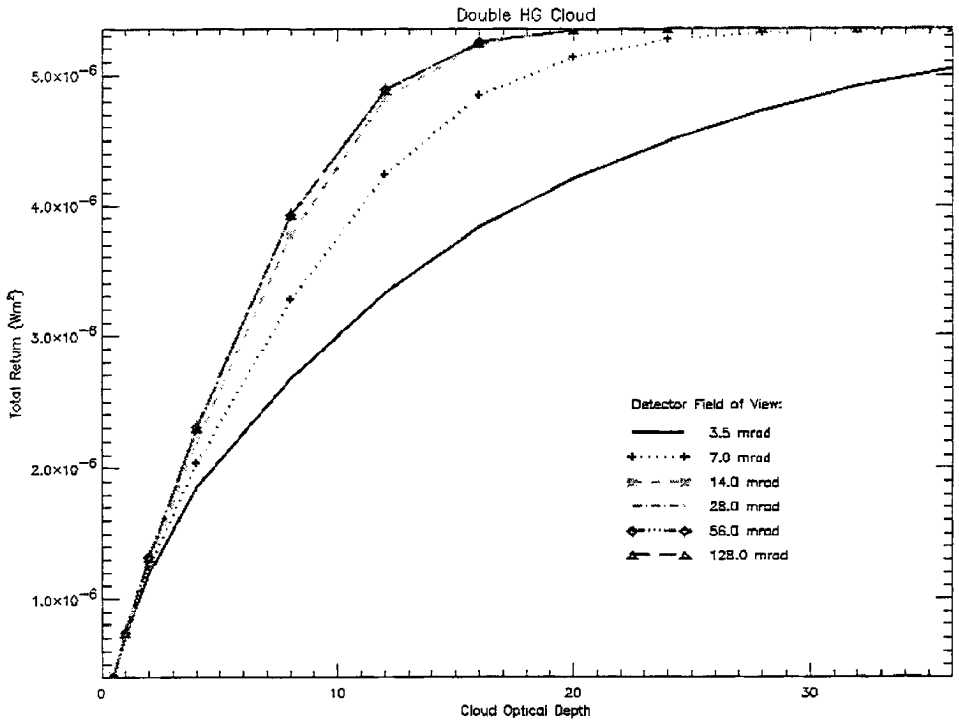

Figure 6.21: Asymptotic signal return with increasing detector FOV for Double HG phase function cloud (g=0.85)

lidar applications at closer ranges will require increasingly higher FOV apertures to attain same spatial coverage as a space-borne instrument.

Contributions to the total return signal as a function of radial distance from the direct beam axis are shown in Figure 6.22. As in Figure 6.21, the lidar was placed 292km above a plane parallel cloud field, with a Deirmendjian C1 scattering phase function employed. The four panels represent four different detector fields of view, and the twelve curves on each panel are cloud optical depths ranging from 1.0 to 36.0 at a $\lambda = 532$ nanometers (τ indices are given in the fourth panel, and apply to all the plots). Radial cutoffs in the optical depth curves indicate where the finite detector field of view truncates the signal returns. The figures show that radial contributions decrease with increasing optical depths. For this particular geometry,

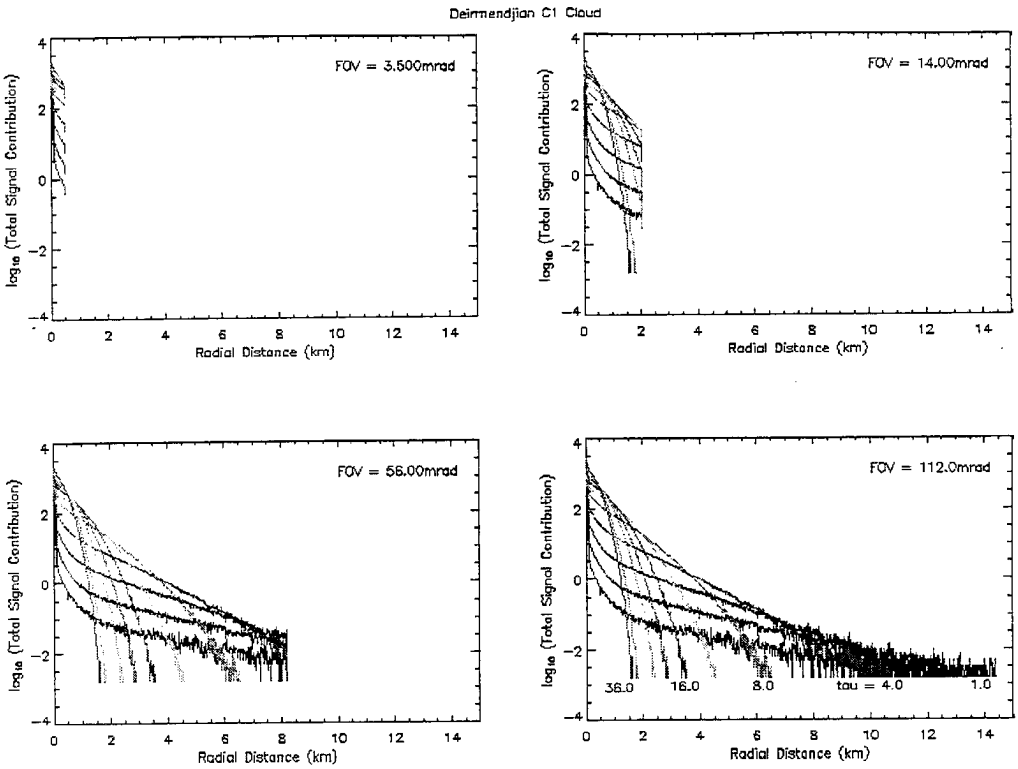

Figure 6.22: Radial contribution to signal return as a function of detector FOV and optical depth for a Deirmendjian C1 cloud

it is observed that a detector field of view somewhat less than 56.0 mrad will suffice to capture the total available signal for all cloud optical depths shown.

From the examples above, it is expected that higher forward-peaked scattering phase functions will exhibit a relatively high signal contribution component at larger radial distances compared to less forward-peaked media, since an off-laser-axis trajectory will tend to continue on this track. Quantifying the change in pulse stretching distances with change in detector FOV might provide the independent measurement needed to separate simultaneous retrieval solutions.

6.4 Summary

Understanding the distributions of multiple scattering in the lidar problem is key to the accurate description of the physical processes leading to pulse extensions.

The modeling of multiple scattering behaviors within a variety of cloud media was conducted in an effort to understand the significant contributers to lidar pulse stretching. As cloud optical thickness increases, scattering event distributions were observed to shift towards the incident boundary as mean photon path lengths decrease. Cloud scattering phase function geometry also dictated the behavior of this distribution, as higher forward-scattering phase functions allowed for an enhanced penetration through the cloud over that of less "peaky" phase functions. Investigation of these effects lead to the conclusion that an instrument with a variable FOV detector may be able to provide additional information about the medium's bulk scattering phase function asymmetry. Definition of a minimum detectable signal, although a somewhat innocuous quantity, was necessary in order to carry forth with a consistent means of truncating the model returns and comparing pulse extension distances.

Chapter 7

MODELING LIDAR PULSE EXTENSIONS

Having gained a familiarity with the general behavior of multiple scattering processes within cloud media of various optical properties, the stage was set to proceed with a formal discussion of the modeled pulse extensions. While the modeling environment is highly simplified with respect to what is posed by Nature, the fundamental drivers of pulse stretching behaviors (optical thickness and asymmetry parameter) are believed to be sufficiently characterized in the model to first order of approximation. The first goal is to understand the "cause and effect" relationships on the most basic level. Extension of the modeling to more complex systems will follow with confidence. This chapter covers the modeling procedures and results of the lidar pulse stretching features; addressing specifically their quantification in terms of the driving cloud optical properties and viewing geometries considered. It then speaks to the complicating issues of examining pulse stretching in multiple cloud layer and 3-dimensional variable cloud environments.

7.1 Book-Keeping Protocols

As mentioned previously, pulse stretching effects occur throughout the depth of optically-thick cloud media. A standard measurement was needed which could be used to directly compare the pulse stretching behaviors as a function of cloud optical

properties and serve as measurable quantity in practice. Because cloud boundary locations are generally considered as a measurable quantities by active instruments, the extent of "cloud return" below this level could be immediately attributed to multiply-scattered contributions. An alternative approach might be to apply an annulus to the detector such that the entire multiply-scattered component of the signal is used (the scattering events within the laser beam divergence may be approximated as primarily first or second order scatter). In this way, a ratio between multiple and single scattering contributions would serve as the measurand, and no *a priori* knowledge on the true cloud base is required. The former method was attempted here was chosen for no other reason than its immediate observability in the LITE returns.

Pulse extensions were computed by binning contributions from a subset photon path histories; those whose path-lengths were greater than the nadir round-trip distance from the source to the base of the scattering medium and were within the detector field of view. Since the ranging algorithm deals only with a simple time-to-distance conversion, the physical path actually traversed by a photon within the cloud is, in reality, immaterial (recall that for the single-scattering assumption the ranging is exact, whereas ambiguity is introduced via the MS process) to pulse stretching distances. To the modeler attempting to extract cloud information from these one-dimensional quantities, however, knowledge of these paths (in a statistical sense) is a powerful diagnostic.

In accordance with the simple single-scatter ranging algorithm, distances in excess of a round-trip distance defined from the lidar to the base of the medium (along the central beam axis) were flagged as "contributing pulse-extension events" and binned as a function of distance below cloud base. Depending on the physical properties of the medium, the contributing photons exhibited varying degrees of pulse extension with change in cloud optical depth and/or variation of the scattering

phase function. The largest pulse extensions occurred for the (τ, g) combinations that enhanced the number of high-order scattering events near the incident boundary of the cloud *and* maximized the detector field of view volume in which they occur (ie relatively low σ_{ext}).

Increasing the cloud optical depth, by definition, decreases the photon mean-free-path $(1/\sigma_{ext})$ of travel, meaning that shorter travel distances will be accumulated as a function of scattering order. Because a truncation of scattering order is enforced on the algorithm, there exists the possibility that some higher-order contributions to pulse extension may be overlooked by the model, and a slight underestimation of pulse extensions will therefore result for cases of higher optical depths (the value is dependent also on the the detector field of view). The determination of a suitable scattering order truncation value (see Chapter 6) was done to minimize this affect. This research intentionally focused upon cloud extinctions and detector fields of view which were within the model's capacity to handle. Any inferences made beyond these thresholds must be made only with the caveats of high order scatter limitations fully in consideration.

7.2 Model Results

The first modeled pulse extension results were computed for all scattering events (regardless of contribution weight) that were both within the detector field of view and had accumulated geometric path lengths exceeding the single-scatter round-trip distance to the cloud base (according to equation 5.10). Figures 7.1 - 7.2 are for a Deirmendjian C1 cloud, showing beyond-base extensions of the return signal as a function of optical depth as well as photon scattering order. The exercise was carried out for a simple case of a 1km thick vertically homogeneous plane parallel cloud (described in Chapter 6), with optical depths τ ranging from 0.5 to 36. The distributions are seen to increase in frequency, broaden, and shift toward higher

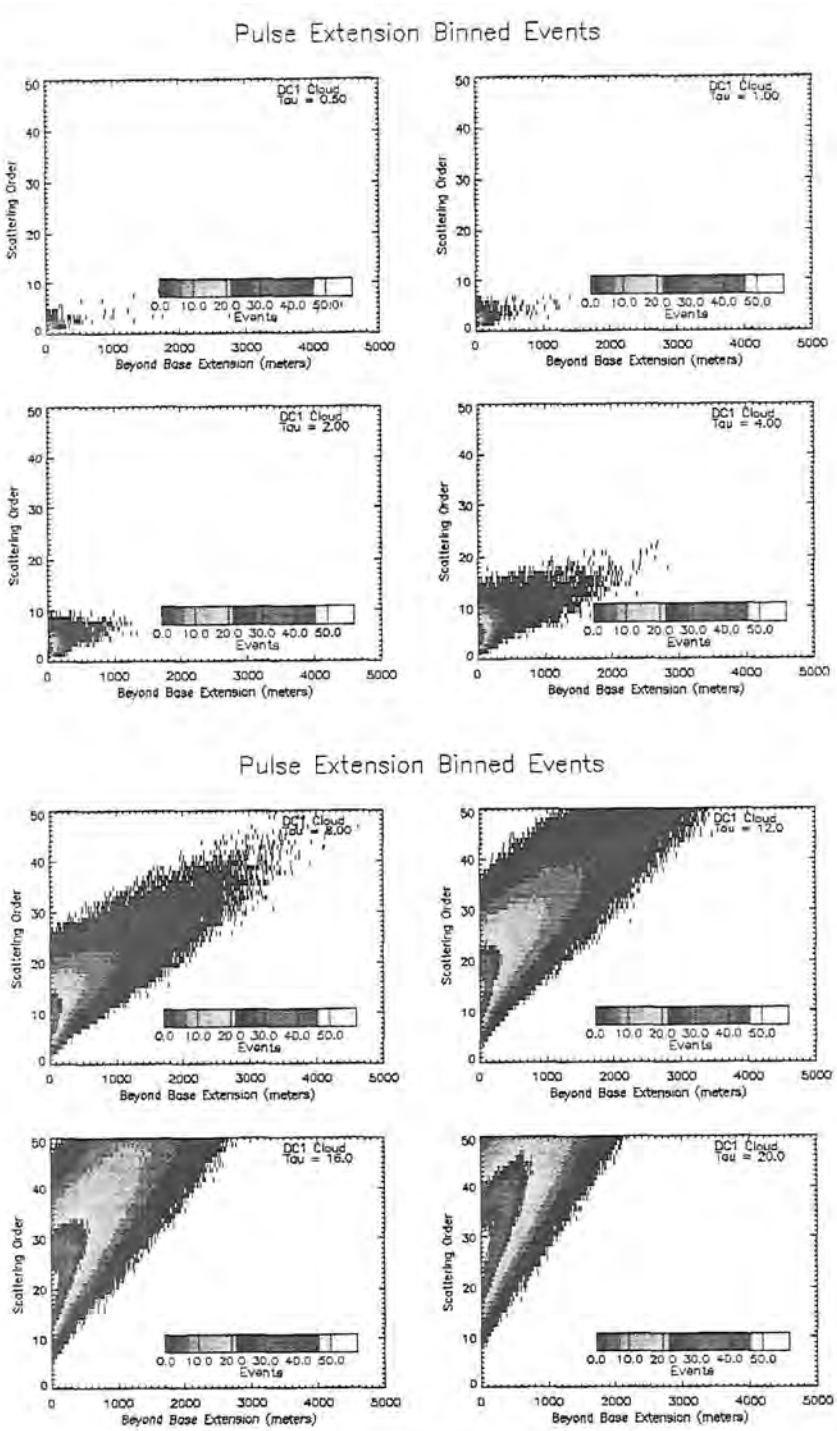

Figure 7.1: Pulse extension as a function of photon scattering order for $\tau = 0.5$ through 20.0

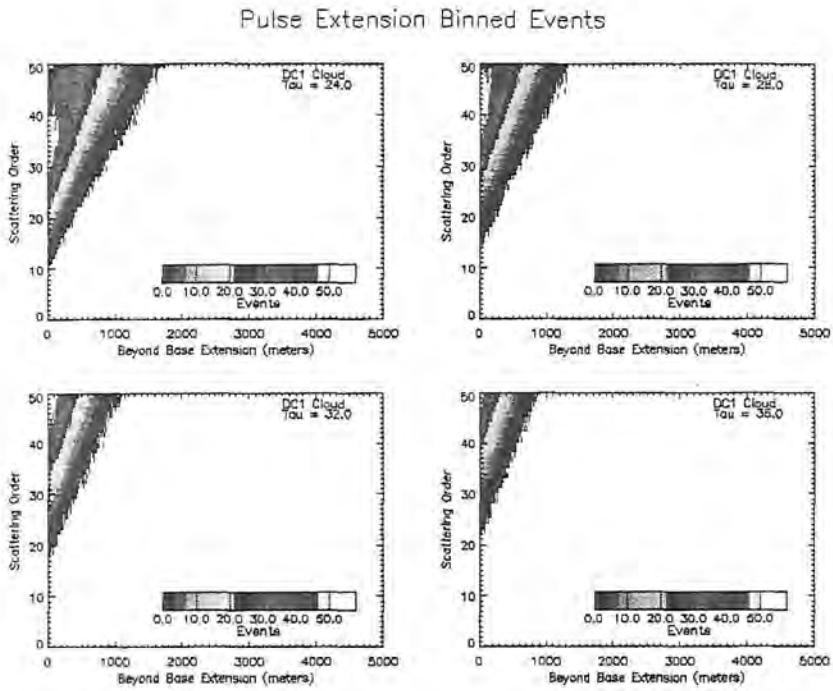

Figure 7.2: (Figure 7.1 Continued) Pulse extension as a function of photon scattering order for $\tau = 24.0$ through 36.0

scattering orders with increasing cloud optical depth. The tail of the distribution roughly defines the extent of the actual pulse extension signature. As τ is increased further, the slope of the distributions steepen, and the beyond-base extensions within the scope of the scattering order truncation (in this abbreviated case, $K = 50$) begin to decrease. This re-illustrates the need to sufficiently account for higher order scatter in the model simulations.

7.2.1 Cloud Parameter Sensitivities

Investigation of pulse stretching as a function of the scattering phase function required a systematically-variable phase function representation. For this purpose, the Henyey-Greenstein scattering phase function was selected. In this way, pulse extensions could be characterized in terms of a "bulk asymmetry parameter" associated with the cloud. Pulse extension events were then plotted as a function of varying

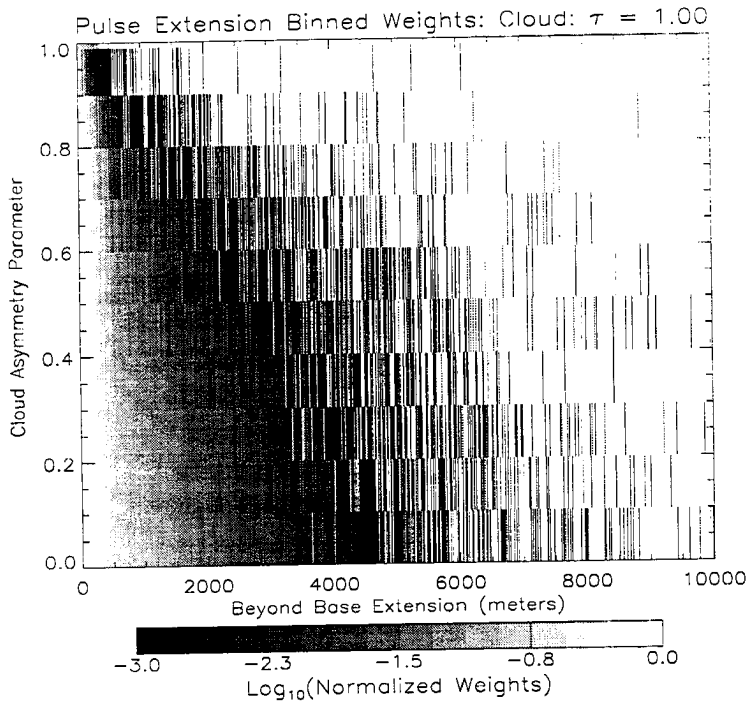

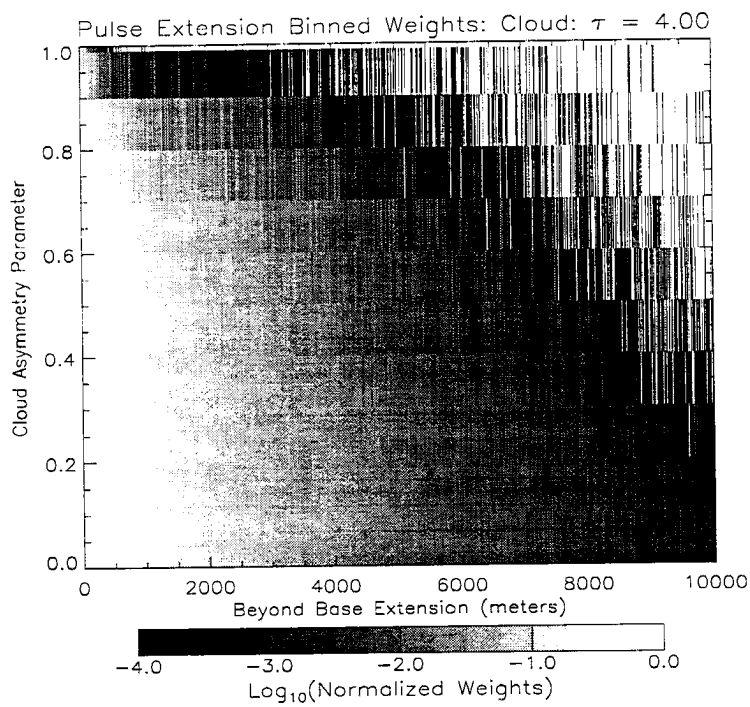

Figure 7.3: Pulse extension as a function of cloud asymmetry parameter for $\tau = 1.0$ and 4.0

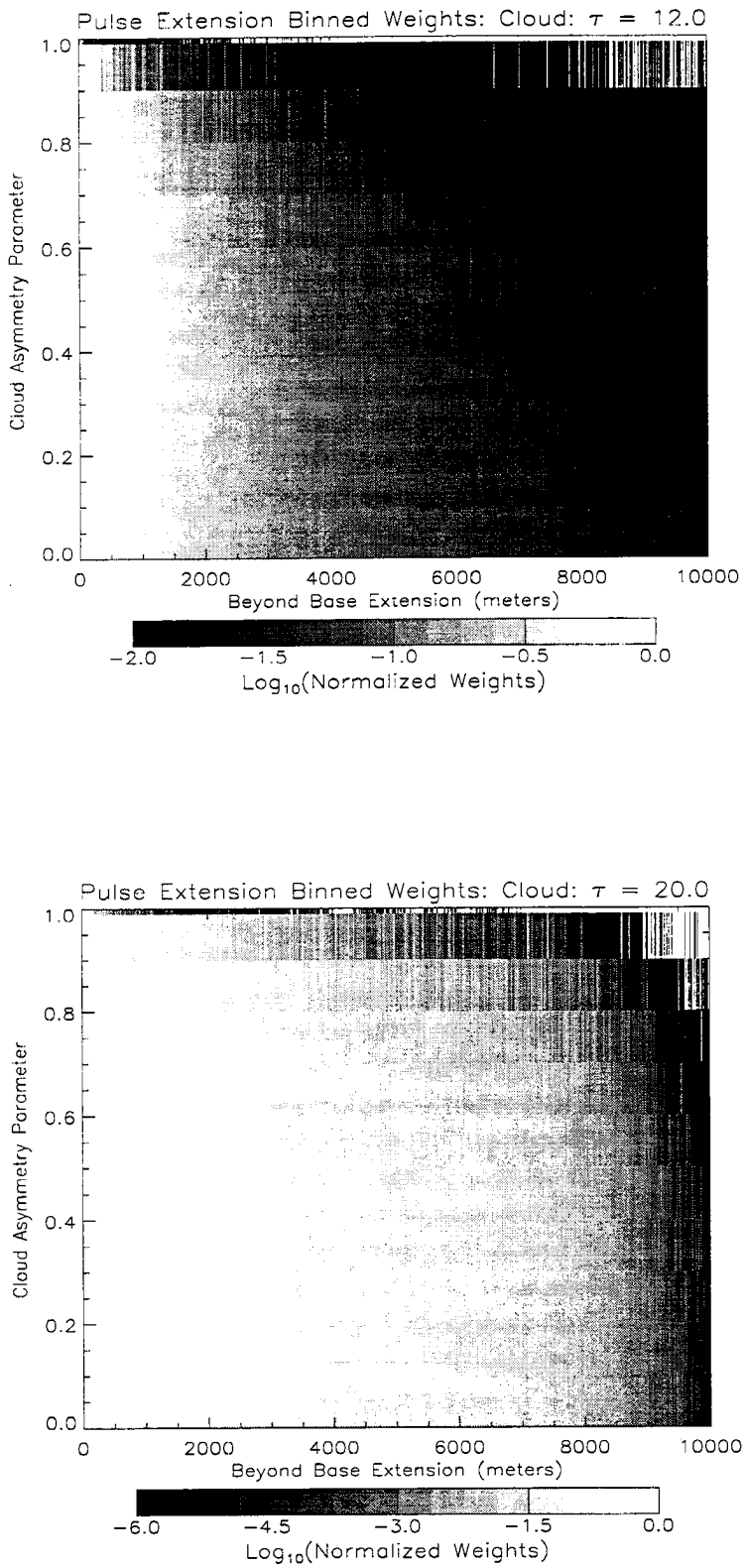

Figure 7.4: Pulse extension as a function of cloud asymmetry parameter for $\tau = 12.0$ and 20.0

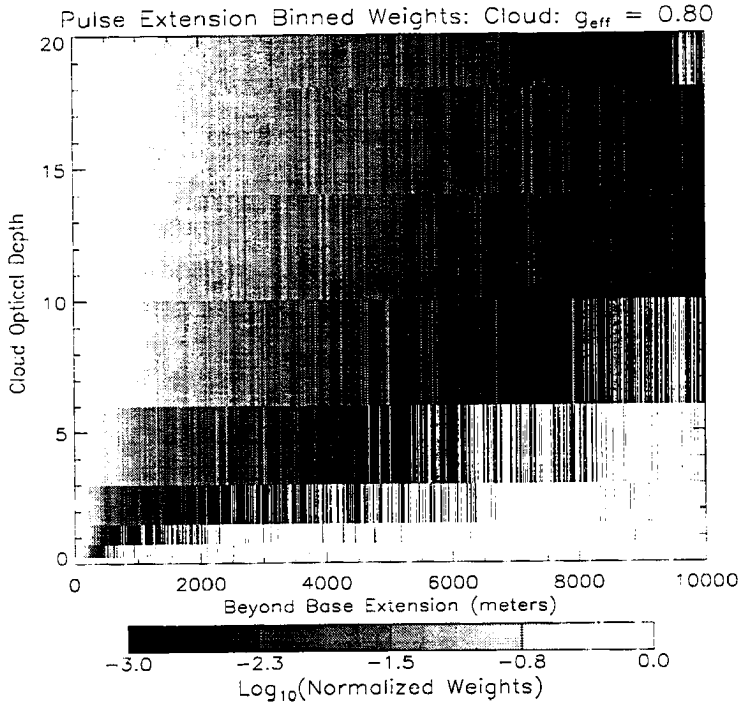

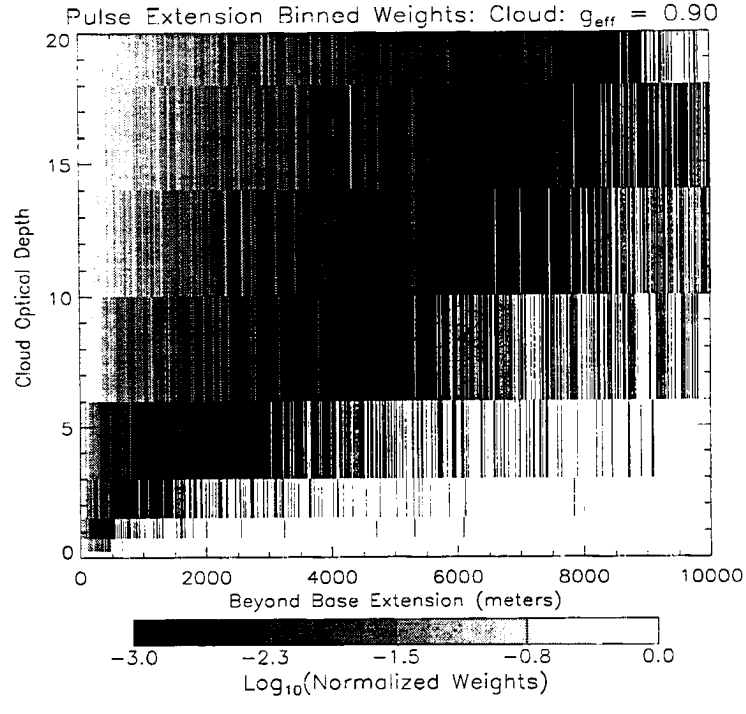

Figure 7.6: Pulse extension as a function of cloud optical depth for $g_{eff} = 0.80$ and 0.90

J) was then used to convert the return signal to the number of photons returned at below-cloud-base pulse extension distance D according to:

$$\begin{aligned} N_{sent} &= \frac{P_{lidar}}{h\nu_{532nm}} \\ N_{returned,D} &= N_{sent} \times \sum_{k=1}^{k=K} S_{k,D} \end{aligned} \tag{7.1}$$

where:

N_{sent} = Total number of photons sent in a single lidar shot

P_{lidar} = Output energy (J) of lidar beam

h = Planck's constant ($6.6262 \times 10^{-34}\ J\,s$)

ν = Frequency of 532nm light

$N_{returned,D}$ = Total number of photons returned to the detector having accumulated a geometric extension distance D

K = Maximum (truncated) scattering order considered

$S_{k,D}$ = Model returned-signal for scattering order k having accumulated a geometric extension distance D

The thresholding problem was then reduced to a simple choice of a detector-dependent minimum number of detectable photons. For this study, the minimum detectable signal was specified according to mimic that of the LITE sensors (see Chapter 6).

Using these guidelines for determining the physical pulse stretching distances, plots of these measurable quantities were made for a Henyey-Greenstein 1km thick cloud with the lidar oriented nadir at an altitude of 293km AGL with a detector FOV of 3.5mrad. Figure 7.7 illustrates the maximum below-cloud-base pulse stretching variation as a function of both cloud optical depth and effective asymmetry parameter. The detector FOV used to construct this plot was the standard (from LITE) 3.5mrad. Pulse extensions in excess of 8km occurred for the most

the cloud asymmetry parameter for fixed optical depths. (See Figures 7.3 - 7.4). The differences between isotropic ($g \approx 0.0$) and highly forward peaked ($g \approx 1.0$) are immediately apparent, with the stronger peaked phase functions exhibiting significantly lower pulse stretching effects (fewer multiple scattering events taking place in favor of transmission through the cloud or away from the detector FOV). As most scattering phase function asymmetry parameters found in nature lie in the range of 0.7 to 0.9, retrievals options based on these data focused on this range of results. In all cases but the largest optical depths, the isotropic scattering phase function produces the highest degrees of pulse stretching. The deeper cloud penetration of the high forward-peaked phase functions account for the relatively larger frequency of pulse extension events at the high optical depths.

Figures 7.5 - 7.6 examine the pulse extension event frequency in terms of a fixed asymmetry parameter and variable cloud optical depth (the corollary to Figures 7.3 - 7.4). It is clear from these plots that pulse stretching effects are also a strong function of the cloud optical depth, as expected. Extension distances increase with increasing τ, while decreasing with increasing g. From these plots, it was concluded that lidar pulse extensions exhibit sufficient sensitivity to cloud optical depth and scattering asymmetry to warrant further investigation into retrievability.

7.2.2 Physical Pulse Stretching

The notion of a "maximum pulse extension," as might be defined from raw lidar data (digitizer counts), was defined as the point when the below-cloud-base stretched signal strength falls below some pre-defined threshold (*eg* a signal-to-noise ratio specification). This was specified by arbitrarily defining a minimum detectable signal (an instrument-dependent quantity) and then truncating the extension signal accordingly. Because the lidar beam strength was normalized to unity, the Monte Carlo model returns therefore represented a fraction of this incident power. A straightforward de-normalization of this return based on the lidar's output energy (0.460

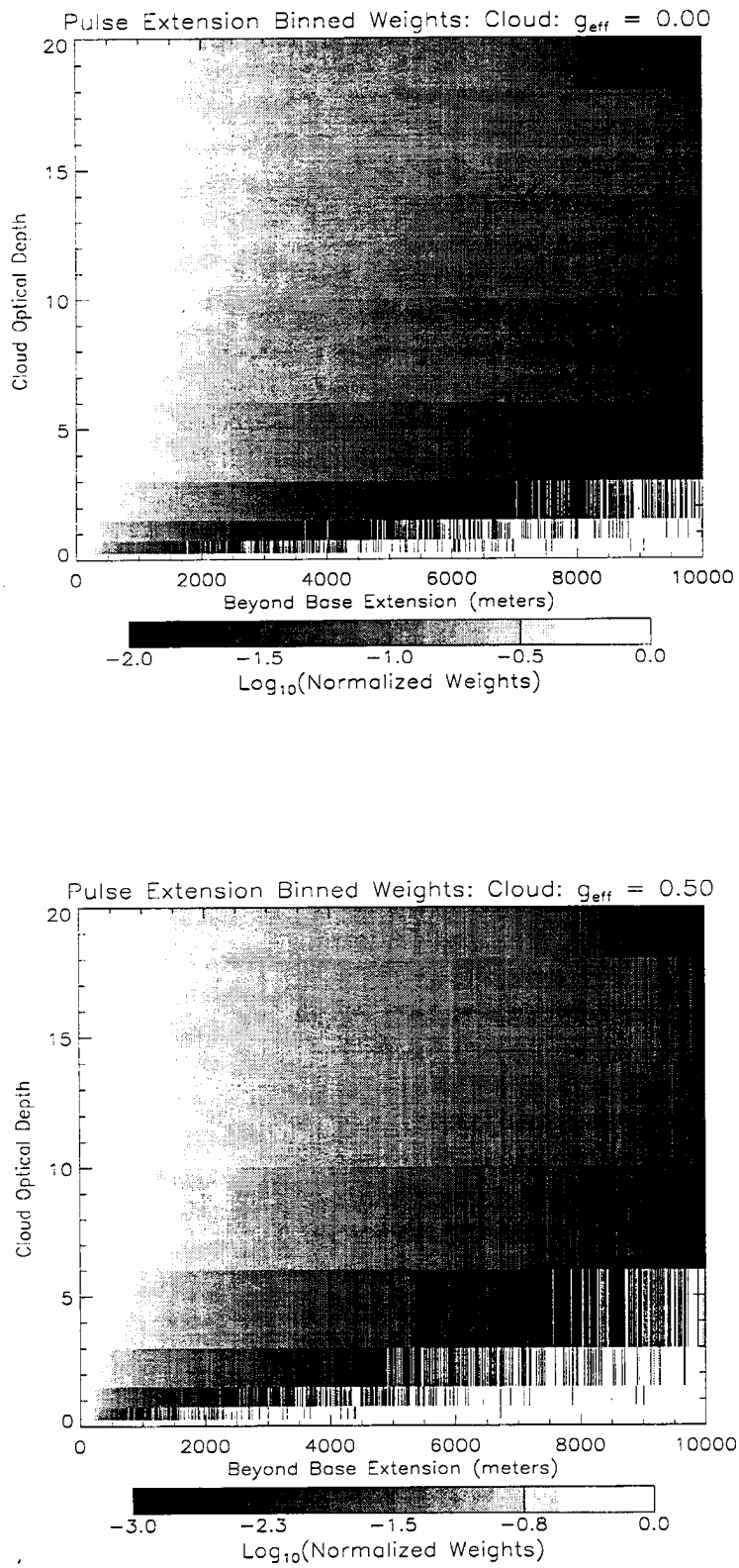

Figure 7.5: Pulse extension as a function of cloud optical depth for $g_{eff} = 0.0$ and 0.50

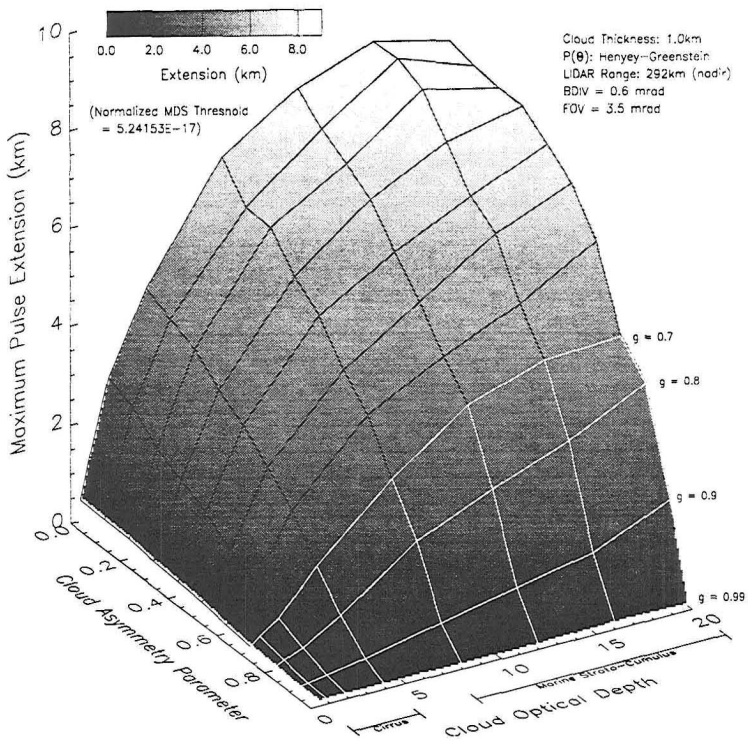

Figure 7.7: Maximum below-cloud-base pulse extensions as a function of cloud optical depth and asymmetry parameter (g_{eff})

isotropic phase functions ($g << 0.7$), while more typically-observed values ranging up to 4 km or 5 km were observed for the phase function asymmetry parameters most often found in nature ($g > 0.7$). The strongest dependencies on scattering phase function asymmetry were for $0.7 < g < 0.9$ at higher optical depths, while the extensions became less sensitive to cloud optical depth as $g \rightarrow 1.0$ (nearly complete forward scattering). Curves of iso-g representative of most "real-world" clouds were highlighted to indicate the expected physical range of pulse extensions observable in nature. These results are in reasonable agreement with the LITE data, which showed relatively little pulse stretching in the cirrus cloud formations (generally higher effective asymmetry parameters and lower optical depths as shown) com-

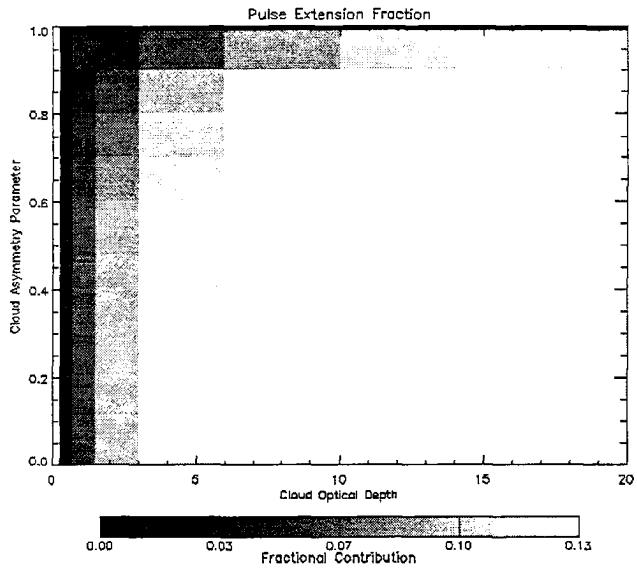

Figure 7.8: Fraction of total signal return attributed to below-cloud-base pulse extensions

pared with the lower marine strato-cumulus clouds (associated with relatively lower asymmetry parameters and higher cloud optical depths).

Given the true cloud base altitude (via independent measurements, sensing at wavelengths less susceptible to multiple scattering effects, or approximation from nearby, unstretched bases), the total accumulated signal associated with the pulse extensions may be obtained via integration. Figure 7.8 shows the fraction of the total signal return comprised of pulse extensions, again as a function of optical depth and asymmetry parameter. For some combinations of τ and g, the below-cloud-base (extended) signal accounts for over 10% of the total backscatter return power. Combining this information with Figure 7.7 indicates that as the forward scattering peak increases (and for decreasing cloud optical depth) the pulse extension signatures decrease in magnitude and intensity. The rate of this decrease becomes a strong function of g for $g > 0.70$.

7.2.3 Bulk Asymmetry Parameter Relationships

As was perhaps expected from the multiple-scattering studies described in the previous chapter, pulse stretching has been shown to be a rather strong function of the scattering phase function asymmetry, g, of the cloud medium. The double Henyey-Greenstein phase function, while insufficient to capture the details of true water or ice clouds, does well to characterize the bulk scattering properties of the medium. In addition to this analytical representation, pulse extension effects for the Deirmendjian C1 cloud (Mie) and Takano & Liou's ice crystal (Monte Carlo ray-tracing) functions were also computed. Because the physical pulse extensions are one-dimensional quantities, the additional details of a complex phase function will be mapped to a corresponding point in "bulk micro-physical space". While this may spell doom for any retrieval seeking to determine specific cloud particle geometries (granted, a lofty ambition to begin with), knowledge of the bulk cloud asymmetry parameter may still be useful for some applications. For example, it might provide a way of defining the phase of cloud particles (ice cloud scattering phase functions are very different from those of water clouds).

Figure 7.9 shows the marked differences in maximum pulse extensions as a function of three different Takano & Liou ice crystal phase functions. The cloud parameters and instrument geometry were unchanged from previous comparisons. Comparing the magnitudes of these extensions to the double Henyey-Greenstein results of Figure 7.7, it is evident that these ice crystal bulk asymmetry parameters fall over the range of approximately (0.84,0.90). To understand how the Monte Carlo model implemented the complex scattering phase functions in a bulk sense, choices of scattering angles (based on the (η, ψ) probability density function look-up tables described in Chapter 5) were averaged over all scattering events to obtain a "mean scattering angle" chosen by the model for a given scattering phase function. Plotted in Figure 7.10 are the results of this exercise for a variety of complex scattering phase functions (symbols) plotted along an analytical Henyey-Greenstein phase

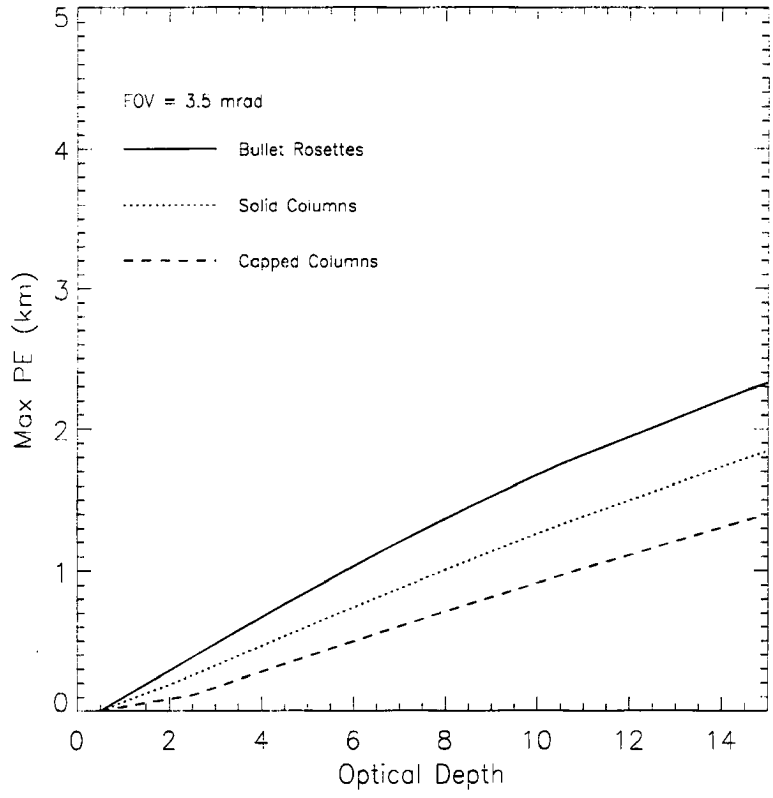

Figure 7.9: Beyond-cloud-base pulse extensions for selected Takano & Liou ray-tracing ice crystal phase functions

function curve. In the zoomed image (upper right corner), it is observed that all the strongly forward-peaked phase functions are nestled tightly over a region corresponding to effective asymmetry parameters spanning (0.83,0.91). The sensitivity to the asymmetry parameter is observed to also be a function of cloud optical depth.

7.2.4 Detector FOV Sensitivities

As shown in Chapter 6, expanding the detector field of view allows for an increasing number of photons to contribute from the diffusion-limited multiple scattering regime. In their studies of blue-green laser propagation through marine fog banks, Mooradian *et al* (1979) show that increasing the receiver field of view results in significant (tens of microseconds) pulse stretching, as well as a delay in the peak

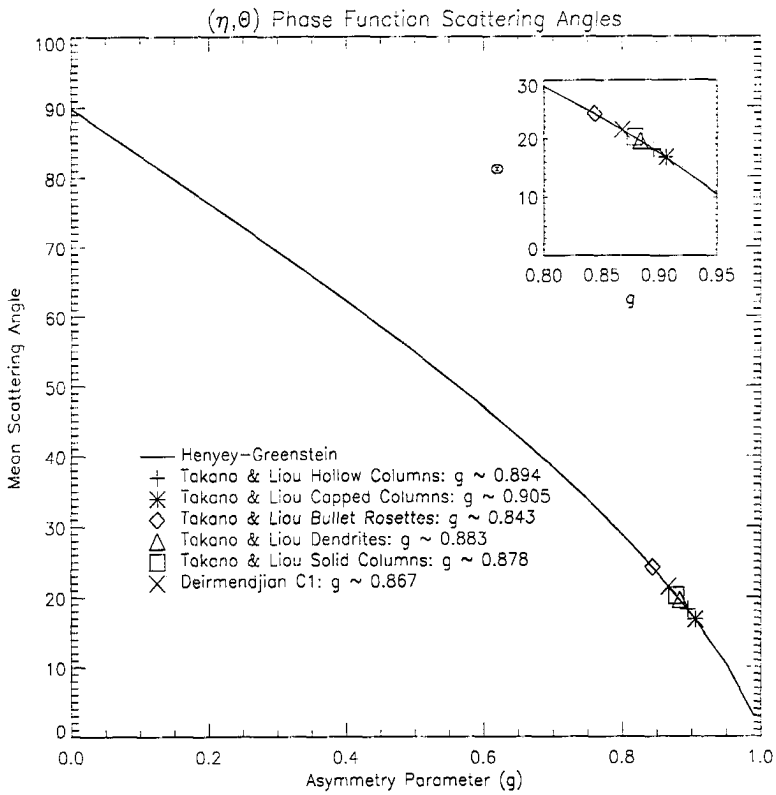

Figure 7.10: Monte Carlo-derived mean scattering angles for selected scattering phase function geometries

return signal. Considering the significant enhancement of multiply-scattered returns and resultant pulse stretching variations, the possibility of these results providing additional information to a retrieval is well founded.

Figure 7.11 provides an illustration of the enhanced pulse stretching effects resulting from an increase in the detector FOV. Again, the lidar instrument was placed at 292km above 1km thick, plane parallel clouds with scattering phase functions as shown. The detector FOV was allowed to vary between 2.0 and 28.0 mrad. Expanding the FOV beyond this value resulted in little change in the results. Extensions were observed to rapidly increase over the first several milli-radians of FOV increase, with less marked increases at higher FOV's . The pulse extensions increased with increasing detector FOV because radially-scattered photons (which possess longer

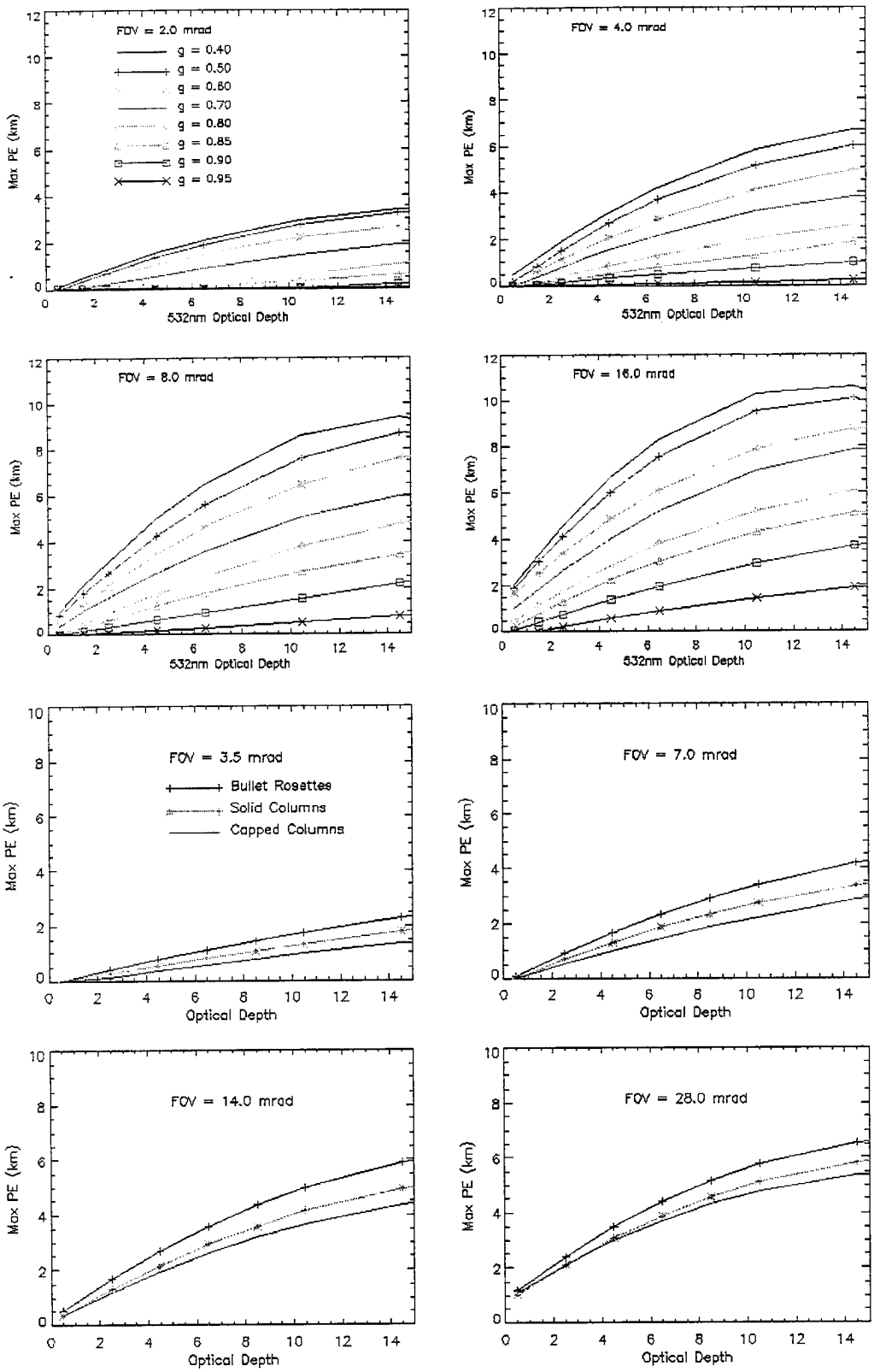

Figure 7.11: Beyond-cloud-base extensions as a function of cloud optical depth for varying detector FOV: Henyey-Greenstein (top) and ice crystal phase functions (bottom)

geometric distances associated with lower cloud extinction) have a better chance of being detected due to the larger FOV footprint. As the asymptotic limit of all available contributing photons in the diffusion-limited multiple scatter region is approached, sensitivity of pulse extensions to incremental changes in FOV diminish in turn.

The changes in the below-cloud-base pulse extension return signal with change in the detector field of view are shown in Figure 7.12 for optical depths ranging from 0.5 to 36. For smaller optical depths the signal associated with the pulse extensions is smaller, but increasing the detector FOV continues to capture more radially-scattered photons (as indicated by the relatively slow decrease of the first derivatives). For larger optical depths, the outer-fringes of the diffusion region are constricted with respect to the direct beam axis. Figure 7.13 shows the change in total signal return as a function of optical depth for increasing detector fields of view. For the lidar geometry of this problem and scattering asymmetries of the 1km thick cloud, increasing the detector field of view by a factor of 4 resulted over an order of magnitude increase in return was achieved at all optical depths. Provided an instrument with variable FOV capability, observations of

$$d(PE)/d(FOV)$$

for the same cloud scene may provide additional information on the cloud asymmetry properties or the optical depth.

7.2.5 Cloud Geometric Thickness

Photon free path travel distances within scattering and absorbing media are governed not by the geometric thickness of the medium but by the probability of the photons encountering targets. For a fixed value of optical depth, increasing the cloud's vertical thickness results in a lowering of the extinction coefficient. Photons will therefore travel larger distances between scattering events. Applying this to a

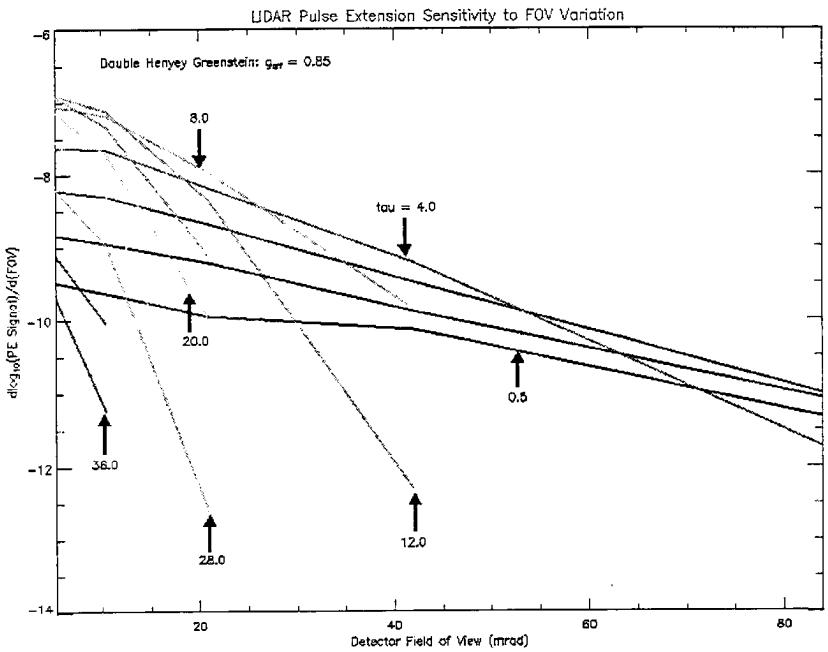

Figure 7.12: Pulse extension signal sensitivity to changes in the detector FOV for a DHG cloud, $g_{eff} = 0.85$

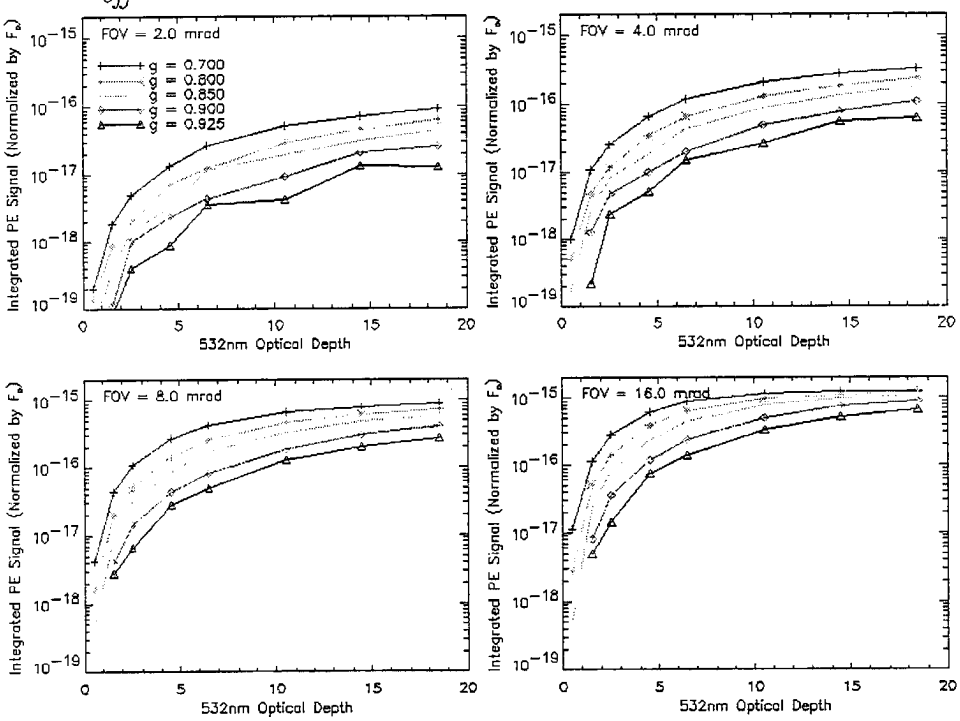

Figure 7.13: Integrated pulse extension signal as a function of cloud optical depth and detector field of view

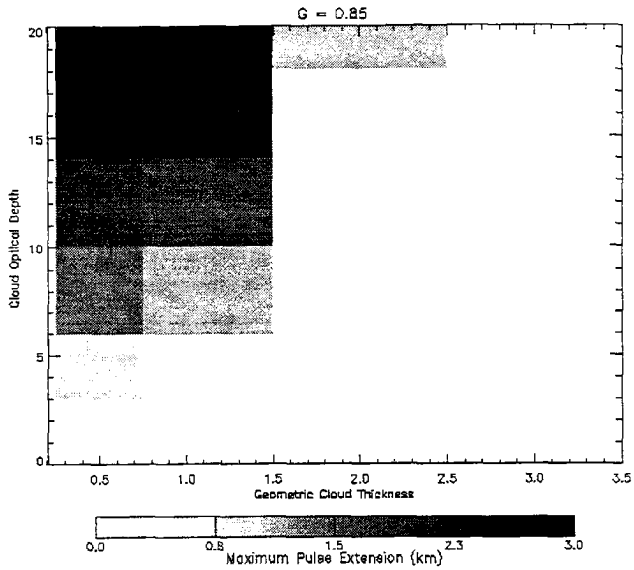

Figure 7.14: Maximum pulse extension measured as a function of τ and cloud geometric thickness for $g = 0.85$

lidar with fixed detector geometry, vertically stretching a cloud (while maintaining its optical depth as constant) will result in fewer multiply-scattered events occurring within the confines of the detector cone. Translated to pulse extensions, fewer photons will possess significant accumulated travel distances, and pulse extension features should decrease.

As Figure 7.14 demonstrates, pulse extensions drop off with increasing cloud geometric thickness and fixed cloud optical depth. Plots for other scattering asymmetry parameters showed similar relationships. It may also be inferred that the relationship between pulse extension and cloud extinction is nonlinear. The maximum pulse extension for a 2km-thick cloud with $\tau = 16.0$ (corresponding to σ_{ext} = 8.0/km corresponded to a 1km-thick cloud having $\tau = 4.0$ ($\sigma_{ext} = 4.0$/km), and pulse extensions were altogether negligible for the 3.0km thick cloud. This is not an implication that multiple scattering effects are innately lower in geometrically

thicker media, but what the fraction of these multiply-scattered events which occur within the detector field of view is. It may therefore be concluded that for a fixed lidar viewing geometry, thicker cloud media require higher extinction coefficients to produce equivalent pulse extension distances.

7.3 Physical Interpretations

Sharply forward-peaked scattering media tend to maintain a significant amount of the energy in the vicinity (and original direction of travel) of the direct beam. Adding a peak at the backscattering lobe and minimizing the probability of off-axis scatter means that photons will have the tendency of either transmitting straight down or reflecting straight back. Because it is even less likely that photons will scatter straight up and down *several* times in succession (due to the relative weakness of the backscattering lobe), the returning photons will tend to be of lower scattering order. To gain significant added distance to a photon's random walk, a large number of scattering events is required. Furthermore, without a strong radial scattering component, it is difficult for photons to achieve these relatively large distances. As a result, phase functions with strong forward and backward scattering lobes should not exhibit the dramatic pulse extensions that more isotropic phase functions do. In the Monte Carlo simulations, it was clearly evident that scattering phase functions having bulk asymmetry parameters closer to unity exhibited lower degrees of pulse extension.

Figure 7.16 shows a comparison between the Deirmendjian C1 water cloud and the capped column ice crystal ray-tracing phase function from Takano & Liou (1995). Note that the forward peak on the ice phase function is several orders of magnitude greater than that of the C1 cloud, indicating a further reduction in the pulse extension phenomenon for ice clouds in comparison to that of water clouds. Also, the larger particles present in cirrus clouds manifest in lower short-wave optical

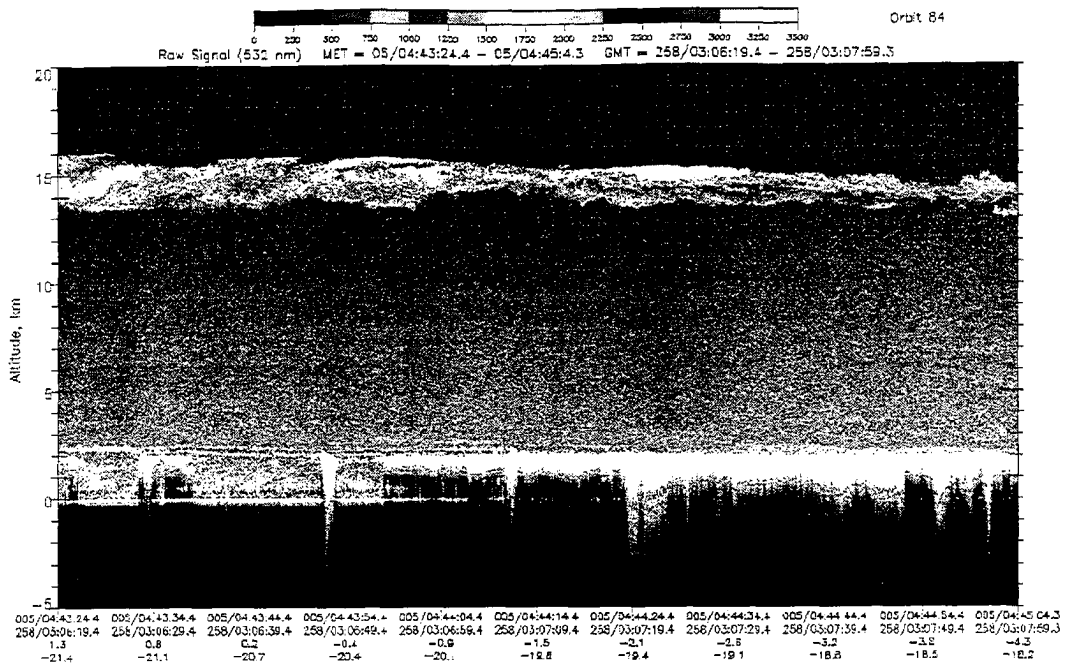

Figure 7.15: Raw Count Return from Orbit 084 showing pulse extensions effects in lower level clouds but not in 15km cirrus

depths. Combining these points with the generalized observation that cirrus clouds are, in general, geometrically thinner structures to begin with, it may be expected that cirrus clouds would exhibit markedly lower pulse extension effects as compared with many lower tropospheric cloud structures.

Figure 7.15 is an example of significant pulse extension effects occurring in marine stratus deck (at 2km), while a cirrus layer (at 15km) does not appear to possess these features even in the most tenuous regions. Also noteworthy is that the deepest observed pulse extensions (~ -4 km) do not appear to correlate with the tenuous regions of the upper cirrus deck. If MS effects were strong in the cirrus, one would expect correspondingly stronger pulse stretching effects in layers directly beneath them. There exist cases in the LITE imagery where the detector field of view was intentionally switched between several apertures as described in Chapter 5. In one such experiment, Discovery flew over a cirrus deck while varying the field of view between 3.5mrad and an annulus which only allowed returns between

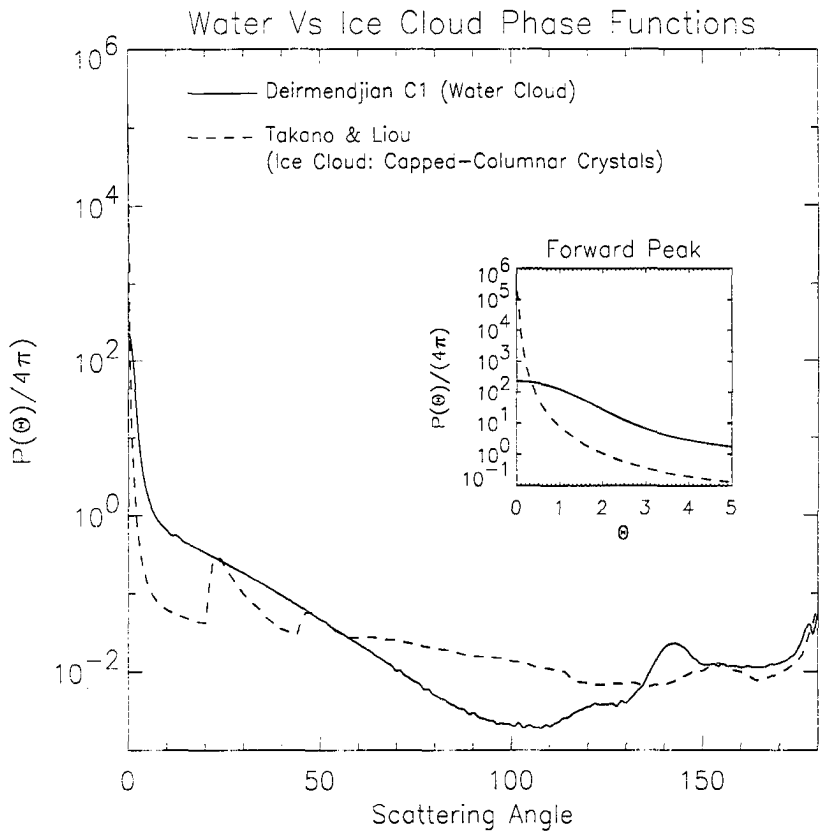

Figure 7.16: Comparison of Deirmendjian C1 to Takano & Liou's ray-tracing results for a "Capped Column" ice crystal geometry.

1.1mrad and 3.5mrad (multiple scattering only). During the times of the latter test, the cirrus cloud disappeared completely from the signal return; indicating that significant radial excursions by multiply-scattered photons were not contributing to the cirrus cloud signal. It follows from the developments of Chapter 6 that pulse stretching features should also be reduced for this case.

7.4 Higher-Order Approximations and Complex Cloud Structures

This study focused primarily on the behavior of pulse extensions within idealized, plane-parallel media. With the exception of the quasi-perennial marine stratocumulus decks located off Western coasts of North America, South America, and

Africa, such scenarios are seldom observed in nature (and even strato-cumulus decks cannot be considered as perfectly stratified formations). Nevertheless, pulse stretching signatures are found in a great variety of cloud structures, including multiple-layered clouds. Although some real-world scattering phase function geometries were introduced to the plane parallel cases, the approximation to real-world clouds remains insufficient. An attempt was made here to address some of these higher-order issues in the pulse stretching problem as ground-work for future investigations.

A brief exploration of pulse extension behavior in non-uniform media was carried out using a three-dimensional Monte Carlo lidar model. A limitation of this model was that scattering phase function properties were required to be held invariant throughout the medium; prohibiting the modeling of (for example) mixed-phase cloud layer scenes. The model did accommodate for variation of cloud optical thickness at arbitrary horizontal and vertical resolution, and multiple cloud layers with an optional reflecting lower boundary. Several cloud geometries were studied which had either an irregular surface texture or inhomogeneous vertical structure in optical depth. In particular, cloud geometries possessing horizontal inhomogeneity, vertical inhomogeneity, and multiple-layered cloud systems were investigated.

7.4.1 Horizontally Inhomogeneous Media

Most all naturally occurring cloud structures possess horizontal inhomogeneities on the spatial scales of interest to the lidar in-space problem. Depending on the optical and geometric variation scales of these features with respect to the instrument geometry, the divergence of multiple scattering behavior from the simple stratified cloud case becomes significant. To examine the effect of a non-uniform cloud-top surface, a geometry was chosen according to Figure 7.17. The cloud extinction was taken to be homogeneous throughout ($\sigma_{ext} = 1.0$/km), with a two-kilometer-wide "pit" of variable depth at the top/center of the cloud. A periodic boundary condition was imposed such that the $6 \times 6 \times 3$km block repeated itself at the boundaries (in

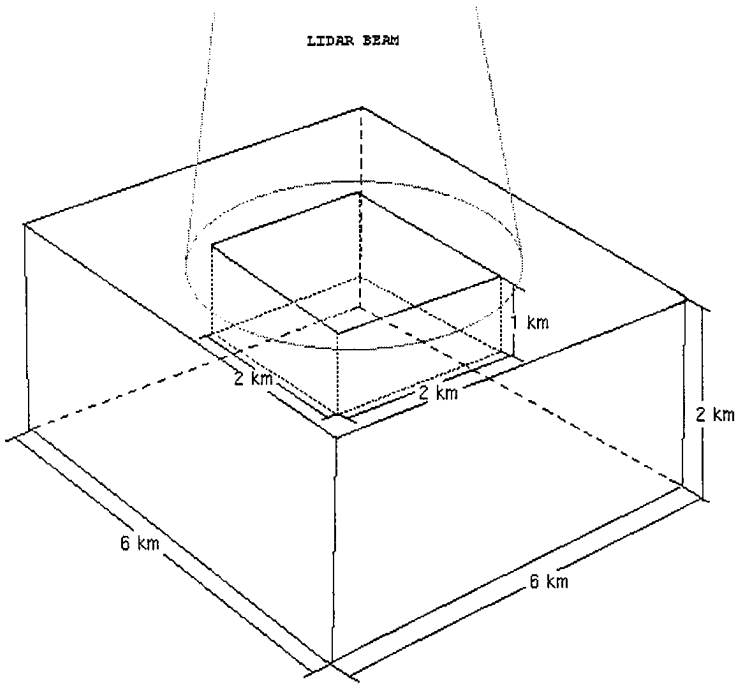

Figure 7.17: Cloud geometry used for 3-D pulse stretching study: modeled cloud hole in center

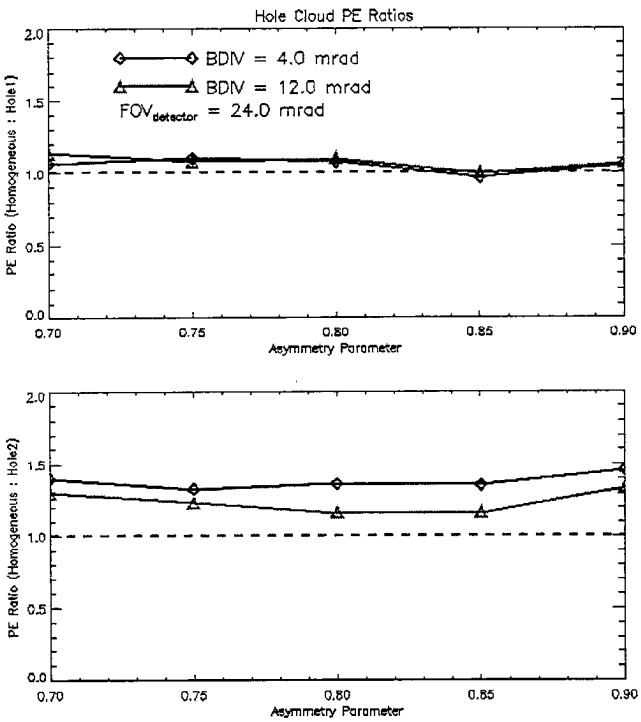

Figure 7.18: Pulse extension ratio results for the modeled cloud hole geometry

order to model a more realistic marine strato-cumulus cloud deck). Because the detector field of view was contained completely within a single cube, and a radially-scattered photon's chance of re-entering this field of view after having scattered out of it approaches negligible significance, the periodic boundary did not affect the model results. The cloud was illuminated by a nadir-pointing lidar beam at a range of 292km, with the direct beam axis incident on the central void in the cloud. The laser beam divergence was modified such that one setting featured the entire beam within the hole and another case where the hole was smaller than the laser beam footprint (a BDIV of 4.0 mrad produced a spot radius of r = 0.58km, and r=1.75km for BDIV = 12.0 mrad). Pulse extensions were re-computed for each case and compared with those computed for a stratified cloud of identical extinction.

The comparisons are given in Figure 7.18 for the cases described above. "Hole1" refers to a cloud having a $2 \times 2 \times 1$km void on its top surface, and "Hole2" is for a $2 \times 2 \times 2$km void (a 1km deeper hole). "BDIV" refers to the laser beam divergence selected, and the detector field of view was held at 24.0 mrad. Some points of interest in these figures are:

- For both cloud geometries, the pulse extensions measured for the homogeneous case were greater than or equal to those of the cloud-hole cases.
- In the Hole2 cloud, there was a marked difference between the two BDIV cases, but little difference for the Hole1 cloud.
- The ratios indicated signs of increasing at higher g for the Hole2 cloud (less noticeable in the Hole1 cloud).

Noting the geometry of the problem, explanation for the first observation is straightforward. The lidar beam was incident on the center of the hole, meaning that the vertical optical thickness from the piercing point to the cloud base along the direct beam was relatively smaller than the homogeneous cloud. Depending

on the depth of the cloud hole, this effect was diminished or exacerbated. but in all cases the horizontally-stratified cloud was characterized by higher photon path-length-distributions. In the Hole1 case, this effect was small, but as the hole's depth was increased the differences in pulse extension magnitude also increased (as an effectively thinner cloud was encountered). The differences between the two laser beam divergences also became apparent. Because the BDIV = 12.0 mrad case projected a laser beam footprint larger than the hole in the cloud, more photons encountered additional scattering events which would be otherwise missed if all the direct beam photons had traveled into the hole. For larger asymmetry parameters. the ratios began to increase (see the Hole2 cloud case). This is explainable by noting that, for higher forward-scattering media, the probability of escape through the lower boundary of the cloud increases dramatically (a portion of the distribution will transmit directly through the cloud without scattering at all). Due to the decreased optical thickness (by virtue of the void in the cloud) compared to the homogeneous cloud, this factor becomes more significant as g increases. More photons will escape the lower boundary and fewer accumulate significant geometric paths; resulting in the larger homogeneous-to-inhomogeneous pulse extension ratio values observed.

These results indicated that clouds with horizontal inhomogeneities of spatial extent on the order of the laser footprint should exhibit notable pulse extension differences with respect to an equivalent homogeneous medium. The horizontal resolution in LITE was on the order of 0.74km and the laser beam and detector footprint radii were approximately 0.18km and 0.90km, respectively. Because cloud horizontal variability occurs at these and smaller scales (depending largely on cloud type) in Nature, it probably cannot be overlooked in the modeling of most cloud fields. The horizontal variability features which occur on scales smaller than the laser beam divergence, on the other hand, will tend to be smoothed out with respect to the broader-scale features of the cloud.

7.4.2 Vertically Inhomogeneous Media

Another important characteristic of real clouds is their optical property variability in the vertical. Stephens and Platt (1987) examine variations in liquid water content (LWC), droplet concentration (N_o) and effective radius (r_e) for a variety of stratocumulus and cumulus cloud fields. They find a large variation in the extinction coefficient, but a more uniform asymmetry parameter for the clouds sampled. Figure 7.20 illustrates pulse stretching behaviors for a cloud of variable optical depth in the vertical (see Figure 7.19 for geometry). For this comparison, two clouds were used, all having a uniform cloud asymmetry parameter throughout. The "top-weighted" cloud distributed the bulk of its optical depth over the top layers (referring to Figure 7.19, $\tau_1 - \tau_4 = (2.5, 2.0, 1.0, 0.5)$, and the optical depth values were reversed for the "bottom-weighted" cloud case. As the benchmark, a vertically uniform (in extinction) cloud was used. These clouds were all placed at the same level in the atmosphere and illuminated from above by a variable FOV lidar instrument. In this case, examination of relative differences in pulse extension rather than absolute values provided for a more meaningful discussion of the variability. For the ratio results of Figure 7.20, the following observations were made:

- The ratio results indicated a general decrease in pulse extensions for the top-weighted case and an increase for the bottom-weighted case.

- The largest ratio excursions were observed for the smallest detector FOV, with less dramatic differences for increasing FOV.

These findings may be explained physically by gathering the multiple scattering behaviors observed in Chapter 6. Focusing on the more forward-peaked phase functions (asymmetry parameter values ≥ 0.80) for simplicity, several points can be made for the two cases:

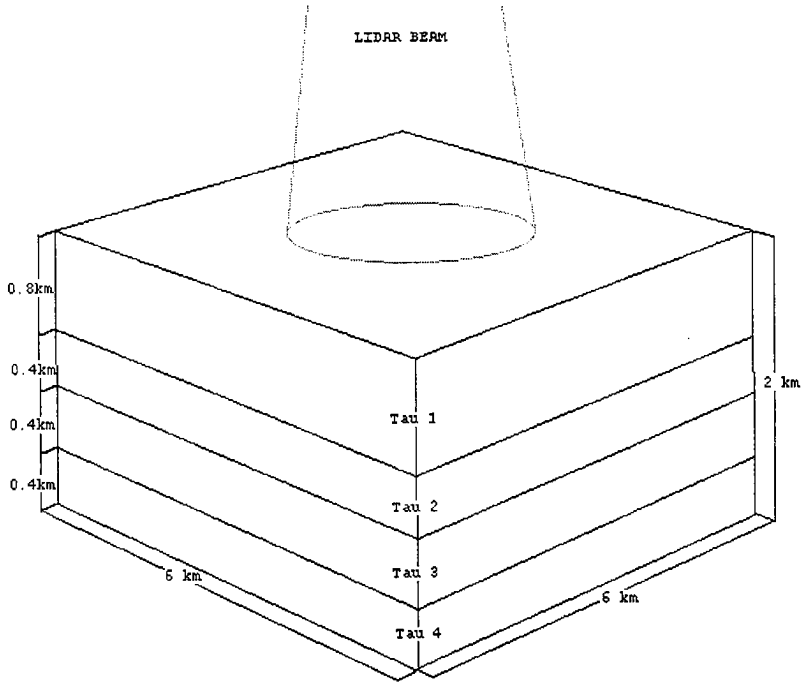

Figure 7.19: Modeled cloud having vertical inhomogeneity

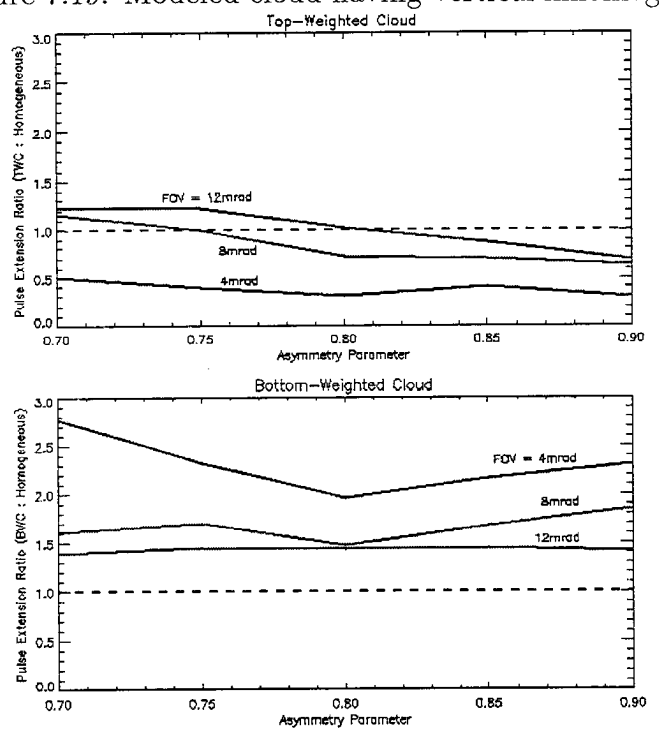

Figure 7.20: Pulse extension ratio results for the vertically inhomogeneous cloud geometry.

1. For the top-weighted cloud. photons immediately encounter several scattering events at short geometric travel distances and then optically thinner regions below.

2. Conversely, photons impinging the upper boundary of the bottom-weighted cloud travel greater distances between scattering events before reaching the optically thick region at the base of the cloud.

3. Photons which have made their way through the thick upper boundary of the top-weighted cloud (and into regimes where appreciable geometric path lengths may be accumulated) tend to transmit out of the cloud base rather than back up through the tenuous layers above. (Re-transmissions back through the upper layers are lower, and are thereby weighted down in probability).

4. Photons in the bottom-weighted cloud have easier transmissions back to the detector (located above the cloud). Many photons will gather significant multiple scatter geometric distances and therefore exit the upper boundary with relatively greater travel distances (and with greater probability of contribution, since upward transmission is higher).

5. As the detector field of view is increased, pulse extensions for both cloud fields approach the homogeneous case results. The sensitivity to FOV is stronger for the bottom-weighted cloud since there are more photons traveling a greater radial distances in this scenario.

6. In both cloud cases, pulse stretching effects are maximized in the region of higher extinction. Because the measurand for this excercise was *below cloud base* pulse extension, the stretching effects of the top-weighted case should have a lower contribution than those of the bottom-weighted case (whose pulse stretching signatures will more-often occur below the true cloud base by virtue of their initial proximity to it.)

The conclusions drawn from these arguments were that clouds with top-heavy optical thickness distributions should exhibit less significant pulse extension effects than a homogeneous distribution having the same integrated vertical optical depth, while clouds with the opposite distribution will show enhanced effects.

7.4.3 Multiple-Layered Clouds

To investigate the behavior of pulse extensions in profiles of multiple-layered clouds, the simple case of two uniform cloud layers each having geometric depths of 1km and $\sigma_{ext} = 2.0/\text{km}$ was investigated. The two clouds were vertically stacked with variable distances of separation ranging from 0km to 4km. Ratios of the resultant pulse extension measurements (with respect to the 0km separation case) were recorded for the lower cloud layer. Figure 7.22 shows the ratio between pulse extensions observed for the unseparated cloud (a uniform cloud having geometric vertical distance of 2km and $\tau = 4.0$) to cloud layer separations of 1km and 4km, respectively. The extension ratios were plotted as a function of scattering asymmetry parameter and for two different detector fields of view. For this figure, the following observations were made:

- The ratios were observed to exceed unity for all combinations of detector FOV and asymmetry parameter value; indicating that the unseparated cloud had pulse extensions which always exceed the separated cloud cases.
- The ratios increased with increasing cloud layer separation.
- The ratios decreased towards unity for increasing cloud asymmetry parameter and increasing detector FOV.

All of the above points may be explained by visualizing the physical scattering processes taking place, while keeping in mind the finite viewing geometry of the detector. As two cloud layers are separated, the downward trajectory of photons

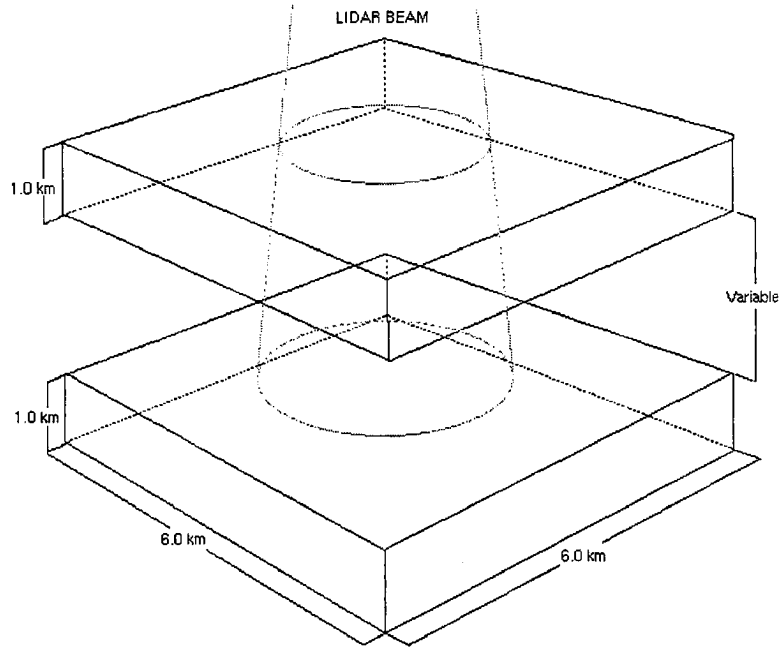

Figure 7.21: Modeled multiple-layered cloud profile

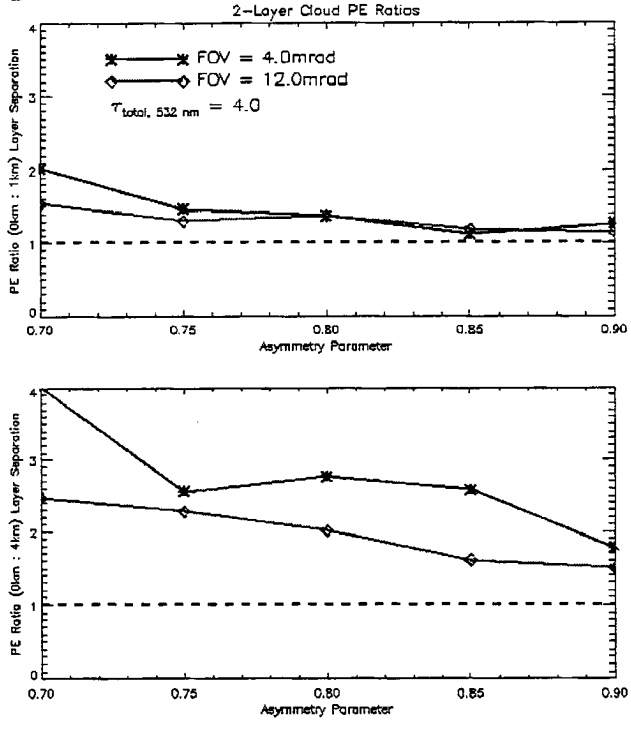

Figure 7.22: Pulse extension ratio results for the multiple-layer cloud study.

exiting the base of the upper-layer (either still along the direct-beam, or a direction determined by their last scattering event) become more critical. If the direction of a scattered photon is far enough askew to the direct beam, it will travel a radial distance placing it outside of the detector field of view projected upon the top boundary of the lower cloud layer. Thus, multiply-scattered photons which exit the base of the upper layer will have a smaller chance of impinging the lower layer at a point that is still visible by the system. This is a minor consideration for small cloud separations, but becomes a significant factor for larger separations (when even a small divergence from the direct beam trajectory will lead to a projection the photon outside of the detector FOV at the lower cloud boundary). In this case, the majority of photons which do contribute to the lower cloud layer's pulse extension signal are ones that did *not* undergo significant off-axis scatter in the upper layer; their contribution to the pulse extension signal upon entry into the lower layer is minimal. The resultant pulse extension for the lower layer reduces to a function of the lower layer's optical properties alone. Because a completely analogous detector-geometry constraint is placed upon reflected photons from the lower layer as they pass through the upper cloud layer, it is argued that the majority of *detected* photons attributed to the lower cloud layer underwent minimal radial scattering in the upper layer. As was shown in the model results, pulse extension distances tended to increase with increasing optical thickness. Hence, the observed ratios exceeded unity in both plots of Figure 7.22.

The values and trends in the ratio results quantify the above discussion. Larger ratios were observed for the 4km cloud separation compared to that of the 1km separation, as the pulse extension of the 0km separated cloud (effectively, a $\tau = 4.0$ cloud) was much greater than the 4km separation (effectively, a $\tau = 2.0$ cloud). As the detector field of view was increased the ratio value decreased, as more of the multiply-scattered photons projected upon the lower cloud boundary remained

within the detector FOV. The observed decrease in ratio for higher values of cloud asymmetry parameter (g) also testifies to this claim, since a larger distribution of the photons impinging the top cloud remain along their original (direct beam) trajectories. Emerging from the lower boundary of the top cloud at smaller off-axis angles, they will have a greater opportunity of contributing to the lower cloud's observed multiple scattering events even if they did undergo some scattering events in the top cloud.

The conclusion drawn from this case was that, within the constraints of the detector FOV, a cloud layer separation distance will exist such that pulse stretching effects between the two layers (in an interactive sense) are effectively independent.

7.5 Summary

Modeled below-cloud-base pulse extensions were presented as functions of the driving optical properties of the scattering media; namely, the cloud extinction and scattering asymmetry parameter. There was also strong evidence of modeled pulse extension sensitivity to the detector FOV (which governs the amount of multiply-scattered photons able to contribute to the signal return). While the modeled results were for a plane parallel homogeneous cloud medium, case studies involving less-idealized cloud media revealed that the relative differences in pulse extensions between these simple cases and those of more detailed cloud geometries were not negligible. This suggests that some *a priori* information about the cloud vertical structure may be needed to adequately model pulse extensions. This information will likely be best provided by an independent measurement at longer wavelengths that are not as susceptible to the pulse stretching effects.

Chapter 8

ADDRESSING THE INVERSE PROBLEM

The primary goal of this study is to determine if the variabilities observed in lidar pulse extensions can somehow map to a unique set of cloud optical properties, and as such, possess uniquely invertible solutions (given sufficient information about the extensions such that only one set of conditions may satisfy the criterion, deduce the required cloud optical properties). In order to back out solutions to the inverse problem unambiguously, several uncorrelated measurements of the pulse extension properties are needed. The physical length of a given pulse extension (determined by some minimum detectable signal threshold defined by the hardware) was shown to be, in and of itself, insufficient to identify information about both cloud optical depth and scattering phase function properties (see Figure 7.7) uniquely. Consequently, several additional pulse stretching measurements must be performed on the medium which provide independent information about their behavior. As a general rule of thumb in retrieval theory, the more independent measurements available the better. The measurements investigated herein were comprised of:

- The physical pulse extension distance (Requires an *a priori* knowledge of true cloud base height).

- The signal strength of the pulse extension return (Requires cloud base height knowledge and an integration of the signal return from cloud base to MDS threshold.)

- The variability of the above properties with Detector FOV (Requires a variable FOV instrument).

This chapter gathers the multiple-scattering and pulse-stretching information presented in chapters 6 and 7 in the interest of identifying cloud property retrieval approaches using pulse stretching information, and concludes with suggestions toward a verification of these findings by means of a detailed field experiment, and possible applications of these data to enhancing existing retrieval approaches.

8.1 What Can Potentially Be Retrieved?

Chapter 7 showed that pulse stretching is a strong function both of cloud optical depth and asymmetry parameter. Keeping to the simple case of a plane parallel, vertically homogeneous cloud medium, it is reasonable to ask the question "can a collection of pulse extension measurement data be used to unambiguously retrieve these parameters?". As was illustrated in Figure 7.7 in Chapter 7, an infinite number of (τ, g) solutions exist simultaneously for any single pulse extension measurement. In addition to the physical pulse extension distance measurement, the change in this quantity as a function of changing the detector field of view and the integrated pulse extension signal strength represent measurable quantities which may be able to provide the additional information needed to convert the ill-posed problem into a more tractable one.

8.1.1 Single Parameter Retrieval

The infinite locus of solutions observed in Figure 7.7 may be reduced to a single solution, provided that one of the parameters (τ, or g) is constrained *a priori*.

While there currently exist few reliable methods for obtaining a value of the cloud asymmetry parameter (a particle size distribution usually must first be assumed), there do exist means of estimating the cloud optical depth. This can be achieved with either passive or active sensors (and may be derivable from techniques using the lidar itself). Constraining the optical depth and measuring the pulse extension provides an unambiguous estimate of the cloud asymmetry parameter. Inversion techniques for cloud extinction exist which make use of theoretical molecular returns immediately above and below the cloud boundaries (the "slope method"). In his investigations of lidar inversion techniques, Klett (1981) develops a simple yet stable analytical method for extracting information about the attenuation and backscatter coefficients in inhomogeneous atmospheric media from the return signal of monostatic, single-wavelength lidar systems. The method is less sensitive to signal noise and approximation of backscatter-to-extinction ratios. The applicability of this method to clouds exhibiting marked pulse stretching effects has not been explored here, but if a lidar measurement can be made at a small enough detector FOV such that pulse extensions are not dominant this method might still be applicable to this problem.

8.1.2 Multiple Parameter Retrieval

Aside from constraining one of the parameters it might also be possible to simultaneously retrieve them both, provided that measurements are available which can capture quasi-orthogonal relationships. That is, variations in optical depth being relatively more sensitive to one kind of measurement and variations in the asymmetry parameter being more sensitive to another. If such a measurement combination exists, then a retrieval grid may be constructed which is capable of simultaneously and unambiguously (over some range of the measurements) mapping out a pair of measurable quantities to a (τ, g) pair of cloud optical parameters; making for a more autonomous retrieval algorithm.

Several measurement-combinations were combined in an attempt to obtain a two-parameter retrieval grid. The "measurable quantities" available from the model were the minimum-detectable-signal (MDS) thresholded maximum pulse extension values for several detector fields of view, the change in these quantities as a function of change in the detector field of view, and the total integrated signal return of the extension (from true cloud base downward, normalized by the incident beam power). The integrated signal return was obtained by accumulating the contributions to the pulse extension signal over all bins ranging from the cloud base to the minimum detectable signal threshold. The signal values represent a fraction of the incident power, normalized in the Monte Carlo model to unity. It was found that the modeled integrated signal return provided some limited independent information about the retrieval parameters, and preliminary retrieval grids for some measurement combinations were constructed. Because these returns were modeled for a highly simplified cloud and represent a hardware-dependent quantity, care should be exercised not to interpret the integrated signal returns (and hence the resultant retrieval grids shown) as having immediate operational value.

The data set used to construct the retrieval grids is as follows:

τ	0.5-19.5 at increments of 1.0
g	0.70-0.95 at increments of 0.025
FOV	2, 4, 8, 16, 24 mrad

For simplicity, a Henyey-Greenstein phase function was used in a 1km-thick plane parallel cloud medium. As before, the lidar instrument was oriented nadir to the stratified cloud at a range of 292.0 kilometers. Monte Carlo simulations were run for 0.5×10^6 photons and a scattering order truncation of $K = 200$.

Figures 8.1 - 8.2 are retrieval grids constructed from maximum pulse extension (at various detector fields of view) and integrated pulse extension signal information. While the curves denoting lines of iso-τ (dashed) and iso-g (solid) were not purely orthogonal (which would mean that each parameter was sensitive to only one of

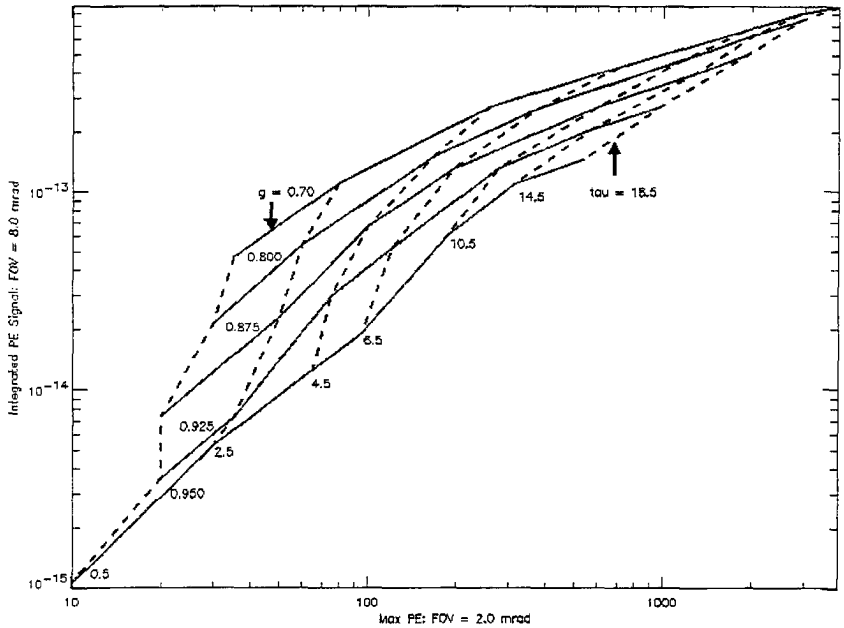

Figure 8.1: A two-parameter retrieval grid example using the integrated pulse extension signal and maximum pulse extension distance. (See text for details)

the measurements and completely insensitive to the other), there appeared to be sufficient independent information to map the measurements to a distinct (τ, g) pair. The highest sensitivities in this example were for $g > 0.70$ and $\tau < 15$ (beyond these limits variability in the grid became small or even ambiguous). The lowest values of integrated pulse extension signal shown were at least two orders of magnitude greater than the specified MDS for the hypothetical instrument, indicating that such information was well above the noise and represented a measurable discriminating parameter for the retrieval grid.

Examination of Figure 8.1 leads to the observation that the integrated signal returns were somewhat more sensitive to changes in the cloud asymmetry parameter, especially at lower values of τ, while the maximum below-cloud-base pulse extension values were more sensitive to changes in the cloud optical depth, especially at lower values of g. The first observation simply states that, for optically thin clouds, the

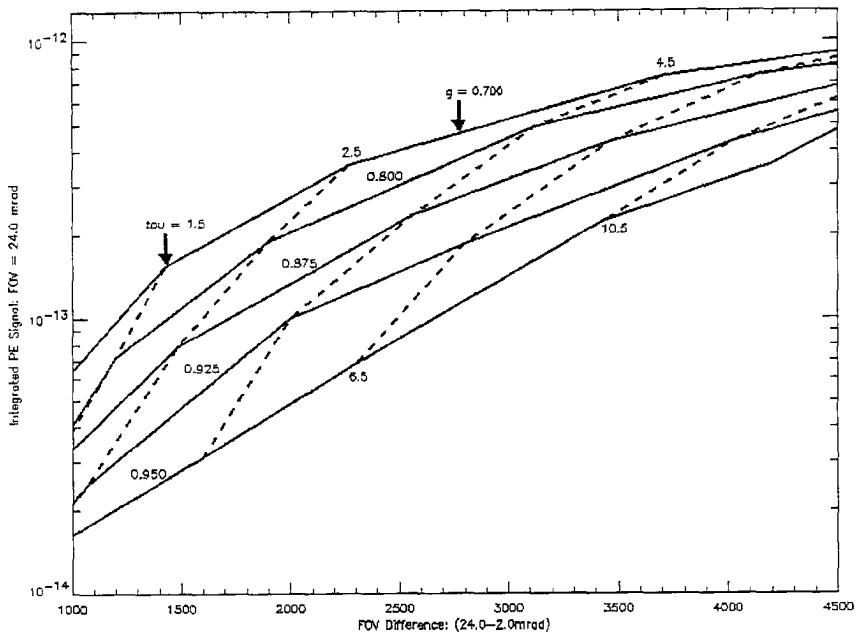

Figure 8.2: A two-parameter retrieval grid example using the integrated pulse extension signal and maximum pulse extension distance differences for two detector fields of view. (See text for details)

photon's ability to contribute to pulse extensions is determined largely by its ability to acquire added travel distances while staying within the detector field of view. For larger asymmetry parameters, the chances of this are less likely (the photon will tend to transmit through the optically thin cloud or escape the detector field of view via radial transmission), and the integrated signal hence is lower. For lower asymmetry parameters, the photon has a better chance of remaining within the detector field of view; more photons (but fewer when compared to a more optically thick cloud of similar scattering asymmetry) contribute to pulse extension events and a larger signal results. The second observation is consistent with Figure 7.7 which showed little change in maximum pulse extension for high values of g, and significant differences for lower g (the physical argument for this was given in Chapter 7). As optical thickness was increased the signal was observed to increase as well, as

expected. For very optically thick media, the discriminators became ambiguous, and no independent retrieval was possible.

Figure 8.2 differs from Figure 8.1 in that the abscissa is now a difference between the maximum below-cloud-base pulse extensions as measured from two different detector FOV. The ordinate remains as the integrated pulse extension signal return. The retrieval grid looks very similar to that of Figure 8.1 and does not appear to provide any marked improvement in orthogonalizing the iso-parameter curves. The fields of view used for the abscissa were 24.0 and 2.0 mrad. Consistent again with Figure 7.7, lower differences in pulse extensions occurred for lower τ and higher g, while higher integrated pulse extension signals were found for higher τ and lower g. Ambiguity in this grid arose for very low optical depths (where pulse extensions contributions become negligible) and at higher optical depths with large detector fields of view (due necessarily to an under-sampling as a result of the imposed scattering-order truncation and photon sampling constraints).

The question was posed early on as to which properties of the actual cloud particles might be retrievable from pulse stretching data. It was concluded that only a "bulk" cloud asymmetry parameter might be derived from the information, due to the random sampling of the characteristic cloud phase function by countless photons. The result obtainable was, in effect, a parameter representative of the integration of the medium's scattering phase function (a characteristic single-scattering phase function derived from an infinite sampling of the individual particles which comprise the distribution of the cloud). This rather convoluted result might still prove valuable if other information is available (*eg*, combined with assumptions on particle size distribution and Mie scattering theory, an effective cloud particle radius may be inferred). To examine the algorithm's ability to discriminate between three different "real world" phase functions, a retrieval grid based on the same structure of Figure 8.2 was constructed using three different ice crystal geometries from Takano

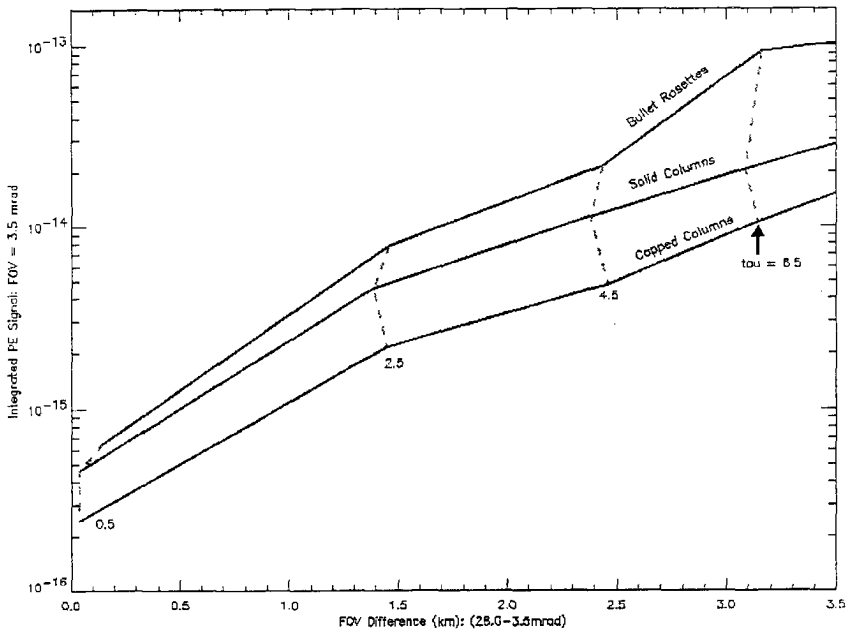

Figure 8.3: A two-parameter retrieval grid similar to Figure 8.1 but applied to Takano & Liou ray-tracing results for the ice crystal geometries shown.

& Liou's ray-tracing phase functions. The orthogonality between lines of constant τ and g is encouraging, and indicates that the retrieval of a characteristic cloud asymmetry parameter combined with other information about the cloud (from both the lidar and other instruments) may give provide additional discriminatory information about the distribution/phase/habits of the cloud particles themselves.

It cannot be over-emphasized that these results are merely an illustrative examination of the possibilities for using pulse extension information in the interest of cloud property retrievals. There may very well exist superior methods unexplored in this study. Furthermore, these grids were produced under the assumption that the fractional signal return due solely to the pulse extension signal was in fact a measurable quantity at the resolutions shown. Besides the properties of the cloud itself, the main driver of the ordinate (integrated return signal) values is the radial distance between the instrument and target. For any given experiment geometry,

a new model run would be required. In other words, the results shown herein are representative of strictly the hypothetical instrument, cloud, and sensing geometry as described; the emphasis of the discussion being not the physical retrieval itself, but the very question of retrievability. The more reliable application of the lidar pulse stretching data appears to be not in an autonomous retrieval, but in synergy with other instrumentation capable of providing independent information on the cloud. An *a priori* knowledge about the cloud extinction profile and true cloud base height would aid in the proper modeling of the cloud, provide an independent approximation of τ, and yield a one-to-one relationship between the measured pulse extension and the cloud asymmetry parameter.

8.1.3 Further Considerations

In order to apply lidar data to cloud property retrievals, the pulse stretching information must be extractable in a consistent and reliable way. Special consideration should be given to the minimum detectable signal threshold and the range resolution of the instrument. Rayleigh (molecular) backscatter return is a function of height in the atmosphere, with the strongest returns occurring near the Earth's surface (where atmospheric pressure, and hence molecular content, is highest). A pulse stretching signal threshold should be designated above the maximum molecular return. If the threshold is set too low then ambiguity will arise for lower-level clouds (where the maximum extent of the pulse stretched signal becomes muddied by atmospheric returns), while too high of a threshold will truncate cloud-property-discriminating pulse extension information. Sufficient range resolution is needed to capture differences in the pulse extensions. For the examples of this study, pulse extension signals varied on the order of kilometers. The LITE instrument had a specified vertical resolution of 15 meters; more than adequate for resolving the behaviors investigated here. In general, the hardware specifications for the instrument

flown in LITE (after which the hypothetical instrument of this study was modeled) appear to sufficiently meet these criteria.

8.2 Outline for a Field Experiment

It may be concluded from these preliminary findings that an inference of cloud optical properties is obtainable given sufficient pulse extension information. If desired, an independent retrieval of the relevant cloud optical properties could also be used to filter the pulse extension component observed in the raw imagery in order to more accurately represent the true cloud bases. Application of any algorithm involving the use of lidar pulse extension information ultimately would require a case-by-case comprehensive analysis of the system sensitivities and a multidimensional lookup table from which a solution may be extracted.

In anticipation of future lidar experiments with variable FOV detectors and synergy with other active/passive sensor instrumentation, a hypothetical experiment outline was constructed here for the purposes of assessing the utility/practicality of pulse stretching effects in cloud property retrievals. The retrieval would necessarily require the re-computation of the lidar pulse stretching relationships for the detector sensitivity and field-of-view options characteristic of the actual instrument used. This would be an off-line task to be completed *a posteriori* in order to best represent the geometry of the scattering media and instrument. This also represents a major drawback of retrievals based on pulse extensions, as a highly variable cloud field may require great computational cost. This study makes no attempt to explore the many possibilities of optimizing this effort, but a tabular/interpolation method employed in a great variety of cases appears to be feasible for some uniform cloud fields.

In addition to the variable-FOV space-borne/airborne lidar itself, independent remote sensing and *in situ* instruments should also be included in the experiment. An independent measurement of cloud base height data might be provided via

ceilometer or cloud radar. A cloud radar could also provide information about the cloud extinction (integrated over the bounds of the cloud to yield optical depth), and with some assumptions made about cloud particle distribution, an approximation to the bulk asymmetry parameter (g) of the medium. The addition of a cloud microphysics aircraft (*eg* the Wyoming King Air, which features a variety of *in situ* cloud particle measuring instruments) to the experiment would provide better information about the cloud particle size distributions, phases and habits, thereby leading to a better approximation of g. Independent verification data is an imperative link to a comprehensive testing of the pulse stretching retrieval algorithm.

Several different cloud types should be examined. Pulse stretching effects have been observed to occur in the persistent strato-cumulus cloud decks over the North-Eastern Pacific, South-Eastern Pacific, and South-Eastern Atlantic oceans. The optimal dataset would also include a variety of cirrus cloud fields, which have shown relatively little pulse stretching in the LITE imagery. Comparisons between maritime and continental cloud structures would provide an opportunity to determine pulse stretching sensitivities to different cloud particle distributions (a relatively higher concentration of smaller cloud particles over the continents due to an enhanced distribution of cloud condensation nuclei affects cloud optics–an "indirect means of measuring the aerosol indirect effect"). The location and time-of-year for scheduling the experiment should be dictated by the availability of these optimal environmental conditions.

A simple procedure for gathering pulse stretching data in a correlative experiment is as follows:

- Arrange the experiment to take place in a location and during a time which maximizes the possibilities of synergy with other instrumentation.

    1. A nighttime, no-moon operation window would be optimal (minimizing short-wave contamination)

2. Minimize aerosol contamination and surface reflection effects. (*eg.* the Eastern Pacific Ocean, marine strato-cumulus)

- Using a sufficiently narrow detector FOV (such that single scatter dominates the signal return), first determine the true cloud base height.

  1. *Co-located* (spatial and temporal) validation data from independent measurements used to verify this single-scatter approximation.

  2. If a true cloud base altitude cannot be identified, the algorithm as posed cannot be tested.

- Once a true cloud base has been established, systematically increase the detector FOV and record measurements of the resultant pulse stretching effects.

  1. The FOV sample sequence (scanning from smallest to largest) should be completed as rapidly as possible under hardware constraints in order to maximize the correlation between cloud scenes being viewed by the FOV measurement series.

  2. Include FOV which both maximize and minimize pulse stretching effects.

  3. Detector gain must be maintained as constant throughout the variable FOV measurement sequence such that pulse extension thresholds and integrations (used in the retrieval) are consistent.

- (Off-line) Apply appropriate retrieval method to obtain (τ, g):

  1. Given an estimate of the optical depth, evaluate the bulk asymmetry parameter using the corresponding pulse extension physical distances.

  2. Without *a priori* information on cloud optical depth, construct a retrieval grid based on integrated pulse extension signal return and extension distances for different FOV measurements.

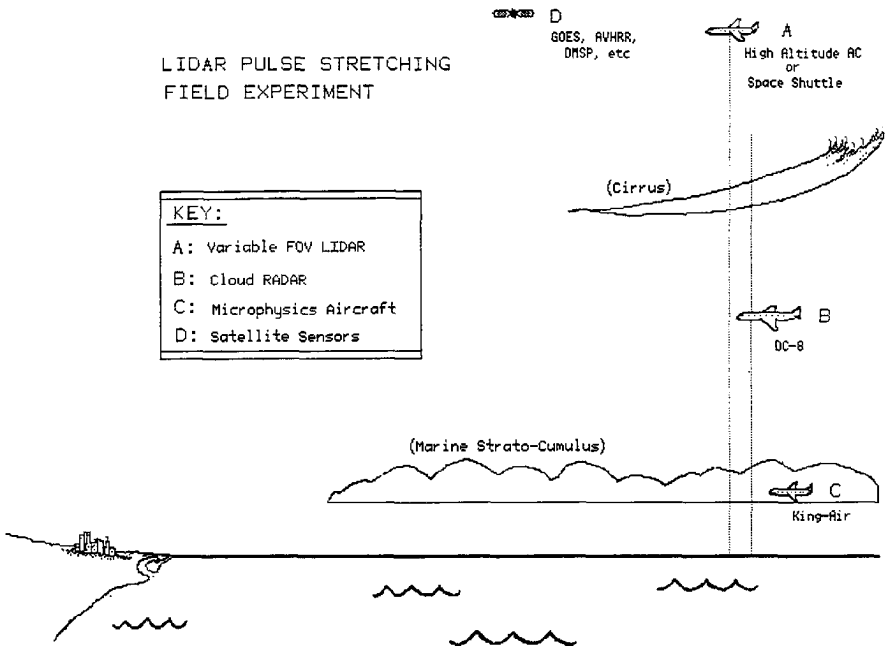

Figure 8.4: Validation of lidar pulse stretching retrievals may be achieved via synergy with independent, co-located measurements

- (Off-line) Compare with independent results:

  1. Cloud radar empirical cloud property retrievals.

  2. Satellite (passive sensor) cloud property retrievals.

  3. Micro-physics aircraft to aid in characterizing cloud particle distributions.

Figure 8.4 is a cartoon schematic depicting a hypothetical pulse-extension-based retrieval validation experiment. Shown are four independent measuring systems (lidar, cloud radar, cloud micro-physics probes, and satellite passive sensor instruments) which would aid in this effort. In this way, a sufficient dataset could be compiled which would serve to test the utility of pulse stretching information in cloud property retrievals. Such an experiment could readily be coordinated within the backdrop of a greater IOP-type lidar survey; with many other experiments con-

ducted simultaneously and without compromise to the requirements of the pulse stretching study.

8.2.1 Applications to Operational Retrievals

The immediate role of the active sensor on the space platform would be to compliment existing passive remote sensing applications. One direct benefit of an active sensor is its utility in cloud height (and geometric thickness) detection. This problem has been addressed in the remote sensing community by methods of CO2-slicing, cloud shadow geometric techniques, and even by the mapping of brightness temperatures onto standard temperature profiles (invoking a blackbody emission assumption on the clouds which fail miserably in optically thin over warm background cases). No method is free of uncertainty, and the vertical structure of the cloud fields or identification of multiple layers shielded by upper layers remain difficult if not impossible (and radiatively significant) parameters to obtain.

In a concurrent study, the application of active sensor instruments in aiding existing passive sensor cloud optical property retrievals is being investigated. Figure 8.5 is an actual cloud optical depth retrieval for the Complex-Layered Cloud Experiment (CLEX) which was carried out in June, 1996. The retrieval integrated GOES-8 imager channel data (IR + VIS) with co-located cloud radar data from the JPL/UMASS 94GHz airborne cloud radar (ACR) flown on a DC-8 experimental aircraft during the IOP. The ACR provided accurate information on the geometric boundaries of the cloud structure, and this information was used as *a priori* input to the satellite retrieval. Using various reflectivity parameterizations, independent information about the cloud extinction, liquid water content, and effective particle radius was also obtainable from the ACR. While the original satellite retrieval algorithm was designed to simultaneously retrieve both cloud optical depth and effective particle radii (r_{eff}), the code was modified to fix the cloud asymmetry (assuming it as *a priori* information to the retrieval) and retrieves on optical depth alone. The

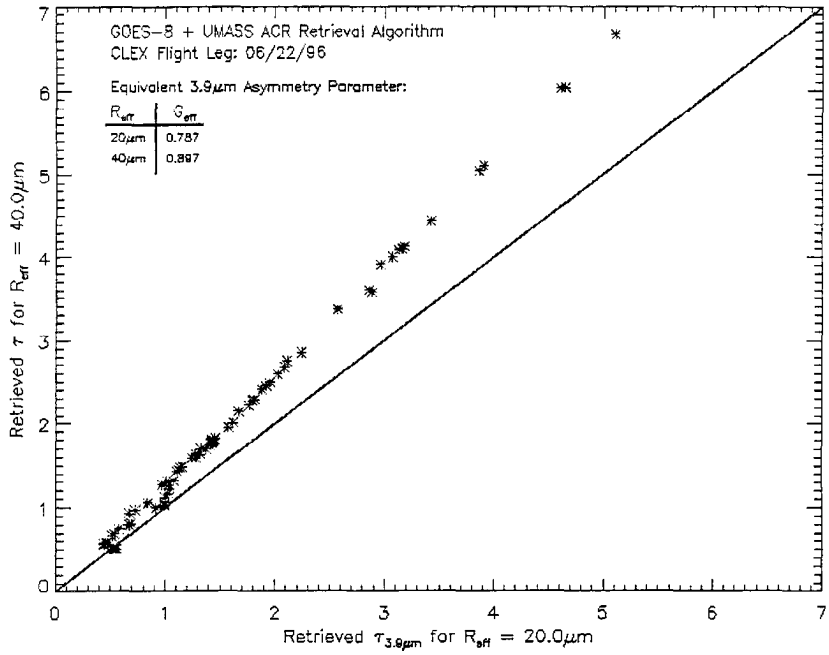

Figure 8.5: A comparison of GOES-8 derived cloud optical depth retrievals for fixed effective particle radii

figure shows a comparison between the retrieved cloud optical depth for the two cases of $r_{eff} = 20.0\mu m$ and $r_{eff} = 40.0\mu m$. Through an assumption on the particle size distribution (assumed here to be a modified-γ distribution with a dispersion of 2.0) and Mie scattering theory, these effective radii were translated to equivalent asymmetry parameters as specified. Fixing the cloud asymmetry parameter resulted in $3.9\mu m$ cloud optical depth retrievals which were greater for the higher forward-peaked scattering phase function (corresponding to $r_{eff} = 40\mu m$). The mean relative difference between the two retrievals was $23.7 \pm 0.875\%$.

The overestimation of cloud optical depth at $3.9\mu m$ can be explained in terms of both short-wave and infrared radiative transfer theory. For short-wave (solar), the brightness (reflectivity) of the cloud as seen from space is determined by the ability of the cloud to reflect the down-welling radiation back upwards to space. For short-wave radiation, this is largely a function of the cloud optical thickness,

which is effectively reduced by introducing a more forward-peaked scattering phase function. To achieve the appropriate reflection to match the observation, the retrieval algorithm must increase the cloud optical depth accordingly, resulting in a relatively high result compared to that of the lower cloud asymmetry parameter retrieval. From an infrared standpoint, the warmest regions of the atmosphere exist near the surface (in this case, below the cloud layer which resided near 8km AGL). For a more forward-peaked scattering phase function, emissions from warmer regions below the cloud will have a better chance of transmitting through and reach the satellite's detector. If the cloud scene appears "cold" to the detector, the optical depth in the model must be increased to compensate for the increase in asymmetry parameter. Hence, the retrieved optical depth for the higher g case again results in a relatively high value.

While this discussion of sensitivity of retrieved cloud optical depth to variations in cloud asymmetry is an issue germane to this research, its relationship to retrievability by means of lidar pulse stretching observations remains somewhat convoluted. This is because in order for the pulse stretching retrieval to yield an adequate approximation to g, τ must first be known rather stringently. Nonetheless, the ability to retrieve g from pulse extension data may still serve as a useful independent verification for passive sensor retrievals. Simultaneous passive sensor retrievals remain an essential and natural link to any validation of the new lidar pulse extension cloud property retrieval procedure. These retrievals consist largely of channel-differencing techniques as currently applied to operational satellites in order to extract independent information about cloud optical properties.

8.3 Summary

An assessment of the utility of lidar pulse extension data in cloud optical property retrievals was discussed. Depending on the availability of independent data,

retrievals of cloud asymmetry alone, or cloud asymmetry *and* cloud optical depth, appear possible. Without adequate information on the cloud extinction profile, the latter method should not be applied, as uncertainties in modeled pulse extensions for varying cloud profiles are high. The approximation to plane parallel cloud may be valid for some stratified cloud formations, but in general is not a realistic assumption for real-world applications. Provided synergy with other instruments, an operational retrieval method based in part on lidar pulse extension information appears to become a tractable problem. An outline has been provided for creating the database necessary for a thorough testing of the algorithm in a field experiment setting. Instrumentation dedicated to supporting/validating the lidar retrieval results would be vital to this effort. Pulse extension retrievals would have immediate applicability to independent verification of other satellite remote sensing algorithms.

Chapter 9

SUMMARY AND CONCLUSIONS

This research endeavored both to characterize and quantify the lidar pulse stretching effects observed during the LITE mission in terms of the optical properties of the clouds producing them. To this end, a series of diagnostic exercises were performed in an attempt to both modularize and fully-characterize the problem. The fruit of this effort was a first look at the internal physics of a non-trivial (even by the standards of the simple cloud media examined herein) multiple-scattering process shown to be responsible for the lidar pulse stretching artifacts observed in LITE. The following chapter contains a recapitulation of the approach taken, the primary findings of this work, and concludes with comments toward branching avenues of research.

9.1 Summary of Approach

The lidar pulse stretching phenomenon was explained physically in terms of the multiple scattering process. Because the Monte Carlo method is capable of representing a signal in terms of the multiple scattering series explicitly, it was recognized as the logical tool for the modeling of this effect. A forward Monte Carlo code was revised to simulate a lidar instrument, assuming hardware and viewing conditions similar to those of LITE, and its performance was verified with both theory and the results

of previous investigators. The inclusion of anisotropic scattering phase functions (in the form of probability distribution lookup tables and the analytical Henyey-Greenstein phase function) was done in order to represent more realistic scattering cloud media and provide for a systematic examination of below-cloud-base pulse extensions (a measurable quantity) as a function of varying bulk cloud scattering properties (of interest to radiative transfer parameterizations).

In order to grasp the various behaviors of multiple scattering effects as applied to the lidar (finite beam) problem, several experiments were carried forth to investigate photon path distributions for a variety of cloud optical depths, scattering behaviors, and cloud geometries. These tests included the evaluation of distributions for radial contributions, photon path lengths, and signal return as a function of varying detector fields of view. These data served as proxies to lidar pulse stretching effects, and provided a clearer picture of the spatial distributions of scattering events throughout the cloud. As such, they comprised the foundation for the discussion of the modeled pulse stretching results.

The modeling of lidar pulse stretching emphasized the below-cloud-base pulse extension signals (recorded for various detector FOV) as a function of cloud optical depth and asymmetry parameter. This value was considered as a measurable quantity (provided a means of identifying the true cloud base) in an operational scenario. As these results were rendered for highly simplified cloud fields, a further examination of the relative differences in pulse extension magnitudes was conducted for cloud geometries which varied in the horizontal and vertical, as well as for the case of multiple cloud layers. The results presented for the simplified cases demonstrated relationships between cloud optical properties and pulse stretching behaviors which may be considered as fundamental to the problem, and appropriate for a first-order discussion of these effects.

An investigation into how these pulse stretching results might be used in a cloud property retrieval followed. The values of the pulse extensions for different detector

FOV were combined with measurements of integrated extended signal strength in an attempt to formulate bi-parameter retrieval grids for τ and g. In order to test the theoretical relationships in practice, a data set dedicated to the specific *a priori* requirements of the pulse extension retrieval was needed. This lead to the proposal and outline for a comprehensive validation study which included several other independent remote sensing instruments. The relevance of these retrieval techniques in complimenting and/or validating existing passive sensor retrieval methods was also discussed.

9.2 The Primary Findings

This research addressed the role of multiple scattering in the observations of lidar pulse extensions in the raw LITE imagery. From the modeled multiple-scattering and pulse stretching results, the following conclusions were drawn:

- The notion of an "enhanced cloud penetration" due to multiple scattering effects is somewhat misleading, since scattering events were observed to diffuse radially with increasing scattering order. It is more likely that these are the signatures of pulse stretching occurring within the cloud, and should not be interpreted as providing additional information about the cloud at the ranges indicated.

- Over the range of cloud asymmetry parameters found in nature (typically 0.7 and upwards) and cloud extinction coefficients between 1.0/km and 20.0/km, the modeled below-cloud-base pulse extensions for a 1km thick stratified cloud varied from 0.0 to 5.0km. These values are similar in magnitude to the extensions observed during LITE. Vertical resolutions and detector sensitivities as specified for the LITE instrument were sufficient for these retrieval approaches.

- Pulse extension signal strengths also decreased with increasing g and decreasing τ. This is reasonable from physical arguments, and leads to the deduction that the most dramatic pulse extensions should be observed in optically thick water clouds residing in aerosol-rich environments and less dramatic effects in thin ice clouds. A cursory examination of the raw reflectivity return from several of the LITE mission orbits also appears to support this claim.

- Increasing the detector FOV resulted in a corresponding increase in pulse extension distance over a limited regime. These findings were expected from the observations of radially-scattered photon distributions.

- A single pulse extension measurement alone leads to an infinite number of simultaneous (τ, g) solution pairs.

- Constraining τ with other inversion methods or independent instruments leads to an unambiguous retrieval of g from the measured pulse extension distance. Additionally, the degree of cloud inhomogeneity over the scene containing the detector FOV may be assessed by comparing the retrieved cloud asymmetry parameter to an *a priori* assumption of g.

- Alternatively, an assumption on the particle distribution and independent retrieval of effective particle radius (*eg*, using a cloud radar empirical retrieval) enables an approximation to g, and would provide for an unambiguous retrieval of cloud optical depth from the measured pulse extension distances.

- Simultaneous retrievals of τ and g may be achieved if the integrated pulse extension signal is measurable and variable FOV data are available. Taking advantage of spectral-dependencies in cloud particles (via a variable-wavelength lidar) may lead to superior orthogonal relationships between τ and g.

- Pulse extension results can vary dramatically between cloud morphologies. For most retrieval applications, an off-line analysis based on the particular geometry of the cloud/lidar combination would be required.

The main drawback of using pulse stretching effects in the retrieval of cloud properties lies in the computational cost inherent to Monte Carlo techniques. It was shown that pulse extension results were highly variable with cloud geometry; necessitating the computation of a new lookup-grid for every new cloud geometry, instrument geometry, and range encountered. While cloud climatology may aid in the assembly of a generalized *a priori* data base, it has not been established that standard interpolations would apply to the pulse stretching behaviors. At this stage, it appears more likely that the utility of pulse stretching information would manifest itself in case-study investigations, as opposed to full-blown operational retrievals.

The results of this work represent a first-attempt at utilizing multiple scattering signatures from lidar returns to the retrieval of cloud properties. Combined with other instrumentation, there is great promise for the use of this method as a complimentary tool in retrieval validations. As active sensors find their way onto the space platform, more opportunities for further exploration of the relationships between cloud optical properties and the multiple-scattering signatures characterizing them will present themselves.

9.3 Toward Future Investigations

Even with the new revisions made, the model and assumptions applied to this study remain quite primitive with respect to any physical system. The transition from theoretical development to operational applicability, however, should come only after a thorough validation of the retrieval algorithm is applied and its feasibility assessed. In order to further the understanding of the pulse stretching problem and how its characteristics might be harnessed as useful information, several additional

improvements and adjustments should be made above and beyond what has been attempted here. These include:

- Improvements and generalizations to the model:
  1. Addition of a Rayleigh (molecular) scattering atmosphere.
  2. Further investigations into 3-dimensional, multi-layer cloud profiles.
- Investigation of lidar backscatter return as a function of angular scanning. (Such experiments were conducted during LITE to investigate ocean surface albedos).
- Exploring pulse stretching behaviors at other lidar frequencies (*eg* 1064 nm). As particle scattering behaviors have strong spectral dependency, this may provide an additional means of eliminating solution redundancies.
- Processed LITE data will be available shortly (from date of this document). This will provide an opportunity to conduct limited testing of the algorithm using GOES-8/GOES-9 cloud property retrievals.
- A second LITE mission has been planned to fly in 1998. Coordination with ground/airplane measurements as outlined in Chapter 8 would provide the additional verification data needed for a thorough testing of the algorithm.
- A Japanese-designed and manufactured variable-FOV lidar instrument is currently in development, and would be well-suited to the needs of a pulse stretching validation study.

9.4 Closing Remarks

The motivation for this research was supplied, in part, by the old adage:

> ... One man's trash is another man's treasure.

Applied to the lidar pulse stretching problem, the "trash" is the pulse stretching artifact itself, which renders clean profiles of cloud vertical structure ambiguous due to the inherent and unavoidable multiple scattering processes taking place within the cloud media. The "treasure" lies in the ability to pan out from these muddied waters the driving cloud optical properties themselves. The conclusions drawn from this study have indeed shown promise for the modeling of pulse extensions as a means of retrieving meaningful cloud parameters in a variety of scattering media. The next stage would be the compilation of a validation data set to test the utility of the theoretical relationships presented here in the real-world environment. With the advent of active sensors on the space platform and ongoing interest in the identification of new retrieval methods, this would appear to be a likely undertaking.

Glossary

Active Sensor In remote sensing, an instrument which physically probes the atmosphere (usually by means of electromagnetic radiation) to derive properties of it.

Beam Divergence (BDIV) The solid angle (see below) characterizing the finite spread of the laser beam.

Bulk Asymmetry Parameter (g) A parameter which characterizes the anisotropy of the scattering phase function. A g of -1.0 implies complete backscatter, a g of +1.0 corresponds to complete forward scatter, and $g = 0.0$ represents an isotropic scattering behavior.

Diffuse Radiation Radiation which has undergone scattering by particles in the medium. These scattering events tend to diffuse radiation away from the direct beam.

Direct Beam Radiation which has not undergone a change in trajectory since being emitted from its source.

Extinction Radiation jargon for loss, or attenuation.

Extinction Coefficient (σ_{ext}) A measure of the attenuation of a direct-beam source along a geometric path (units of per-kilometer).

Field of View (FOV) The solid angle characterizing the finite receiver viewing area.

Flux (F) Integration of the intensity (spectral or broadband) over solid angle.

Footprint The projected area of the laser BDIV or detector FOV upon the surface of the medium.

Infrared In reference the spectrum of electromagnetic energy, encompassing all wavelengths longer than those of the visible red portion of the spectrum (usually, wavelengths between 0.9 and 4.0 μm are considered in the *Near*-Infrared, while wavelength longer than 4.0 μm are entirely within the infrared regime)

LIDAR Light Detection And Ranging active instrument used in this study. Actively probes media using laser emissions

Monte Carlo Statistical approach to solving the radiative transfer equation via the multiple scattering series.

Optical Depth (τ) The optical path along the local vertical. (Assuming a stratified atmosphere and projecting the optical path upon the vertical)

Optical Path Line integral of the extinction coefficient along an arbitrary geometric path.

Passive Sensor An instrument which relies on emission/external stimuli from the medium to provide its measurement signal

Photon Salvo A grouping of photons simulated together in a Monte Carlo run. The results from several independent salvos are averaged together to bring down the statistical variance.

Plane Parallel The simplifying assumption for cloud/atmospheric morphologies that assumes no variation of physical properties in the horizontal.

Pulse Extension The measurement of an extended (due to multiple scattering combined with a single-scatter ranging algorithm) signal beyond the edge of the physical media boundary.

Pulse Stretching An artifact stemming from the misranging (by a time-ranging algorithm) of multiply-scattered radiation.

RADAR Radio-wave Detection and Ranging. The analogy to the LIDAR at radio-wave (millimeter to centimeter wavelength) frequencies.

Radiance (I) A measure of the (spectral or broadband) electromagnetic energy traveling through a point at a specific viewing geometry (fixed in zenith and azimuth).

Remote Sensing A science dedicated to obtaining indirect measurements of a quantity or system using a platform removed from the property being measured (as opposed to *in situ* measurements). Indispensable whenever *in situ* measurements are not practical.

Scattering Angle (Θ) The angle formed between the incident and scattered directions of travel when a photon scatters off of a particle. $\Theta = 0.0$ corresponds to the forward scattering direction, and $\Theta = 180.0$ corresponds to the backscattering direction.

Scattering Order (K) A book-keeping index that indicates how many times a photon has scattered with particles in the medium.

Scattering Phase Function ($P(\Theta)$) A probability density function which characterizes the scattering tendencies of a particle or medium. Except for the isotropic case, the probability of a scattering angle assuming any given value between 0.0 and π is characterized by this function.

Single-Scatter Albedo (ω_o) Characterizes in a bulk sense the fraction of extinction of radiation due to scattering versus absorption. An ω_o of 0.0 denotes purely absorption, and $\omega_o = 1.0$ denotes purely scattering.

Single/Multiple Scattering Denotes whether photons have encountered one or many scattering events along the course of their travels.

Solid Angle (Ω) The area (in steradians) of an opening on the unit sphere: defining a cone of directions emergent from or incident upon a point at the center of this sphere.

Bibliography

[1] A. Ambirajan and D.C. Look Jr, 1996: A Backward Monte Carlo Estimator for the Multiple Scattering of a Narrow Light Beam. *J. Quant. Spectrosc. Radiat. Transfer*, **56**, No. 3, 317-336.

[2] L.R. Bissonnette, P. Bruscaglioni, A. Ismaeli, G. Zaccanti, A. Cohen, Y. Benayahu, M. Kleiman, S. Egert, C. Flesia, P. Schwendimann, A.V. Starkov, M. Noormohammadian, U.G. Oppel, D.M. Winker, E.P. Zege, I.L. Katsev, and I.N. Polonsky, 1995: LIDAR Multiple Scattering from Clouds. *Appl. Phys. B*, **60**, 355-362.

[3] D. Deirmendjian: *Electromagnetic Scattering on Spherical Polydispersions* (Elsevier, New York 1969), 186-187.

[4] V.A. Donchenko, I.V. Samokhvalov, G.S. Matvienko, 1971: Izv. Akad. Nauk SSSR, Fiz Atmos. Okeana **7**, 1183.

[5] D.P. Duda, 1994: *Macrophysical and Microphysical Influences on Radiative Transfer in Two Dimensional Marine Stratus.* Ph.d. Dissertation, Colo. State Univ., Dept. of Atmos. Sci., Fort Collins, 202p.

[6] G.M. Kaul, I.V. Samokhvalov, 1975: Izv. Vuzov, Ser. Fiz. **8**, 109.

[7] J.D. Klett, 1981: Stable Analytical Inversion Solution for Processing Lidar Returns. *J. Appl. Optics*, **20**, No. 2, 211-220.

[8] K.E. Kunkel and J.A. Weinman, 1976: Monte Carlo Analysis of Multiply Scattered Lidar Returns. *J. Atmos. Sci.*, **33**, 1772-1781.

[9] K.N. Liou, 1980: *An Introduction to Atmospheric Radiation* (Academic Press Inc., San Diego 1980), 182-184.

[10] G.I. Marchuk, G.A. Mikhailov, M.A. Nazaraliev, R.A. Darbinjan, B.A. Kargin, and B.S. Elepov: *The Monte Carlo Methods in Atmospheric Optics.* (Springer-Verlag Berlin Heidelberg, New York 1980) 208p.

[11] G.C. Mooradian, M. Geller, L.B. Stotts, D.H. Stephens, and R.A. Krautwald, 1979: Blue-Green Pulsed Propagation Through Fog. *Appl. Optics*, **18**, No. 4, 429-441.

[12] D.M. O'Brien. 1992: Accelerated Quasi Monte Carlo Integration of the Radiative Transfer Equation. *J. Quant. Spectrosc. Radiat. Transfer.* **48**. No. 1. 41-59.

[13] C.M.R. Platt. 1973: Lidar and Radiometric Observations of Cirrus Clouds. *J. Atmos. Sci.*, **30**. 1191-1204.

[14] C.M.R. Platt. 1981: Remote Sounding of High Clouds. III: Monte Carlo Calculations of Multiple-Scattered Lidar Returns. *J. Atmos. Sci.*, **38**. 156-167.

[15] C.M.R. Platt and D.M. Winker. 1996: Multiple Scattering Effects in Clouds Observed from LITE. *SPIE, Opt. in Atmos. Prop and Adapt. Sys.*, **2580**. 60-71.

[16] T.L. Schneider. 1995: Climatically Relevant Clouds as Seen by a Lidar and Radar. *Class Paper*. Colorado State University, 15p.

[17] J. Simpson, R.F. Adler and G.R. North, 1988: A Proposed Tropical Rainfall Measuring Mission (TRMM) satellite. *Bull. Amer. Met. Soc.*,**69**. No. 3. 278-294.

[18] P.W. Stackhouse, Jr., 1995: *The Effects of Two Dimensional Inhomogeneity on Ice Cloud Radiative Properties.* Ph.d. dissertation, Colo. State Univ., Dept. of Atmos. Sci., Fort Collins, 250p.

[19] G.L. Stephens and C.M.R. Platt, 1987: Aircraft Observations of the Radiative and Microphysical Properties of Stratocumulus and Cumulus Cloud Fields. *J. Climate Appl. Meteor.*,**26**, 1243-1269.

[20] G.L. Stephens: *Remote Sensing of the Lower Atmosphere: An Introduction.* (Oxford University Press, New York 1994) 523p.

[21] Y. Takano and K.N. Liou, 1995: Radiative Transfer in Cirrus Clouds. Part III: Light Scattering by Irregular Ice Crystals. *J. Atmos. Sci*, **52**, 818-837.

[22] S Tsay, J.M. Davis, G.L. Stephens, S.K. Cox, and T.B.McKee: Backward Monte Carlo Computations of Radiation Propagating in Horizontally Inhomogeneous Media. Part I: Description of Codes. *CIRA Report*, September 1987.

[23] D.M. Winker and L.R. Poole, 1995: Monte-Carlo Calculations of Cloud Returns for Ground-Based and Space-Based LIDARS. *Appl. Phys. B*, **60**, 341-344.

[24] D.M. Winker, R.H. Couch, and M.P. McCormick, 1996: An Overview of LITE: NASA's Lidar Inspace Technology Experiment. *Proc. IEEE*, **84**, 164-180.